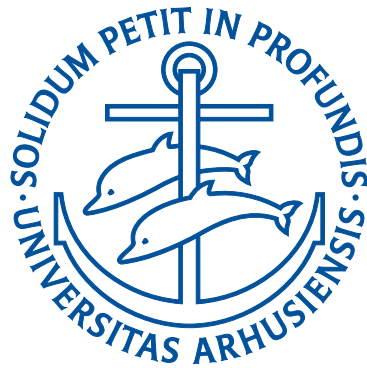


Atom Number Fluctuations in Bose-Einstein Condensates



Mick Althoff Kristensen
Department of Physics and Astronomy
Aarhus University, Denmark

Ph.D. Thesis
July 2018

ABSTRACT

Ever since the first creation of Bose-Einstein condensates (BEC) in 1995, physicist have had access to an almost ideal system to test a broad range of physical theories. The condensates constitute macroscopic quantum systems, and the toolbox for manipulation of these objects make them prime candidate as model system for quantum simulations. However, there are still unsolved questions relating to the statistics of the BEC. Within this thesis, research into the fundamental stability of atomic BECs is presented.

The phenomenon of Bose-Einstein condensation is statistical at heart. A full statistical description of the BEC is contained in the distribution function, which is characterised by it's moments. A knowledge of all moments thus contains all information we might hope to obtain about the statistics of the system. Bose gases at ultra-low temperatures present an interesting example, where grand canonical approaches to determine the statistics fails. To date, despite a large effort, no theory is able to fully account for all aspects concerning the statistics of the experimentally most relevant situation of weakly interacting condensates. Additionally, experimental investigations are limited to studies of the condensate fraction, corresponding to the first moment of the distribution. In our experiment we have successfully made the first ever measurement of the fluctuations of the condensate atom number in a ^{87}Rb BEC, which corresponds to the second moment. Our measurements show that the fluctuations are only weakly influenced by interactions, and that the peak fluctuations are similar in magnitude to the fluctuations of the non-interacting BEC.

These experiments are made possible by our novel preparation scheme. Using non-destructive dispersive imaging based on the Faraday effect, we measure atom numbers at sub-shot noise precision during the cooling process. Through real-time analysis of these images, we make an actively controlled correction of the atom number and obtain samples with a stability at the shot noise level.

RESUMÉ

DANISH ABSTRACT

Lige siden den første skabelse af Bose-Einstein kondensater (BEK) i 1995 har fysikere haft adgang til et ideelt system til test af en bred vifte af fysiske teorier. Kondensaterne udgør makroskopiske kvante-objekter, og med den lange række af redskaber til at manipulere disse objekter er de førsteklasses kandidater til model-systemer for kvantesimuleringer. Der er dog stadig en række ubesvarede spørgsmål der relaterer sig til den statistiske beskrivelse af BEKer. I den afhandling præsenteres forskning i den fundamentelle stabilitet af Bose-Einstein kondensater.

Bose-Einstein kondensering er i sidste ende et statistisk fænomen. En fuld statistisk beskrivelse af BEKet er indeholdt i fordelingsfunktionen, som er karakteriseret ved dens momenter. Kendskabet til alle højere momenter indeholder dermed al den information om systemets statistik, som vi kan håbe på at opnå. Bose-gasser ved ultralave temperaturer udgør et interessant eksempel hvor grand-kanoniske tilgange til at bestemme statistikken fejler. På trods af stor indsats er der endnu ikke nogen teori, der til fulde behandler alle aspekter af fluktuationerne i svagt vekselvirkende kondensater. Ydermere er de eksperimentelle undersøgelser begrænset til til studier af kondensatfraktionen, hvilket svarer den underliggende fordelings første moment. I vores eksperiment har vi lavet den første måling af fluktuationerne i et ^{87}Rb kondensat, hvilket svarer til det andet moment. Vores målinger viser at fluktuationerne kun er svagt påvirkede af vekselvirkninger, og at størrelsen af fluktuationerne er sammenlignelige i størrelse med fluktuationerne i det ikke-vekselvirkende BEK.

Eksperimenterne er muliggjort af vores nyskabende teknik til at skabe ultrakolde kvantegasser. Ved at anvende en ikke-destruktiv dispersive afbildning baseret på Faradayeffekten kan vi måle atomantallet med en præcision bedre end shot-støjniveauet i løbet af afkølingsprocessen. Ved hjælp af analyse af billederne i realtid kan vi aktivt kontrollere en korrektion af atomantallet og opnår derved skyer af atomer med antallet af partikler stabiliseret til shot-støjniveauet.

PREFACE

This thesis presents the research I have done during the last four years as a member of the Ultracold Quantum Gases Group at Aarhus University. I have been a part of the Lattice Experiment team, but despite the name, optical lattices has not been the focus of the research.

During my Ph.D. studies, two main research directions were pursued. When I started my studies, I joined the ongoing Faraday project together with former Ph.D. student Miroslav Gajdacz. This project led to the successful development of a stabilisation scheme that provides a stable source of ultracold clouds, and is now an invaluable tool in our experiments. The period covered by this project corresponds roughly to the first two years of my studies. The stabilisation technique enabled the pursuit of the observation of atom number fluctuations of Bose-Einstein condensates, which has been the goal in the last part of my Ph.D. I was joined in these investigations by Ph.D. student Mikkel Berg Christensen.

Research would not have been such a joy if not for the people I have been surrounded by during my studies. A big thanks to my supervisor Jan Arlt for support and guidance the Ph.D. studies. Your ability to always find time for lengthy and fruitful discussions of the project is invaluable, and I admire your ability to keep up the spirit in the group. A thank you is also in its place to Jacob Sherson, for countless valuable inputs during discussion.

A very special thanks goes to Miroslav Gajdacz and Andrew Hilliard.

You taught me to find my way around the lab, and without you both I would not possess the technical skills I do. Thank you for showing me both the value of highly creative thinking and the value of thoroughness.

Halfway through my studies, Ph.D. student Mikkel Berg Christensen joined me on the experiment when I would otherwise have been the sole student. The time has been so much more enjoyable when working with you, and it is cool to see that you are ready to take up the baton. In the last year we have been accompanied by Masters student Søren Sørensen Sneftrup. Thank you for bringing some proper taste of music back to the lab!

A huge thank you to all former and current members of the Mixtures team and the HiRes experiment, for joyful company both during work hours and leisure. You are a fantastic group to share victories and defeats with.

I would like to thank Mikkel Berg Christensen, Nils Byg Jørgensen, Jan Arlt and Nanna Bill Andersen for proofreading this thesis.

Thanks to friends and family for making life outside the confines of the lab so enjoyable. My sister Mette deserves a very special thank you for having a weakly dinner ready such that studies and dancing could both be managed! Thank you!

Finally the biggest thanks to my Nanna. You have been my tether to the real life, and it brings me happiness to have you at my side.

Mick Althoff Kristensen

LIST OF PUBLICATIONS

- M. Gajdacz, A. J. Hilliard, M. A. Kristensen, P. L. Pedersen, C. Klempt, J. J. Arlt and J. F. Sherson, Preparation of ultracold atom clouds at the shot noise level, *Phys. Rev. Lett.* **117**, 073604 (2016).
- M. A. Kristensen, M. Gajdacz, P. L. Pedersen, C. Klempt, J. F. Sherson, J. J. Arlt and A. J. Hilliard, Sub-atom shot noise Faraday imaging of ultracold atom clouds, *Journal of Physics B: Atomic, Molecular and Optical Physics* **50**, 034004 (2017).
- M. A. Kristensen, M. B. Christensen, M. Iglicki, K. Pawłowski, C. Klempt, J. F. Sherson, K. Rzażewski, A. J. Hilliard and J. J. Arlt, Observation of fluctuations in a Bose-Einstein condensate, In preparation (2018).

CONTENTS

Abstract	i
Resumé	iii
Preface	v
List of publications	vii
Contents	ix
1 Introduction	1
1.1 Non-destructive probing and preparation of ultracold gases	3
1.2 Atom number fluctuations in BECs	4
1.3 Thesis outline	5
2 Formation and fluctuations of Bose-Einstein condensates	7
2.1 The Bose-Einstein distribution	7
2.1.1 Bose-Einstein condensation of ideal gases	9
2.2 The interacting Bose gas	12
2.2.1 The Thomas-Fermi approximation	13
2.2.2 Shift of the critical temperature due to interactions	14
2.3 Fluctuations of Bose-Einstein condensates	15
2.3.1 Grand canonical fluctuations of the ideal gas . . .	17

2.3.2	Canonical and micro canonical fluctuations	18
2.3.3	Fluctuations in the interacting BEC	22
2.4	Cloud profiles	25
2.4.1	Semi-ideal model in TOF	33
3	Production and detection of ultracold gases	37
3.1	BEC apparatus	38
3.1.1	Laser cooling and magneto-optical trapping	39
3.1.2	Magnetic trapping	41
3.1.3	Forced RF evaporative cooling	43
3.1.4	Cooling water system	44
3.2	Laser system	46
3.3	Imaging systems	50
3.3.1	Absorption imaging	50
3.3.2	Faraday imaging	57
3.4	Bragg diffraction of ultracold clouds	57
4	Non-destructive Faraday probing of ultracold clouds	67
4.1	Faraday rotation	68
4.2	Experimental implementation of Faraday imaging	69
4.3	Characterisation of Faraday imaging	70
4.3.1	Evaluation of Faraday images	71
4.3.2	Absolute atom number and temperature	74
4.3.3	Atom number from the Faraday signal sum	76
4.4	Precision of Faraday imaging	77
4.4.1	Multi-image detection	82
5	Feedback-stabilised preparation of ultracold clouds	87
5.1	Experimental implementation	89
5.1.1	Analysis of Faraday images on the FPGA	90
5.1.2	RF control	92
5.2	Characterisation of RF induced losses	92

5.2.1	Noise growth due to stochastic loss of atoms	97
5.3	Active stabilisation of Faraday Signal	100
5.3.1	Adjustment of feedback parameters	101
5.3.2	Stabilisation at the shot noise limit	103
5.4	Atom number stabilisation	104
5.4.1	Loss induced at mean energy	105
5.5	Summary	107
6	Observation of fluctuations in Bose-Einstein condensates	109
6.1	Background	110
6.2	Experimental procedure	111
6.3	Image analysis	114
6.4	Correlations revealed by feedback stabilisation	115
6.5	Condensate fraction	117
6.6	Observation of fluctuations	120
6.6.1	Discussion of excess variance	125
6.7	Supporting analysis	126
6.8	Summary	128
7	Conclusion and outlook	129
A	Integrated density profiles	135
	Bibliography	137

INTRODUCTION

The development of quantum mechanics started at the beginning of the last century, when Max Planck considered the problem of black-body radiation. In order to derive the Planck distribution he introduced the concept of discreteness of the electromagnetic spectrum [1]. While he considered it a mathematical tool only, this was picked up by Albert Einstein to explain the photo-electric effect by treating electromagnetic radiation as particles, now called photons [2]. Niels Bohr used the concept of quantisation to develop his orbital model of the atom [3], and with the ground breaking works of pioneering physicists such as Werner Heisenberg, Paul Dirac, Erwin Schrödinger and many more, modern quantum mechanics was born.

Today quantum mechanics is one of the most successful and important theories in all of physics. Governing nature at the microscopic level, it helps us explain a broad range of phenomena. Subatomic particles, the

processes inside stars and the structure of molecules are all understood using quantum mechanics. Modern lifestyle has been revolutionised by the technological advances brought about by the understanding of matter at the microscopic levels. Inventions such as the semi-conductor transistor and the laser that are fundamentally dependant on quantum mechanics are the crucial ingredients in information technology, which plays an ever larger role.

The next generation of quantum technology is based on exotic phenomena such as quantum superposition and entanglement. This will enable a new generation of technologies to realise quantum metrology, quantum communication and quantum simulation and quantum computing [4, 5]. A wide range of physical systems are being studied for the application within quantum science. Among others, this includes trapped ions [6], super-conducting circuits [7], photonic systems [8], Rydberg atoms [9], ultracold quantum gases and Bose-Einstein condensates (BECs).

Bose-Einstein condensation corresponds to the accumulation of a macroscopic population in the ground-state of a quantum system. It was first predicted when Satyendra Nath Bose asked Einstein to translate his paper into German, in which he re-derived Plancks law by introducing a new counting statistic, where photons is regarded as indistinguishable [10]. Einstein extended the result to massive particles, and realised that they would condense into the ground state at low enough temperatures [11].

In 1995 three groups independently succeeded in creating the first BECs in dilute alkali gases [12–14], followed four years later by the cooling of Fermi gases to degeneracy [15]. Since then, the field has attracted large attention, with hundreds of groups now routinely producing BECs of not only alkali metals, but also Helium, alkaline earth metals and rare earth metals among others. The palette of tools to manipulate these pure quantum systems of macroscopic extent is rich. The confining potentials can today be shaped almost arbitrarily through the use of mag-

1.1. Non-destructive probing and preparation of ultracold gases

netic, radio-frequency and optical fields. Through Feshbach resonances, the interactions between the atoms can be finely tuned over several orders of magnitude from attractive to repulsive interactions [16], and the composition of different particles can be controlled [17, 18]. Together, this makes ultracold quantum gases an ideal test-bench for quantum simulations [19]

Bose-Einstein condensation is fundamentally a statistical phenomenon. Einstein was led to the conclusion that condensation occurs in the ideal gas by considering the statistics of Bosons at low temperature using a grand canonical approach. All information of the statistics is contained in the distribution function for the gas, which is characterised by its moments. The moments are however not known for real BECs except for the first moment, which is the mean condensate atom number and has been studied experimentally [20–22].

The research presented within this thesis follows two directions. The use of Faraday rotation to non-destructively probe ultracold gases is investigated in detail, and the information we infer from such measurements is then used in a feedback scheme to stabilise the preparation of ultracold gases. Using the feedback scheme as a starting point, this has provided the opportunity to study the statistics of BECs, which resulted in the first experimental observation of the atom number fluctuations of BECs at finite temperature.

1.1 Non-destructive probing and preparation of ultracold gases

Ultracold gases are usually probed using optical methods. The ubiquitous tool is absorption imaging, where the spatial distribution is inferred from the absorption of a resonant imaging beam. However, when the optical density is large, the probe beam will be completely absorbed,

and the method is therefore mainly applicable to time-of-flight imaging. Furthermore, the absorption of resonant light leads to significant heating, which destroys the sample.

To avoid these limitations, one can resort to dispersive and other minimally destructive techniques. A wide range of methods including phase-contrast imaging, diffractive methods and partial transfer absorption imaging is used to study the quantum gases in-situ [23–30]. In our experiment we take advantage of the Faraday effect, where the polarisation state of light rotates under propagation through a spin polarised medium. The spatially dependant rotation angle is detected, and provides information on the spatial distribution of the sample [31]. This so-called Faraday imaging method achieves sub-atom shot noise precision on atom number determination in ultracold thermal gases [32].

Non-destructive probing has been used as precursor measurement applied during the preparation of ultracold gases [33, 34]. Conditioning the final atom number on the precursor measurements allows for a reduction of classical number fluctuations. We supplement Faraday imaging with fast on-line analysis of the images on a field-programmable gate array (FPGA), which allows us to take a step further and correct for atom number variation by altering the evaporative cooling sequence. This methods provides ultracold samples stabilised in atom number at the shot noise level [35]. Reduction of number fluctuations may lead to improved performance of atomic clocks limited by collisional shifts [36] and reduction of the linewidth of atom lasers [37]. The feedback stabilisation is furthermore an invaluable tool for our investigations of the atom number fluctuation of BECs.

1.2 Atom number fluctuations in BECs

Despite the fact that first experimental realisations of BEC occurred more than twenty years ago, and the theoretical discovery precedes this by

another 70 years, there are still unsolved fundamental issues in the description of the BEC. The description of the ideal gas within the grand canonical ensemble fails for all moments but the mean condensate fraction [38], and presents an interesting example where the statistical description within the microcanonical, canonical and grand canonical ensemble are not equivalent, even in the thermodynamic limit [39]. Within the grand canonical ensemble, the fluctuations of the condensate atom number diverges at $T = T_c$, which is unphysical and contradicts experiments.

The creation of BEC renewed the large interest in this problem. The numerical tools to calculate the fluctuations of the ideal gas were developed within the canonical ensemble [40], but the experimental relevant case of interacting trapped gasses remains an unsolved problem and warrants experimental investigation.

The feedback stabilised preparation of ultracold gases provides us with a unique opportunity to study these fluctuations. The stable starting conditions for the creation of a BEC reveals correlations of the total atom number and temperature. Using these correlations greatly increases the information content in a measurement of the total atom number, and has enabled us to make the first observation of fundamental atom number fluctuations in BECs.

1.3 Thesis outline

This thesis is structured as follows:

Chapter 2: Formation and fluctuations of Bose-Einstein condensates

Key theoretical concepts for ultracold quantum gases are presented. This includes the concept of Bose-Einstein condensation, the Gross-Pitaevskii equation and the behaviour of Bose gases expanding during free fall. Additionally, a thorough overview off the theoretical work on the description of fluctuations in a Bose-condensed system is given.

Chapter 3: Production and detection of ultracold gases

The experimental apparatus used within this thesis is presented with an emphasis on recent changes and upgrades not covered by previous Ph.D. dissertations from the group. The analysis of absorption images is covered in detail.

Chapter 4: Non-destructive Faraday probing of ultracold clouds

Our implementation of Faraday imaging, a non-destructive dispersive imaging technique, is presented with an in-depth experimental characterisation of the precision of the method.

Chapter 5: Feedback-stabilised preparation of ultracold clouds

This chapter presents our preparation scheme, where the cooling sequence is modified in real-time based on non-destructive measurements of the cloud properties. With this we have demonstrated the preparation of ultracold clouds at the atom shot noise level.

Chapter 6: Observation of fluctuations in Bose-Einstein condensates

This chapter presents the experimental observation of the atom number fluctuations of BEC. Using the stabilised preparation of thermal clouds as a starting point for creation of BECs, a strong correlation between atom number and temperature is observed. Taking advantage of this correlations leads to improved precision on the temperature determination. This in combination with careful analysis of time-of-flight absorption images enables us to measure the fluctuations of the condensate atom number.

Chapter 7: Conclusion and outlook

The thesis concludes with a summary of key results and an outlook for future work.

FORMATION AND FLUCTUATIONS OF BOSE-EINSTEIN CONDENSATES

This chapter presents a theoretical overview of relevance for the experimental work presented in the following chapters. It opens with a description of the formation of BECs, followed by a review of the available theory of fluctuations of BEC. The last part of this chapter covers the description of the cloud profiles in-trap and in time-of-flight (TOF), since a detailed understanding of these is necessary when extracting properties from images of ultracold clouds.

2.1 The Bose-Einstein distribution

The phenomenon of Bose-Einstein condensation is statistical at heart. For non-interacting indistinguishable particles, the occupancy of the

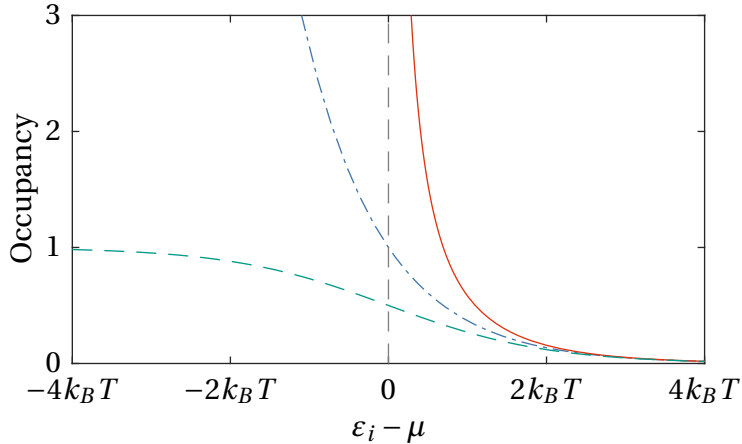


Figure 2.1: Plots of the Bose-Einstein distribution (—), the Fermi-Dirac distribution (---) and the Maxwell-Boltzmann distribution (-·-·).

state i with energy ε_i is given in the grand-canonical ensemble by the distribution function

$$f^0(\varepsilon_i) = \frac{1}{e^{(\varepsilon_i - \mu)/k_B T} \pm 1}, \quad (2.1)$$

where μ is the chemical potential, k_B is the Boltzmann constant and T is the temperature. The sign in the denominator is determined by the particle type. For bosons the sign is negative, and we obtain the Bose-Einstein distribution, and for fermions, the sign is positive and the distribution is the Fermi-Dirac distribution.

For high temperatures, $\mu \rightarrow -\infty$, and the ± 1 can be neglected. Then both distributions approach the classical Maxwell-Boltzmann distribution

$$f_{\text{MB}}^0(\varepsilon_i) = e^{-(\varepsilon_i - \mu)/k_B T}. \quad (2.2)$$

However, the difference is dramatic at low temperatures as illustrated in Fig. 2.1. As the chemical potential becomes larger than the energy of

a given state, the Fermi-Dirac distribution goes to 1, and at most unity filling of the state is obtained, as required by the Pauli exclusion principle.

The situation is completely different for the Bose-Einstein distribution. When the chemical potential increases, the occupancy starts to diverge. Additionally, it's evident that the chemical potential is constrained to $\mu < \varepsilon_0$ in order to keep the occupation of the ground state positive. The peculiarities of the Bose-Einstein distribution leads to the fascinating phenomenon of Bose-Einstein condensation, which is considered next.

2.1.1 Bose-Einstein condensation of ideal gases

Bose-Einstein condensation corresponds to the build-up of a macroscopic population in the ground state of a system, which occurs below a certain temperature denoted as the critical temperature T_c . It occurs when particles can no longer be accommodated in the excited states of the system. For large N we can choose the ground state energy to $\varepsilon_0 = 0$, which implies that the maximal value of the chemical potential is $\mu = 0$ in order for the occupancy $f^0(\varepsilon_0)$ to stay positive. Then the number of particles in the excited states is obtained by summation of the occupancy (Eq. (2.1)) of all states $i > 0$. This summation is typically simplified by introducing the density of states $g(\varepsilon)$ and converting the sum to an integral [41]:

$$N_{\text{th}} = \sum_{i \neq 0} \frac{1}{e^{\varepsilon_i/k_B T} - 1} \rightarrow \int_0^{\infty} d\varepsilon g(\varepsilon) \frac{1}{e^{\varepsilon/k_B T} - 1}. \quad (2.3)$$

The solution depends on $g(\varepsilon)$, which is given by the specific geometry of the confinement. For a three-dimensional anisotropic harmonic trap, the density of states is

$$g(\varepsilon) = \frac{\varepsilon^2}{2(\hbar\bar{\omega})^3}, \quad (2.4)$$

2. FORMATION AND FLUCTUATIONS OF BOSE-EINSTEIN CONDENSATES

where $\bar{\omega} = (\omega_x \omega_y \omega_z)^{1/3}$ is the geometric mean of the trapping frequencies. The solution in this case is

$$N_{\text{th}} = \frac{\zeta(3)(k_B T)^3}{(\hbar \bar{\omega})^3}, \quad (2.5)$$

where $\zeta(x)$ is the Riemann zeta function. The critical temperature can be determined by requiring that $N = N_{\text{th}}$:

$$N = N_{\text{th}} = \frac{\zeta(3)(k_B T_c)^3}{(\hbar \bar{\omega})^3} \implies k_B T_c = \frac{\hbar \bar{\omega}}{\zeta(3)^{1/3}} N^{1/3}. \quad (2.6)$$

Below T_c the total atom number is larger than N_{th} , and the remaining atoms accumulate in the ground state. The condensate fraction is then

$$\frac{N_0}{N} = \frac{N - N_{\text{th}}}{N} = 1 - \left(\frac{T}{T_c}\right)^3 \quad (2.7)$$

Chemical potential above T_c

Above the critical temperature, μ is determined by Eq. (2.3) by allowing for $\mu < 0$. The condition for the chemical potential is then given by

$$N = \int_0^\infty d\varepsilon g(\varepsilon) \frac{1}{\tilde{z}^{-1} e^{\varepsilon/k_B T} - 1} = \left(\frac{k_B T}{\hbar \bar{\omega}}\right)^3 g_3(\tilde{z}), \quad (2.8)$$

where the fugacity $\tilde{z} = \exp(\mu/k_B T)$ has been introduced. The function $g_\gamma(x)$ is known both as the Bose function and the Polylogarithm function and defined as

$$g_\gamma(x) = \sum_{j=1}^{\infty} \frac{x^j}{j^\gamma}. \quad (2.9)$$

Note that $g_3(1) = \zeta(3) \approx 1.202$, such that Eq. (2.8) reduces to Eq. (2.5) when $\mu = 0$. Above the critical temperature, Eq. (2.8) can be solved for the chemical potential given the total atom number and temperature.

Corrections to the condensate fraction and critical temperature

The expression for the condensate fraction given by Eq. (2.7) completely neglects the finite size and the interactions within a real condensate. In order to arrive at Eq. (2.7) the simplifying assumption that $\varepsilon_0 = 0$ is made. The finite N can be taken into account, by considering the zero-point energy. The condensate fraction is then found to be smaller than the $N \rightarrow \infty$ prediction of Eq. (2.7) [42]. To leading order the change in the condensate fraction is [43]

$$\frac{N_0}{N} = 1 - \left(\frac{T}{T_c}\right)^3 - \frac{3\omega_m \zeta(2)}{2\bar{\omega} [\zeta(3)]^{2/3}} \left(\frac{T}{T_c}\right)^2 N^{-1/3}, \quad (2.10)$$

where $\omega_m = (\omega_x + \omega_y + \omega_z)/3$ is the arithmetic mean of the trapping frequencies. In the limit of $N \rightarrow \infty$ this reduces to the simple prediction of Eq. (2.7). Since it depends on the ratio $\frac{\omega_m}{\bar{\omega}}$, the effect is enhanced for highly asymmetric harmonic traps.

It is worth noting that the finite size of experimentally realisable systems smears out the onset of condensation. Hence, Bose-Einstein condensation is only truly a phase transition in the thermodynamic limit [42, 43]. Still, the transition is rather sudden already for $N = 1 \times 10^4$, and the critical temperature is still a useful concept. If we set the condensate fraction equal to zero in Eq. (2.10), we obtain the approximate shift ΔT_c^{FS} of the condensation temperature due to the finite size of the sample

$$\frac{\Delta T_c^{\text{FS}}}{T_c} = -\frac{3\omega_m \zeta(2)}{2\bar{\omega} [\zeta(3)]^{2/3}} N^{-1/3} \approx -0.73 \frac{\omega_m}{\bar{\omega}} N^{-1/3}. \quad (2.11)$$

This shift of the critical temperature due to the finite size of the system is typically a small effect on the order of a few percent for condensates with 1×10^4 to 1×10^7 atoms.

2.2 The interacting Bose gas

In Section 2.1.1 the origin of Bose-Einstein condensation of an ideal gas as a statistical phenomenon was introduced. However, typical experiments work with weakly interacting atomic species, and to correctly describe the condensates, these interaction must be taken into account. The many-body Hamiltonian for a system of N interacting bosons in an external trapping potential $V_{\text{ext}}(\mathbf{r})$ is given in second quantisation by [43]

$$\hat{H} = \int d\mathbf{r} \hat{\Psi}^\dagger(\mathbf{r}) \left[-\frac{\hbar^2}{2m} \nabla^2 + V_{\text{ext}}(\mathbf{r}) \right] \hat{\Psi}(\mathbf{r}) + \frac{1}{2} \int d\mathbf{r} d\mathbf{r}' \hat{\Psi}^\dagger(\mathbf{r}) \hat{\Psi}^\dagger(\mathbf{r}') V(\mathbf{r} - \mathbf{r}') \hat{\Psi}(\mathbf{r}') \hat{\Psi}(\mathbf{r}). \quad (2.12)$$

Here $\hat{\Psi}(\mathbf{r})$ and $\hat{\Psi}^\dagger(\mathbf{r})$ are annihilation and creation field operators for particles at position \mathbf{r} . The first integral describes the single-particle Hamiltonian of a particle moving in an external potential, and the second integral corresponds to the pair-wise interaction between particles through the two-body inter-atomic scattering potential $V(\mathbf{r} - \mathbf{r}')$. In the regime of ultracold gases, these cold collisions are completely dominated by s -wave scattering events, which are parametrised by a single parameter a called the *s-wave scattering length*. For ^{87}Rb , the scattering length is on the order of $100 a_0$ with a_0 being the Bohr radius. Since the inter-atomic separation in ultracold gases is typically much larger than the scattering length, the scattering events can be treated as contact interactions through the effective potential

$$V(\mathbf{r} - \mathbf{r}') = U_0 \delta(\mathbf{r} - \mathbf{r}') \quad (2.13)$$

with the interaction energy given by $U_0 = \frac{4\pi\hbar^2}{m}$ where m is the atomic mass, and $\delta(x)$ denotes the Dirac delta function. This constitutes a significant simplification, since the Hamiltonian in Eq. (2.12) becomes local.

Following an idea first introduced by N. N. Bogoliubov [44], the field operator is separated into a classical field $\Phi(\mathbf{r})$ for the condensate and

a fluctuation term $\delta\hat{\Psi}(\mathbf{r})$ for the excitations, since the ground state is macroscopically populated

$$\hat{\Psi}(\mathbf{r}, t) = \Phi(\mathbf{r}, t) + \delta\hat{\Psi}(\mathbf{r}, t). \quad (2.14)$$

The complex function $\Phi(\mathbf{r})$ is equal to the expectation value of the field operator $\Phi(\mathbf{r}) = \langle \hat{\Psi}(\mathbf{r}) \rangle$ and determines the condensate density $n_c(\mathbf{r})$ through

$$n_c(\mathbf{r}, t) = |\Phi(\mathbf{r}, t)|^2. \quad (2.15)$$

$|\Phi(\mathbf{r}, t)|^2$ is also referred to as the order parameter.

For very low temperatures, the excitations can be treated as a small perturbation of the system. If we neglect them for $T \rightarrow 0$ and use the Heisenberg equation of motion we obtain the time-dependent Gross-Pitaevskii equation (GPE)

$$i\hbar \frac{\partial}{\partial t} \Phi(\mathbf{r}, t) = \left(-\frac{\hbar^2}{2m} \nabla^2 + V_{\text{ext}}(\mathbf{r}) + U_0 |\Phi(\mathbf{r})|^2 \right) \Phi(\mathbf{r}, t). \quad (2.16)$$

Within this mean field theory the condensate wave function can be written as $\Phi(\mathbf{r}, t) = \psi(\mathbf{r}) \exp(-i\mu t/\hbar)$, and the stationary GPE is obtained

$$\mu\psi(\mathbf{r}) = \left(-\frac{\hbar^2}{2m} \nabla^2 + V_{\text{ext}}(\mathbf{r}) + U_0 n_c(\mathbf{r})^2 \right) \psi(\mathbf{r}). \quad (2.17)$$

The GPE can be extended to finite temperatures by keeping the fluctuation term in Eq. (2.14). Within the Popov approximation the resulting condensate equation is [45, 46]

$$\mu\psi(\mathbf{r}) = \left(-\frac{\hbar^2}{2m} \nabla^2 + V_{\text{ext}}(\mathbf{r}) + U_0 [n_c(\mathbf{r})^2 + 2n_{\text{th}}(\mathbf{r})] \right) \psi(\mathbf{r}). \quad (2.18)$$

2.2.1 The Thomas-Fermi approximation

For repulsive interactions and large atom numbers, the kinetic energy term in the GPE becomes negligible. The simplification arising from

dropping the relevant term from Eq. (2.17) is called the *Thomas-Fermi approximation*, and leads to a simple expression for the condensate density

$$n_c(\mathbf{r}) = \frac{\mu - V_{\text{ext}}(\mathbf{r})}{U_0} \Theta(\mu - V_{\text{ext}}(\mathbf{r})), \quad (2.19)$$

where $\Theta(x)$ is the Heaviside step function.

For a harmonic potential the condensate density assumes the shape of an inverted parabola. The Thomas-Fermi radii are given by the condition $\mu - V_{\text{ext}}(\mathbf{r}) = 0$

$$R_i = \frac{2\mu}{m\omega_i^2}, \quad i = x, y, z. \quad (2.20)$$

From the normalisation condition $N_0 = \int d\mathbf{r} n_c(\mathbf{r})$ the expression for the chemical potential within the Thomas-Fermi approximation is obtained

$$\mu = \frac{15^{2/5}}{2} \left(\frac{Na}{a_{\text{ho}}} \right)^{2/5} \hbar\bar{\omega}, \quad (2.21)$$

where $a_{\text{ho}} = \sqrt{\frac{\hbar}{m\bar{\omega}}}$ is the harmonic oscillator length.

2.2.2 Shift of the critical temperature due to interactions

Interactions induce a shift in the critical temperature, and the direction of the shift can be understood intuitively; A positive scattering length causes the atoms to repel each other, reducing the central density in a ultracold cloud, which in turn reduces the critical temperature for condensation. For negative scattering length the opposite is true; the increased central density leads to condensation at a higher temperature. The first order mean field shift is given by [47]

$$\frac{\Delta T_c^{\text{int}}}{T_c} \approx -1.33 \frac{a}{a_{\text{ho}}} N^{1/6}. \quad (2.22)$$

Contrary to the shift due to the finite size of the system (see Eq. (2.11)), this shift is independent of the trap anisotropy, and does not vanish in the limit of $N \rightarrow \infty$. Note that higher order corrections push the shift in the opposite direction [48].

The shift is furthermore related to a change in the condensate fraction. The first-order mean field correction to the condensate fraction is [43]

$$\frac{N_0}{N} = 1 - \left(\frac{T}{T_c}\right)^3 - \eta \frac{\zeta(2)}{\zeta(3)} \left(\frac{T}{T_c}\right)^2 \left(1 - \left(\frac{T}{T_c}\right)^2\right)^{2/5}, \quad (2.23)$$

where $\eta = \frac{\mu}{k_B T_c}$. The observation of beyond mean-field contributions to both the shift in the critical temperature and the condensate fractions was reported in [49, 50].

Figure 2.2 shows a measurement of the condensate fraction compared to the simple ideal gas result (Eq. (2.7)) and the prediction with the corrections due to finite size-effects and interactions given by Eq. (2.10) and Eq. (2.23). While the ideal gas model already captures the general behaviour of the data, the agreement is improved by the inclusion of the two corrections for larger condensate fractions. A more detailed comparison between experiment and theory can be done by treating the interactions between the condensate atoms and the thermal atoms with self-consistent methods. Detailed experimental investigations of the condensate fraction was reported in [20–22].

2.3 Fluctuations of Bose-Einstein condensates

The preceding sections dealt with the determination of average properties of BECs such as the condensate fraction and the critical temperature. All results were obtained within the grand canonical ensemble (GCE), which generally works well for the mean properties of the system. This is as a surprising fact when the nature of the system we are considering is taken

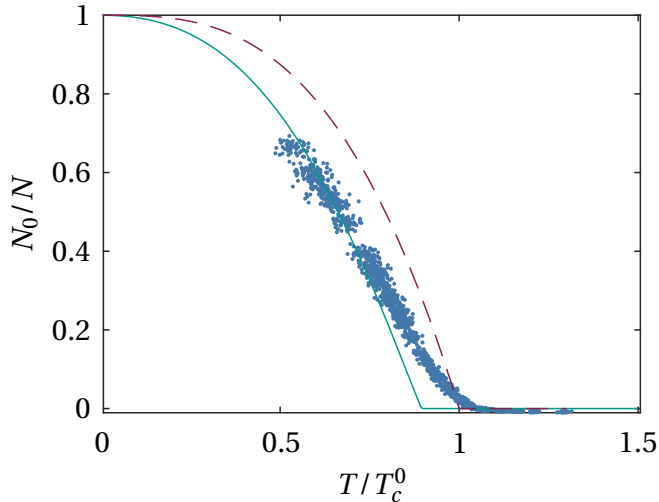


Figure 2.2: The condensate fraction as a function of the reduced temperature. The blue points (\bullet) are measured values, the purple dashed curve (---) is the simple ideal gas result Eq. (2.7), and the teal curve (—) includes the first order corrections due to finite size effects (Eq. (2.10)) and interactions (Eq. (2.23)).

into account, and it is worthwhile to pause and discuss the applicability of the grand canonical ensemble to trapped BECs.

The GCE represents a system in thermal and diffusive equilibrium with a reservoir. The system is able to exchange both particles and energy with the reservoir, and the total atom number and energy is therefore not constrained. Contrast this with the experimental realisation of BEC, where a trapped atom cloud is completely isolated from the surroundings. Clearly, the total atom number is fixed, and the validity of the GCE is questionable. To get a more accurate statistical representation of the system, we must adopt a description based on the canonical ensemble (CE) or micro canonical ensemble (MCE), where the total atom number

is fixed. The fluctuations of the ground state occupation of a BEC is a striking example of the shortcomings of the grand canonical description.

2.3.1 Grand canonical fluctuations of the ideal gas

The grand canonical prediction of the number fluctuations is a common textbook exercise [51]. The variance of the occupation of a state i is

$$\Delta N_i^2 = N_i(N_i + 1). \quad (2.24)$$

For temperatures $T \gg T_c$, the excited states $i > 0$ can be viewed as a reservoir in contact with the population in the ground state, and Eq. (2.24) gives an accurate description of the ground state occupation fluctuations. However, for an atomic Bose-Einstein condensed system where $N_0 \rightarrow N$ as $T \rightarrow 0$, this prediction leads to the absurd conclusion that the fluctuations ΔN_0 of the ground state are equal to the total atom number of the system. As the temperature approaches zero the fluctuations of the ground state must vanish [52]. This flaw of the GCE is at times referred to as the grand canonical catastrophe [39, 52].

The discussion of the GCE's inadequacy in describing ideal gases with Bose-Einstein condensates is an old issue. Ziff, Uhlenback and Kac showed that the GCE loses its validity for Bose-Einstein condensed systems even in the thermodynamic limit [38]. A more accurate description must therefore be based on a canonical or micro-canonical ensemble, which retains their equivalence in the thermodynamic limit. This makes Bose-Einstein condensation an interesting example of a system, where we do not have complete freedom in the choice of statistical ensemble.

To observe the grand canonical statistics, the particle number must be unconstrained. This has been achieved in a photon BEC, where the condensate of photons is created in a dye filled micro cavity [53, 54]. In these systems, photons are absorbed and re-emitted by the dye molecules, and the conserved quantity is the sum of the number of photons and

molecular excitations. Therefore, the photon number is not conserved, and the molecular excitations serve as the particle reservoir, realising grand canonical statistics.

One intuitive approach to remedy the “catastrophe” for $T \ll T_c$ is to reverse the role of the condensate and thermal excitations. For $T \ll T_c$, the condensate fraction is large and can be viewed as a reservoir for non-condensed atoms. This is the starting point for several canonical treatments of the fluctuations problem [55, 56].

The idea can be exploited somewhat further. Using the grand canonical results for the condensate number and chemical potential, but explicitly introducing particle number conservation $N = N_0 + N_{\text{th}}$, the fluctuations can be calculated for low temperatures, as outlined in [39]. Due to the atom number constraint, the prediction corresponds to a canonical estimate of the fluctuations. It can be evaluated analytically to good approximation for an isotropic trap. Naturally, this is expected to fail as $T \rightarrow T_c$ from below due to the depletion of the condensate, as is seen in Fig. 2.3.

2.3.2 Canonical and micro canonical fluctuations

As outlined above, a proper description of the statistics of BECs must use the canonical or micro canonical ensemble. The creation of the first BECs in 1995 sparked a renewed interest in the problem of the BEC fluctuations. In the following I present a brief overview of the most important approaches to tackling this problem.

The leading contribution

The first result for the leading contribution to the canonical fluctuations of a harmonically confined non-interacting cloud at $T \ll T_c$ was obtained by Politzer [55]. He exploited the idea outlined above, and determined the fluctuations of the excited states using the grand canonical

result Eq. (2.24), for which the occupation of individual states $i > 0$ is always small. However, the ground state occupation is determined not by the chemical potential, but the requirement that $N_0 = N - N_{\text{th}}$, which also has the consequence that $\Delta N_0 = \Delta N_{\text{th}}$. The leading contribution is thus

$$\Delta N_0^2 = \frac{\zeta(2)}{\zeta(3)} N \left(\frac{T}{T_c} \right)^3, \quad (2.25)$$

where $\frac{\zeta(2)}{\zeta(3)} = 1.37$.

Microcanonical fluctuations: The Maxwell's demon ensemble

Similar ideas were used to introduce the Maxwell's Demon ensemble [57], which can be viewed as a fourth statistical ensemble. By separating the system into the ground state BEC and the excited states, an ensemble where the excited states can exchange particles only with the ground state without exchange of energy can be constructed. The name is inspired by the famous Maxwell's demon, since the process corresponds to keeping track of the energy of the particles. The predictions using this approach reproduces Eq. (2.25) in the canonical ensemble. However, the Maxwell's demon ensemble also yields an analytical expression for the leading contribution of the micro canonical fluctuations at low temperatures

$$\Delta N_{0,\text{MC}}^2 = \left(\frac{\zeta(2)}{\zeta(3)} - \frac{3\zeta(3)}{4\zeta(4)} \right) N \left(\frac{T}{T_c} \right)^3. \quad (2.26)$$

$\frac{\zeta(2)}{\zeta(3)} - \frac{3\zeta(3)}{4\zeta(4)} = 0.54$. The fluctuations calculated within the MCE is thus smaller than the corresponding result in the CE.

Exact recursion relations

It was later shown that the fluctuations of the non-interacting trapped gas can be calculated exactly using numerical methods within the CE.

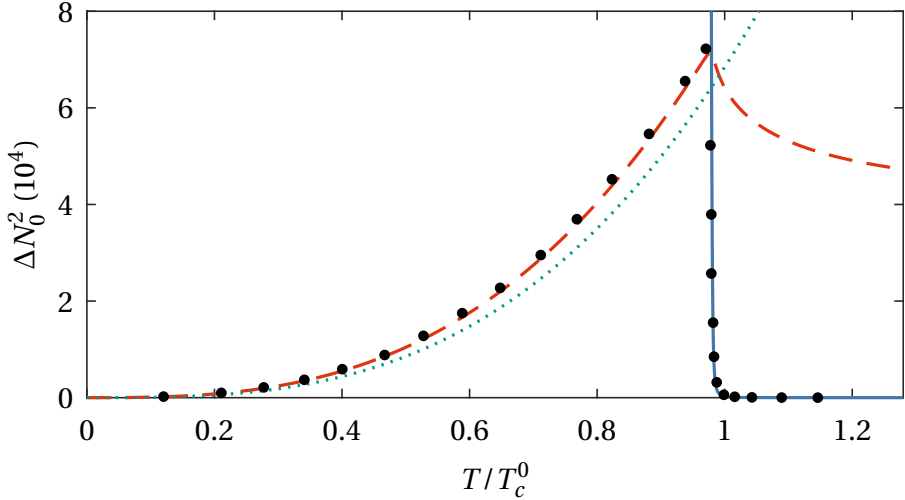


Figure 2.3: The BEC fluctuations of a non-interacting gas of $N = 50,000$ atoms in a isotropic harmonic trap. (—) The grand canonical prediction given by Eq. (2.24) clearly fails below T_c . (---) The modified grand canonical prediction, where the condensate is treated as a reservoir for thermal excitations. The curve corresponds to the analytic approximation of an isotropic trap in [39, appendix D]. (⋯) The leading contribution to the fluctuations below T_c given by Eq. (2.25). (●) An exact canonical calculation based on the recursion relations of [40]. The calculation was provided by K. Pawłowski and K. Rzążewski (private correspondence).

Using a set of recursion relations, Weiss and Wilkens [40] developed the numerical tools to calculate the fluctuations.

Figure 2.3 shows a comparison of the most important predictions for the non-interacting gas in an isotropic harmonic trap. The grand canonical fluctuations Eq. (2.24) and the fluctuations based on the reversal of roles of the condensate and excited states constitute two limiting cases for

2.3. Fluctuations of Bose-Einstein condensates

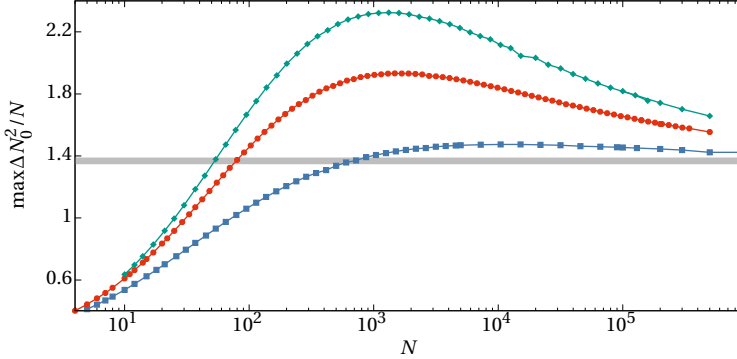


Figure 2.4: Peak fluctuations scaled with the atom number for harmonic traps with aspect ratio $\lambda = 1$ (\blacksquare), $\lambda = 5.27$ (\bullet) and $\lambda = 7.64$ (\blacklozenge). The horizontal grey line is the corresponding asymptotic value $\zeta(2)/\zeta(3)$ given in Politzer [55].

the high- and low-temperature limits. The Politzer expression Eq. (2.25) captures most of the low temperature behaviour, but only the exact calculation shows the defining quench of the fluctuations at T_c .

The exact calculations can be performed for anisotropic traps. Fig. 2.4 shows the influence of trap anisotropy on the fluctuations, where the peak fluctuations were calculated exactly for experimentally relevant trapping frequencies. The peak fluctuations are greater for traps with larger aspect ratios $\lambda = \omega_\rho/\omega_z$, where ω_ρ and ω_z are the radial and axial trapping frequencies of a cigar shaped harmonic trap. The enhancement of the fluctuations is interpreted as a consequence of the reduction of the dimensionality of the trap due to the anisotropy and finite atom number. For large atom numbers the fluctuations approach the limiting value $\zeta(2)/\zeta(3)$ expected for infinite N .

2.3.3 Fluctuations in the interacting BEC

The preceding discussion focused solely on the non-interacting Bose gas, but the experimentally most relevant situation is a weakly interacting gas in a harmonic trap. Unfortunately, no exact solution in the form of the recursion relations exist for the interacting gas, and theoretical predictions therefore resort to various approximations. Hence, most theoretical results to date are obtained for the homogeneous case.

Giorgini et al. [47] calculated the low-temperature dependence of the fluctuations in the homogeneous and harmonically confined case. Their theory is based on a Bogoliubov quasiparticle approach, and reproduces the result of Polizter for the non-interacting Bose gas. Surprisingly, they find that the fluctuations scale anomalously with atom number as $\Delta N_0^2 \propto N^{4/3}$ for the weakly interacting Bose gas in both the homogeneous and harmonic case.

This was challenged by Idziaszek et al. [58], who calculated the fluctuations in homogeneous gas with a method similar to the Maxwell's Demon approach of [57], and found a normal scaling with atom number $\Delta N_0^2 \propto N$. The anomalous fluctuations became a point of controversy. Note that the fluctuations of the non-interacting gas scale anomalously in the homogeneous case, but exhibit normal scaling under harmonic confinement.

The methods of Giorgini et al. [47] were extended in a series of papers by Kocharovsky et al. [59–61] using two approaches, one based on a number-conserving canonical quasiparticle approach and one based on an analogy between the second order phase transition of Bose-Einstein condensation and the behaviour of lasers at threshold. More recently, the two methods were combined into a hybrid master equation approach [39, 62, 63]. They find the same anomalous scaling as the earlier results.

Other recent works by Xiong et al. [64] and Liu et al. [65] also find that an anomalous scaling of the fluctuations. However, other authors put emphasis on the point that the fluctuations must scale normally for the

weakly interacting system to be stable [66–69]. Today there appears to be consensus, that the fluctuations are anomalously large, at least for low temperature and small atom numbers [39, 70], but it is not clear how this scaling approaches normal scaling expected for $T \rightarrow T_c$. In practice no theory as of yet is able to take into account all aspects of the problem of calculation of the fluctuations of BECs with interactions. The fundamental difficulty is the determination of the correct energy spectrum. As an example, one of the most recent results by Bhattacharyya and Chakrabarti [71] make use of the Thomas-Fermi approximation to calculate the fluctuations for a large number of weakly interacting particles, but the validity of the approximation close to T_c can be questioned.

To analyse our experimental results, we collaborate with the group led by Kazimierz Rzążewski who has calculated the fluctuations using the CFA method [72–74]. The classical fields approximation (CFA) works perfectly in lower dimensions, but is only feasible for a limited number of particles in 3D. Therefore, the calculations were only performed for particle numbers up to $N = 200$ atoms. This method can be seen as complementary to the method of Bhattacharyya and Chakrabarti [71], since it treats the interactions better at the transition, but only for low particle number. To get values that compare with our experiment, the scattering length a_s was increased to produce the same interactions strength $n(0)^{1/3} a_s$, where $n(0)$ is the density in the centre of the trap.

Figure 2.5 shows a comparison of the maximal fluctuations relative to the non-interacting gas, as reported by different groups. The results are plotted as a function of the interaction strength $n(0)^{1/3} a$, where $n(0)$ is the central density and a is the scattering length. The results scatter along the x -axis without revealing any trends, indicating that the interactions has a limited influence on the fluctuations. The deviation from the non-interacting result is within $\pm 20\%$ which is comparable to the influence of the anisotropy of our trap.

In summary, the fluctuations are well understood only for the non-interacting Bose gas in homogeneous and harmonically confined systems,

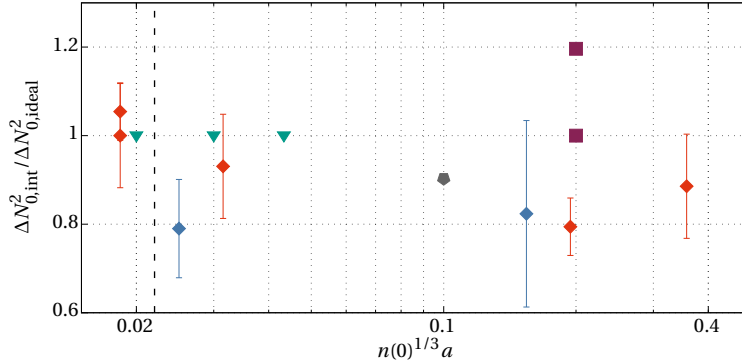


Figure 2.5: Fluctuations of the number of condensed particles in the interacting system relative to the non-interacting as a function of the interaction strength $n(0)^{1/3} a_s$, where $n(0)$ is a density in the centre of the trap. (♦) and (♦) are results obtained within the classical field approximation for $N = 100$ and $N = 200$ atoms. The error bars correspond to typical jump of the final results after averaging in Monte-Carlo simulations (see supplementary material of [75]). The other points correspond to ▼ [71], ■ [58], ◆ [62]. The interaction strength typical for our experiments is indicated by the dashed line.

where numerical recursion relations allows for exact calculations. No exact methods exist for the fluctuations of the interacting Bose-gas, and in particular the difficulties in determining the energy spectrum of the interacting gas makes the theoretical models uncertain for the experimentally most relevant systems. Interactions may lead to anomalous scaling of the fluctuations with atom number, at least at low particle numbers and temperatures. Finally, the anisotropy of the harmonic confinement may have as large an effect on the fluctuations as the interactions. With the wide range of unresolved theoretical challenges and questions, this highlights the necessity of experimental inputs.

2.4 Cloud profiles

To extract the information about ultracold gases the typical approach consist of using an imaging technique, that records the spatial density distribution of the gas. Different imaging methods are in use, and the two methods we use are treated in Section 3.3 and Chapter 4. However, to extract quantities such as atom number and temperature, it necessary to model the expected distributions both in trap and in TOF to define appropriate fitting functions.

Pure BEC

The condensate wavefunction for a non-interacting BEC is the ground state single particle wavefunction,

$$n_c(\mathbf{r}) = N_0 |\phi_0(\mathbf{r})|^2, \quad (2.27)$$

where $\phi_0(\mathbf{r})$ is the single particle wavefunction. In the case of a harmonic trap this is Gaussian, and the condensate wavefunction is thus also Gaussian. The expansion in TOF depends on the momentum distribution, which is the Fourier transform of Eq. (2.27). The momentum distribution is thus broader along tightly confined axes, which leads to a larger expansion along these axes during free fall. For a cigar-shaped cloud, the aspect ratio inverts, and the condensate goes from an elongated cigar-shape to a pancake shape. This is an interesting manifestation of the Heisenberg uncertainty relation.

Interactions significantly change the ground state. Fortunately, the Thomas-Fermi approximation is often applicable, in which the condensate density distribution given by Eq. (2.19). For a harmonic trapping potential $V_{\text{ext}}(\mathbf{r}) = \frac{m}{2} \sum_{i=x,y,z} \omega_i^2 r_i^2$, the condensate density profile is an inverted parabola

$$n_c(\mathbf{r}) = \frac{15}{8\pi} \frac{N_0}{R_x R_y R_z} \max\left(0, 1 - \frac{x^2}{R_x^2} - \frac{y^2}{R_y^2} - \frac{z^2}{R_z^2}\right). \quad (2.28)$$

with the Thomas-Fermi radius $R_i = \frac{2\mu}{m\omega_i^2}$ (Eq. (2.20)).

The expansion of an interacting BEC is dominated by the conversion of the mean-field energy into kinetic energy and the above argument for the non-interacting BEC is not applicable. However, the weakly interacting BEC still undergoes a similar inversion of the anisotropy. The mean field interaction energy creates a pressure gradient across the condensate. Since this is proportional to the local density, the gradient is larger in the directions of tight confinement, which leads to a faster expansion in these directions [41]. The density profile retains the parabolic shape during TOF expansion. For a cigar-shaped condensate ($\omega_x = \omega_y = \omega_\rho$), the radii after expansion can be expressed as a rescaling of the in-trap extent [76]

$$\begin{aligned} R_\rho(t) &= R_\rho(0) \sqrt{1 + \tau^2} \\ R_z(t) &= \frac{R_\rho(0)}{\varepsilon} \left(1 + \varepsilon^2 \left[\tau \arctan \tau - \ln \sqrt{1 + \tau^2} \right] \right) \end{aligned} \quad (2.29)$$

with $\tau = \omega_\rho t$ and $\varepsilon = \omega_z/\omega_\rho$ and $R_x(t) = R_y(t) = R_\rho(t)$.

Thermal cloud

In principle, to determine the thermal distribution requires one to perform a summation over single particle wavefunctions with occupations given by Eq. (2.1). In practice, we can often replace the discrete sum with an integral via a semi-classical approximation. To determine the thermal density distribution, we apply the semi-classical approximation, where the discrete energies in Eq. (2.1) are replaced by the continuous energy of a particle in an effective potential $V_{\text{eff}}(\mathbf{r})$ [41].

$$\varepsilon(\mathbf{p}, \mathbf{r}) = \frac{p^2}{2m} + V_{\text{eff}}(\mathbf{r}) \quad (2.30)$$

The semi-classical approximation is valid when the thermal energy is much larger than the level spacing of the potential.

To obtain the spatial density distribution, $f^0(\mathbf{p}, \mathbf{r})$ (Eq. (2.1)) is integrated over momentum using the fact that $f^0(\mathbf{p}, \mathbf{r})d\mathbf{p}d\mathbf{r}/(2\pi\hbar^3)$ is the number of particles in a phase space volume element.

$$n_{\text{th}}(\mathbf{r}) = \int \frac{d\mathbf{p}}{(2\pi\hbar)^3} \frac{1}{e^{(p^2/2m + V_{\text{eff}}(\mathbf{r}) - \mu)/k_B T} - 1}. \quad (2.31)$$

The solution to the integral is

$$n_{\text{th}}(\mathbf{r}) = \frac{1}{\lambda_T^3} g_{3/2} \left(e^{(\mu - V_{\text{eff}}(\mathbf{r})/k_B T)} \right), \quad (2.32)$$

where the thermal de Broglie wavelength is $\lambda_T = \sqrt{\frac{2\pi\hbar^2}{mk_B T}}$, and $g_\gamma(x)$ is defined in Eq. (2.9).

For a 3D harmonic confining potential, Eq. (2.32) becomes a Bose-enhanced Gaussian distribution. In terms of the atom number N and the cloud widths $\sigma_i = \sqrt{\frac{k_B T}{m\omega_i^2}}$ it is given by

$$n_{\text{th}}(\mathbf{r}) = \frac{N}{(2\pi)^{3/2} \sigma_x \sigma_y \sigma_z g_3(\tilde{z})} g_{3/2} \left(\tilde{z} e^{-\sum_{i=x,y,z} r_i^2 / 2\sigma_i^2} \right), \quad (2.33)$$

where the fugacity $\tilde{z} = e^{\mu/k_B T}$ has been introduced. For high temperatures $T \gg T_c$ the fugacity $\tilde{z} \ll 1$ and only the first term of the Bose function contributes. Then Eq. (2.33) reduces to a simple Gaussian distribution, as we would have obtained from the classical Maxwell-Boltzmann distribution

$$n_{\text{th}}^{\text{MB}}(\mathbf{r}) = \frac{N}{(2\pi)^{3/2} \sigma_x \sigma_y \sigma_z} e^{-\sum_{i=x,y,z} r_i^2 / 2\sigma_i^2}, \quad (2.34)$$

Figure 2.6 on Page 30 compares the Bose Enhanced (Eq. (2.33)) for $\tilde{z} = 1$ and classical (Eq. (2.34)) distributions. This clearly illustrates the enhancement of the central density of the Bose Enhanced distribution.

To determine the density distribution of thermal clouds after expansion in TOF, we assume that the cloud expands ballistically without collisions. Then the distribution function will be constant in time [41]. For

an atom to be found with momentum and position \mathbf{p} and \mathbf{r} at time t it must follow a path from it's initial position \mathbf{r}_0 given by $\mathbf{r} = \mathbf{r}_0 + \mathbf{p}t/m$. The distribution function at time t is thus given by

$$f(\mathbf{r}, \mathbf{p}, t) = f_0(\mathbf{r} - \mathbf{p}t/m, \mathbf{p}) = \frac{1}{e^{(p^2/2m + V_{\text{eff}}(\mathbf{r} - \mathbf{p}t/m) - \mu)/k_B T} - 1}. \quad (2.35)$$

Modifying Eq. (2.31) accordingly, the density is given by

$$n_{\text{th}}(\mathbf{r}, t) = \int \frac{d\mathbf{p}}{(2\pi\hbar)^3} \frac{1}{e^{(p^2/2m + V_{\text{eff}}(\mathbf{r} - \mathbf{p}t/m) - \mu)/k_B T} - 1}. \quad (2.36)$$

For a harmonic potential, this can be solved by a change of coordinates that separates momentum and spatial coordinates, and the solution is given by Eq. (2.33)

$$n_{\text{th}}(\mathbf{r}) = \frac{N}{(2\pi)^{3/2} w_x w_y w_z g_3(\tilde{z})} g_{3/2} \left(\tilde{z} e^{-\sum_{i=x,y,z} r_i^2/2w_i^2} \right), \quad (2.37)$$

with widths given by

$$w_i(t) = \sqrt{\frac{k_B T}{m\omega_i} \left(\frac{1}{\omega_i^2} + t^2 \right)} = \sigma_i \sqrt{\frac{1}{\omega_i} + t^2}. \quad (2.38)$$

Partially condensed BEC

At finite temperatures, the density distribution is bimodal with a high central density due to the condensate and lower density wings of thermal atoms. The condensate density in-trap in the presence of the thermal atoms is given by Eq. (2.18), while the thermal density is given by Eq. (2.32) with the effective potential taking the mean field interaction into account [45, 46, 77]

$$V_{\text{eff}}(\mathbf{r}) = V_{\text{ext}}(\mathbf{r}) + 2U_0 [n_c(\mathbf{r}) + n_{\text{th}}(\mathbf{r})]. \quad (2.39)$$

This yields a set of coupled equations, that can be solved self-consistently in an iterative fashion using numerical methods [46]

$$n_c(\mathbf{r}) = \frac{\mu - V_{\text{ext}}(\mathbf{r}) - 2U_0 n_{\text{th}}(\mathbf{r})}{U_0} \Theta(\mu - V_{\text{ext}}(\mathbf{r}) - 2U_0 n_{\text{th}}(\mathbf{r})) \quad (2.40)$$

$$n_{\text{th}}(\mathbf{r}) = \frac{1}{\lambda_T^3} g_{3/2} \left(e^{(\mu - V_{\text{ext}}(\mathbf{r}) - 2U_0 [n_c(\mathbf{r}) + n_{\text{th}}(\mathbf{r})]) / k_B T} \right), \quad (2.41)$$

where $\Theta(x)$ is the Heaviside step function.

The semi-ideal model provides an analytic approximate solution of Eqs. (2.40) and (2.41) [78]. Since the thermal density is much lower than the condensate density it can be neglected from Eq. (2.40), which reduces to the density of a pure BEC given by Eq. (2.28). If $n_{\text{th}}(\mathbf{r})$ is also neglected in Eq. (2.39), the system of equations can be solved analytically. The effective potential and thermal density within the semi-ideal model is thus

$$V_{\text{eff}}(\mathbf{r}) = V_{\text{ext}}(\mathbf{r}) + 2U_0 n_c(\mathbf{r}), \quad (2.42)$$

$$\begin{aligned} n_{\text{th}}(\mathbf{r}) &= \frac{1}{\lambda_T^3} g_{3/2} \left(e^{(\mu - V_{\text{ext}}(\mathbf{r}) - 2U_0 n_c(\mathbf{r})) / k_B T} \right) \\ &= \frac{1}{\lambda_T^3} g_{3/2} \left(e^{-|V_{\text{ext}}(\mathbf{r}) - \mu| / k_B T} \right), \end{aligned} \quad (2.43)$$

where Eq. (2.19) is used in the last step. The semi-ideal model has been used to study BECs using dispersive techniques [22, 34]. Figure 2.6 compares the semi-ideal density distribution (Eq. (2.43)) with the Bose-enhanced Gaussian distribution with $\mu = 0$ and the classical density distribution (Eq. (2.34)). The semi-ideal model captures the repulsion of the thermal atoms by the BEC with a reduced density at the centre.

The semi-ideal model does not yield an analytic solution for the thermal density in TOF, since it requires solving the integral Eq. (2.36) using Eq. (2.42). However, due to the rapid decrease of the density, the “hole”

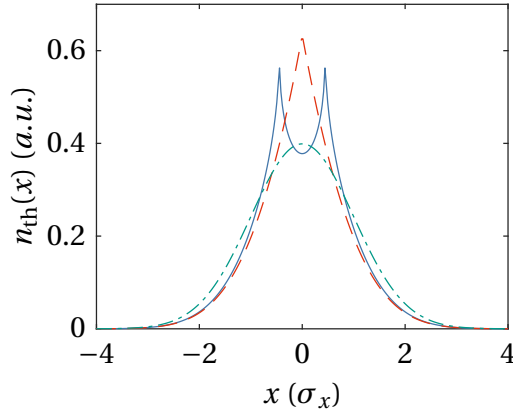


Figure 2.6: Comparison of different models for the thermal density. — Semi-ideal model with $\mu = 0.1k_B T$ (Eq. (2.43)). - - - Bose-enhanced Gaussian distribution with $\mu = 0$. - · - · Classical distribution based on Maxwell-Boltzmann statistics (Eq. (2.34)). All distribution has been normalised to $\int dx n_{\text{th}}(x) = 1$.

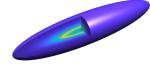
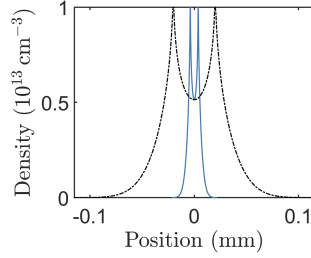
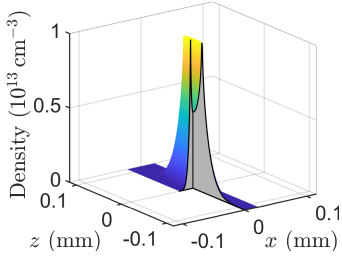
in the distribution seals during the expansion. Therefore, it is customary to fit the experimental images using [79, 80]

$$n(\mathbf{r}, t) = n_c(\mathbf{r}, t) + n_{\text{th}}(\mathbf{r}, t) \quad (2.44)$$

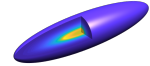
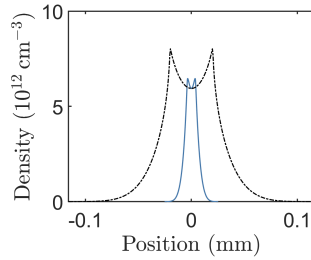
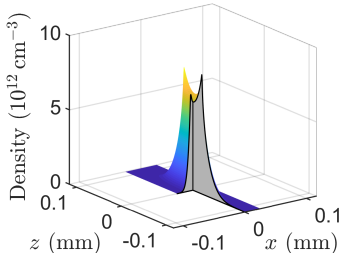
with $n_c(\mathbf{r}, t)$ given by Eq. (2.28) to model the condensate density and $n_{\text{th}}(\mathbf{r}, t)$ given by Eq. (2.33) with $\mu = 0$ to model the thermal density, referred to as the ideal or non-interacting model [21, 22]. In Section 2.4.1 the discrepancy from the semi-ideal model is studied numerically.

Optical imaging methods probe the column densities $\tilde{n}(x, y) = \int dz n(\mathbf{r})$, which are given for the relevant distributions in Appendix A.

TOF = 0 ms



TOF = 1 ms



TOF = 2 ms

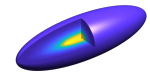
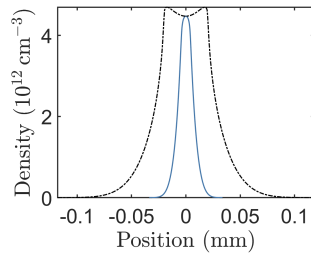
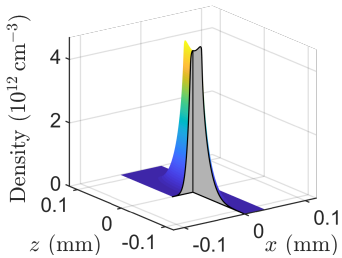
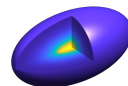
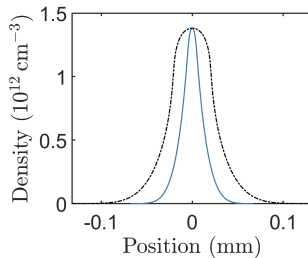
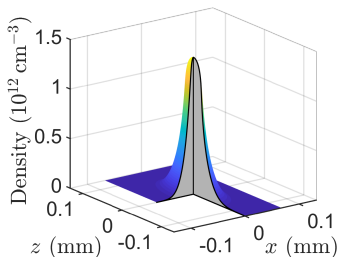


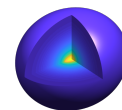
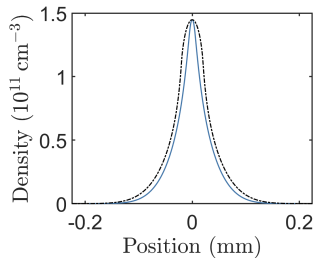
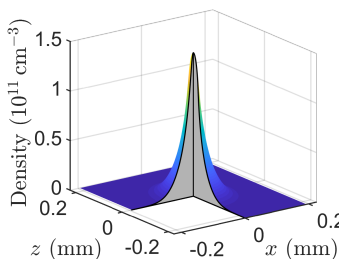
Figure 2.7: Numerical integration of Eq. (2.36) with the effective potential given by Eq. (2.42), for TOF between 0 ms and 5 ms. Left column shows surface plots of the thermal density with a cut out. The middle column show cross sections along the radial x axis (—) and the axial z direction (---). Left column illustrate the 3D density distribution.

2. FORMATION AND FLUCTUATIONS OF BOSE-EINSTEIN CONDENSATES

TOF = 5 ms



TOF = 15 ms



TOF = 27.5 ms

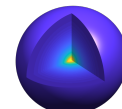
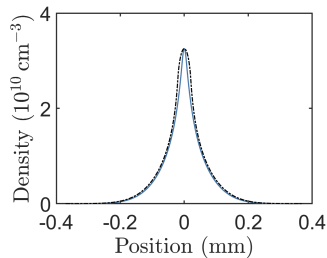
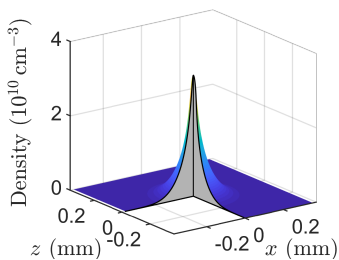


Figure 2.8: Numerical integration of Eq. (2.36) with the effective potential given by Eq. (2.42), for TOF between 10 ms and 27.5 ms. Left column shows surface plots of the thermal density with a cut out. The middle column show cross sections along the radial x axis (—) and the axial z direction (- - -). Left column illustrate the 3D density distribution.

2.4.1 Semi-ideal model in TOF

To estimate the validity of Eq. (2.44) for modelling TOF distributions of BECs, Eq. (2.36) is integrated numerically with the effective potential given by Eq. (2.42). This is an idealised model where the repulsion of the thermal cloud by the BEC is included in-trap, but completely neglected during expansion. While this is reasonable for longer expansion times, where the density drops several orders of magnitude, it will be inaccurate for the initial expansion. Despite this, these results provide a useful estimate of the systematic error on inferring cloud properties from fits of Eq. (2.44).

For the integration of Eq. (2.36) the TOF t , atom number N and reduced temperature T/T_c is chosen. In this case, $N = 1.194 \times 10^5$ and $T/T_c = 0.8$. The condensate atom number is determined numerically from the semi-ideal model [78, Eq. (12)] to $N_0 = 3.5218 \times 10^4$, corresponding to a 29.5 % BEC fraction.

The integration problem has cylindrical symmetry in the spacial coordinates for a cigar-shaped trapping geometry with $\omega_x = \omega_y = 2\pi \times 93.4$ Hz and $\omega_z = 2\pi \times 17.7$ Hz. It is therefore sufficient to determine the density for $x \geq 0$, $y = 0$ and $z \geq 0$, which is achieved on a 200×200 grid. The full 3D density is constructed by rotation and reflection around the symmetry axis and is calculated on a resulting $499 \times 499 \times 499$ grid. The maximal grid spacing is $1.85 \mu\text{m}$ for $t = 27.5 \text{ms}$ ¹.

In momentum space, no symmetries can be exploited, and the momentum must be integrated numerically in all three dimensions. This is computationally demanding, and the calculation of density for a single set of parameters takes 1 to 2 days, highlighting the infeasibility of using this approach to fit experimental images².

¹This is smaller than the effective pixel size of the absorption imaging system which is $3.80 \mu\text{m}$, see Section 3.3.

²If the trap is spherical symmetric, the problem is significantly simplified. The density only needs to be calculated along a symmetry axis, and the momentum integral

Figures 2.7 and 2.8 show the evolution of the thermal density as surface plots, cross sections and 3D density plots for TOF ranging from $t = 0$ ms to 27.5 ms. At $t = 0$ ms the calculated density agrees exactly with the analytical expression given by Eq. (2.43). The “hole” seals during the first few milliseconds of expansion, and at $t = 5$ ms the profile assumes an anisotropic bell shape. At larger times the cloud becomes spherical due to the isotropic expansion. The pointed profile at $t = 27.5$ ms qualitatively agrees with the Bose-enhanced Gaussian profile (Eq. (2.33)) as seen in Fig. 2.6.

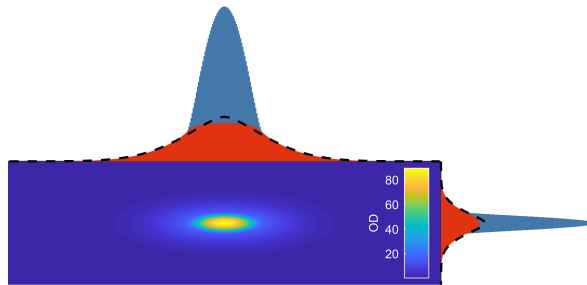


Figure 2.9: The image shows the optical density after 2 ms TOF for a cloud with a 29.5 % condensate fraction. The thermal density is determined by integrating Eq. (2.36) over momentum, while the condensate density is given by Eq. (2.28). The density is integrated along a radial direction to yield the column density, displayed in units of optical density $OD(x, z) = \tilde{n}(x, z)/\sigma_0$, where σ_0 is the resonant scattering cross section (see Section 3.3 for details.) The integrated column densities along the two directions is shown at the edge of the image, with ■ indicating thermal density and ■ indicating the condensate density. (---) is a fit of Eq. (A.3) to the thermal density.

To quantify the agreement, the column density is calculated by integrating the density over the radial direction. For a cloud with cylindrical symmetry, reducing the integral to a surface integral.

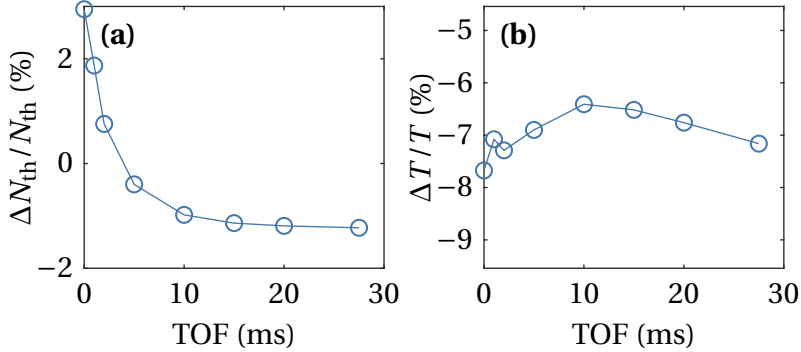


Figure 2.10: Error on **(a)** inferred thermal atom number N_{th} and **(b)** temperature T when fitting column densities using Eq. (A.3) as fit function, when the density is given by the semi-ideal model and expanded in TOF through integration of Eq. (2.36).

rating the densities along a radial axis. The column density is fitted with Eq. (A.3) in a region that excludes the condensate density. An example is shown in Fig. 2.9 for $t = 2$ ms. The fit agrees well with the density in the wings of the distribution, but makes a slight underestimation near the condensate boundary, while overestimating the central density. Figure 2.10 shows the error on the fitted temperature and atom number as a function of the TOF. For low t , the atom number is overestimated due to the repulsion of the thermal atoms by the condensate. For larger expansion times the error approaches a constant value of $\sim 1.2\%$. The error on the temperature estimation varies less, and is -8% to -6% across all expansion times. This indicates that the effect of the repulsion on the wings is small, but that the overall shape is different due to the difference in chemical potential of the semi-ideal distribution and the fitting model.

The same analysis is repeated to investigate the error on the fitted values of N and T when the temperature varies. In this case the expansion

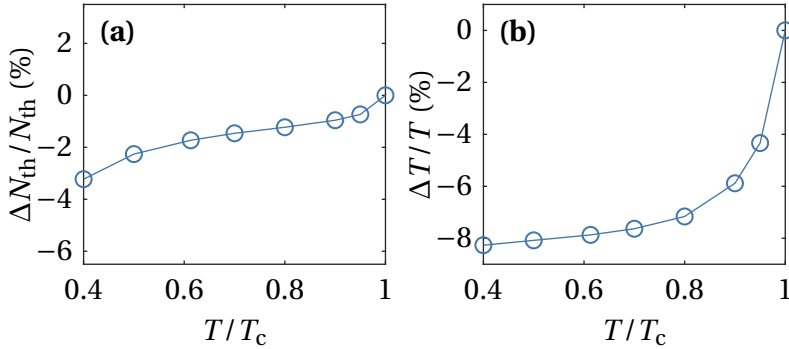


Figure 2.11: Error on **(a)** inferred thermal atom number N_{th} and **(b)** temperature T when fitting column densities using Eq. (A.3) as fit function, when the density is given by the semi-ideal model and expanded in TOF through integration of Eq. (2.36).

time is constant at $t = 27.5$ ms, while the reduced temperature is varied between $T/T_c = 0.4$ and $T/T_c = 1$. The total atom number and absolute temperature varies to match the atom number and temperature of the data shown in Fig. 2.2 on Page 16.

Figure 2.11 shows the result. At $T = T_c$, the semi-ideal model is equivalent to the fitting function, and exact agreement is found. As the temperature is reduced, both the thermal atom number N_{th} and the temperature T under-estimation increases. The error on the temperature estimation grows quickly until $T/T_c \approx 0.8$, where it levels off at a value around -8% . The error on the thermal atom is less affected, and is between -2% to -1% until $T/T_c \approx 0.5$, where it starts to grow.

While these results are still derived from idealized models, they show that properties of partially condensed BEC extracted from fitting images with Eq. (2.44) can be trusted taking systematic errors of a few percent into account.

PRODUCTION AND DETECTION OF ULTRACOLD GASES

This chapter opens with a brief overview of the experimental apparatus used for the experiments within this dissertation. At the time of writing, the apparatus where I have conducted my experiments has been producing BECs for 12 years, and was originally constructed by Henrik Kjær Andersen and Jesper Fevre Bertelsen. Since their theses give a thorough account of all aspects of the original design and implementation of the apparatus [81, 82], this chapter focuses on developments of the apparatus during my studies, and only a short general summary is given for completeness. For changes to apparatus between the initial construction and the period covered by this dissertation, the reader is referred to the theses of Poul Lindholm Pedersen and Miroslav Gajdacz [83, 84].

The next part of the chapter is devoted to the imaging systems used

for the detection of ultracold atom clouds, before closing with a section on the newly implemented Bragg diffraction set-up and the initial results from this.

3.1 BEC apparatus

The experimental apparatus can be divided into two main components physically separated on two optical tables named the *laser table* and the *vacuum table*. The vacuum system is illustrated in Fig. 3.1, and is divided into two main chambers - the magneto-optical trap (MOT) glass cell and the science chamber. In the following, selected parts of the experiment is described in more detail, but to get an idea where everything fits in, a general experimental sequence is first described.

An experimental run starts in the MOT chamber, where a cloud of ^{87}Rb atoms are optically trapped and cooled from a background gas of rubidium. The background gas is maintained by running rubidium dispensers. When the MOT contains $\sim 10^9$ atoms the MOT is extinguished, and the atoms are optically pumped to the magnetically trappable $|F = 2, m_F = 2\rangle$ hyperfine state¹, and caught in a magnetic quadrupole trap. The relatively high background pressure necessitates the two-chamber design, and the atoms are transported to the science chamber which is kept at lower pressure. This is achieved with two sets of quadrupole coils mounted on mechanical translation stages. The first set named the MOT coils transports the atoms from the MOT chamber through a differential pumping stage to the cross seen in Fig. 3.1. Here the atoms are transferred to the second set of coils named the Transport coils that take the atoms to the science chamber.

When arriving at the science chamber, the cloud is transferred to a quadrupole Ioffe-Pritchard configuration (QUIC) trap, where the cloud is

¹Throughout the thesis, I will refer to hyperfine ground states with $|F, m_f\rangle$ and the D₂-line excited states with $|F', m_{f'}\rangle$.

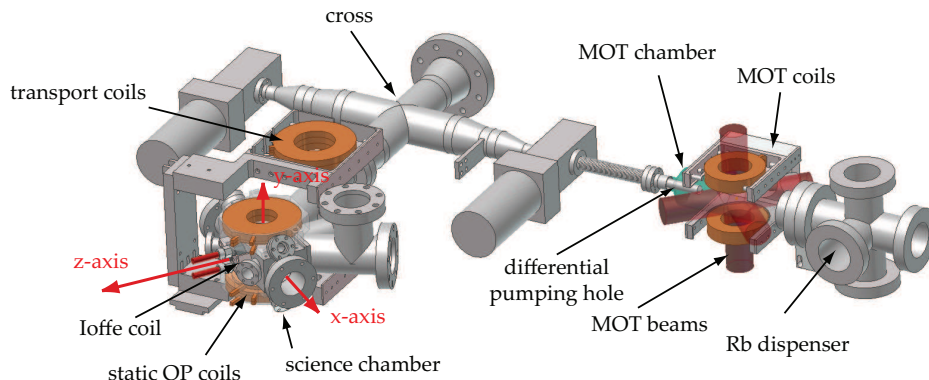


Figure 3.1: Overview of the vacuum system. Reproduced from [83]

further cooled by forced evaporative radio-frequency (RF) cooling. The entire duration of the sequence is roughly 1 min 20 s, yielding clouds with few hundred thousand atoms at temperatures on the order of 100 nK.

The unusual design where the atoms are transported around a cross is due to the initial design ideas for the experiment. The experiment were designed to be a dual species experiment with lithium as the second species. A second MOT chamber were planned on the other side of the cross, and the two species were to be prepared in separate MOTs before being combined at the cross. This idea was abandoned later due to the difficulty of combining two magnetic traps without losing atoms, and other experimental directions with a pure ^{87}Rb system have since been pursued.

3.1.1 Laser cooling and magneto-optical trapping

A MOT consists of an arrangement of laser beams and a magnetic field, that creates a spatially and velocity dependant force on the atoms. Our MOT consists of 3 orthogonal pairs of counter-propagating laser beams

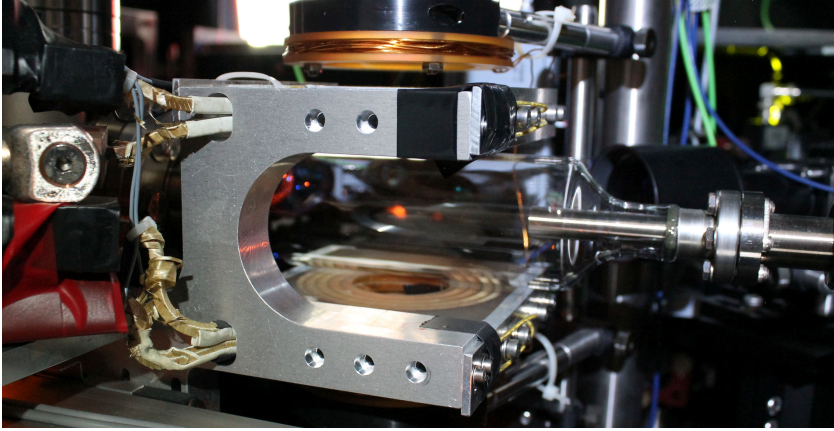


Figure 3.2: Image of the MOT glass cell taken with long exposure and a short flash while the MOT beams were on. The red spot in the center of the image is a cloud of trapped ^{87}Rb atoms. In the front the coil holders for the magnetic coils are seen.

that provide both cooling and trapping in all directions.

The cooling beams are red detuned relative to the $|F = 2\rangle$ to $|F' = 3\rangle$ transition of the D_2 line. When an atom moves towards a laser beam, the Doppler shift makes the atom resonant with the light, pushing the atoms in the opposite direction, thereby slowing its movement and cooling it down. If the atoms are off-centre from the magnetic field, the Zeeman shift will perturb the energy levels and move them into resonance. The increased scattering off-centre causes the atoms to be pushed toward the centre of the trap. Thus, the MOT provides both cooling and confinement of the atoms [85].

We typically load on the order of 1×10^9 atoms before they are optically pumped to the $|F = 2, m_f = 2\rangle$ state and transferred to the magnetic trap. Figure 3.2 shows a picture of a particular big MOT, where the spontaneous emission of red light is seen in the centre of the MOT glass cell.

3.1.2 Magnetic trapping

For the majority of the preparation sequence the atoms are trapped in magnetic traps. The Zeeman effect perturbs the energy levels of the atoms, leading to a potential energy of an atom in a magnetic field of

$$U(\mathbf{r}) = \mu_B g_F m_f |\mathbf{B}(\mathbf{r})|, \quad (3.1)$$

where μ_B is the Bohr magneton, g_F is the Landé g -factor and m_f is the hyperfine magnetic substate. It is thus possible to trap atoms in an inhomogeneous magnetic field near the field strength minimum for certain hyperfine states. For sufficiently slowly varying fields, the atoms spin orientation follow the field orientation adiabatically and they remain in the same spin state and stay trapped.

The experiment has three primary sets of magnetic coils for trapping of atoms, namely the MOT coils, the transport coils and the Ioffe-Pritchard QUIC trap. The MOT and transport coils are quadrupole coils in an anti-Helmholtz configuration. This yields a linear field with strong confinement but has a zero field crossing at the trap centre, where atoms can undergo Majorana spin flips making a non-adiabatic transition to an untrapped spin state and be lost from the trap [85]. This in particular becomes a problem as the cloud is cooled down, at which point the atoms spend more time at the trap centre.

To avoid this, the cloud is transferred to the harmonic QUIC trap. The QUIC trap is just one out of several trap configuration that realise a Ioffe-Pritchard trapping potential [86]. It consists of a pair of quadrupole coils with an extra coil in between that we denote the Ioffe coil. This configuration accomplishes two things. First, it has a non-zero magnetic field at the field minimum, which eliminates the problem of losses due to spin flips. Secondly, the potential is harmonic near the trap minimum. Figure 3.3 illustrates both coil geometries and the resulting potentials.

The trapping potential of the QUIC trap is asymmetric. At standard current settings, our trapping frequencies are around $\omega_\rho = 2\pi \times 300$ Hz in

the radial directions and $\omega_z = 2\pi \times 17\text{Hz}$ in the axial direction, which is along the symmetry axis of the Ioffe coil. If required, we can reduce ω_ρ to create a more symmetric trap. Either, we increase the relative strength of the Ioffe coil by bypassing some of the current through the quadropole (QP) coils, which is possible due to a MOSFET in parallel with the QP coils. Alternatively, we can increase the bias field in the axial direction. Both methods leave ω_z almost unchanged. As this reduces the overall confinement of the atoms, we refer to it as trap decompression.

The science trap was originally fitted with a MOSFET that could be used to bypass the Ioffe-coil. This meant that the field produced by the science coils could be transformed from a QP field to a harmonic field. To improve the stability of the trap, this was disconnected, and the current now runs in series through all 3 coils. This also means that we no longer have the option of starting the RF-evaporative cooling in a QP trap. A final MOSFET is used to extinguish the science trap. This allows us to turn off the trap in approximately 400 μs .

In addition to the main coils, the science trap is fitted with 4 pairs of shim coils² in Helmholtz configurations. They produce homogeneous fields which are used to null background fields or apply a bias field when required. Previously we had an extra option for creating large homogeneous fields in the vertical direction. The transport coils were fitted with a polarity switch, which inverted the current direction in one of the coils, changing the coil configuration to a Helmholtz configuration. The polarity switch was however removed in the fall of 2014 to increase the stability of the trap.

All coils share a similar design with a low winding number of ~ 40 to keep the inductance low. Therefore, a high current is required to create the necessary magnetic fields for trapping. Typically we use a current of 300 A.

²The z-axis has 2 sets of shim coils, a fast coil with a low winding number and a slower with larger winding number that produces stronger fields.

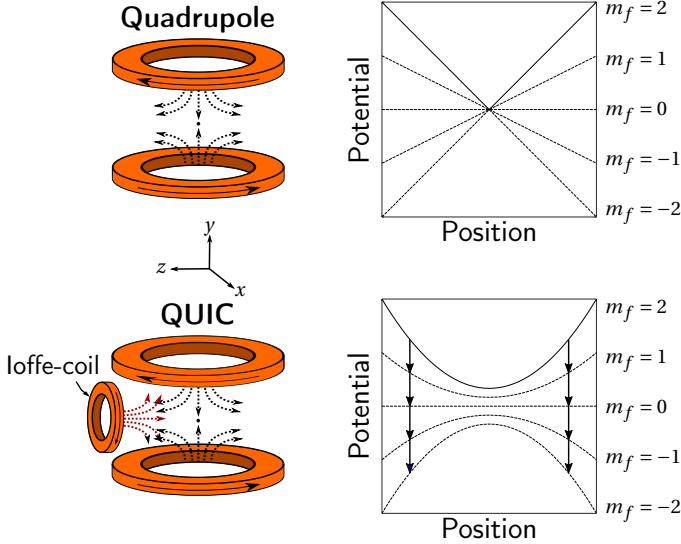


Figure 3.3: Illustration of coil configurations for the quadrupole and QUIC traps and the resulting potentials for ^{87}Rb in the hyperfine states $|F = 2, m_f = -2 - 2\rangle$. The arrows indicate RF transitions during evaporative cooling. Adapted from [87].

3.1.3 Forced RF evaporative cooling

The cloud temperature after laser cooling is still too high for Bose-Einstein condensation. To reduce the temperature we employ forced RF evaporative cooling. The RF-radiation couples the different m_f states in the hyperfine manifold $|F = 2\rangle$ when the frequency matches the Zeeman shift of the atoms. As the Zeeman shift is dependant on the position through Eq. (3.1), we can address a certain class of atoms by tuning the frequency, illustrated with arrows in Fig. 3.3.

The most energetic atoms venture farthest from the trap centre, where they experience a stronger magnetic field and correspondingly larger Zeeman

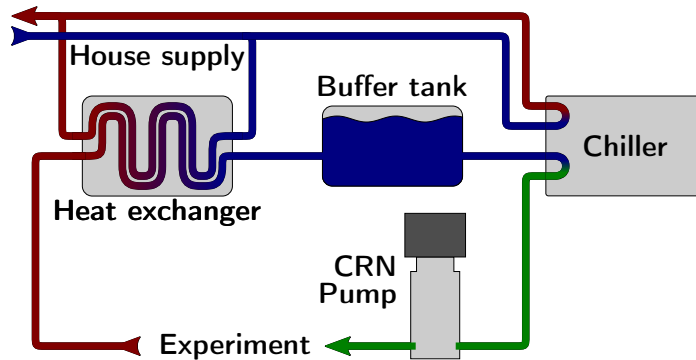


Figure 3.4: Schematic illustration of the cooling water system. Red tubes indicate hot water, blue indicates cold water and green tubes indicate water stabilised by the chiller.

man shift. Therefore, by slowly sweeping the RF from a high frequency to a lower frequency at a rate, where collisions between atoms redistribute the energy and preserve thermal quasi-equilibrium, we remove predominantly the hottest atoms. This allows us to cool clouds to ~ 100 nK with 10^5 to 10^6 atoms in approximately 45 s.

We typically refer to the frequency of the RF radiation as the RF knife ν_{knife} , and the lowest frequency that empties the trap as the trap bottom ν_{trap} . The same radiation is used to spill atoms in the feedback scheme presented in Chapter 5.

3.1.4 Cooling water system

The high current causes considerable heating of the coils, which therefore requires active cooling. The resistance in QUIC circuit is 14Ω , which

means we must remove 4.2 kW of heat. This is achieved by pumping cooling water through the hollow wires that make up the coils. The coils are wound into an hourglass-shaped spring, that when compressed forms a tight coil. To avoid deformation the coils are cast in epoxy. The MOT-coil and holder is visible in Fig. 3.2.

The cooling system is based on an internal closed circuit, where the water runs through all coils, in parallel with an external circuit in the building. When we started on the fluctuations work presented in Chapter 6, a rebuild of the cooling water system was required. The original system was based on heat exchanger, that delivered the heat from the internal circuit to the house supply, and a CRN pump to increase the pressure. The flow of external cooling water through the heat exchanger was regulated by a slow gas valve. The house cooling water supply can vary in temperature with several degrees on an hourly time scale, which lead to temperature variations of the magnetic coils. This was observed as a changing trap bottom ν_{trap} , that caused the trap depth $\nu_{\text{knife}} - \nu_{\text{trap}}$ to vary, inducing technical fluctuations in the final atom number and temperature of the prepared samples.

To remedy this, the new system is based on an active chiller unit³. The set-up is sketched in Fig. 3.4. The heat exchanger is still used to remove the bulk heat from the experiment, and the pre-cooled water is buffered in a 50 l buffer tank, corresponding to 2 min flow through the system. The water is further cooled by the chiller, which maintains a stability of 0.2 °C. There is a small ripple left, which has so far been unavoidable due to the big difference in load on the system when the trap is on and off. As the cooling is not completely isolated from the external house supply, during periods of large temperature variations of the external supply, this will still influence the experiment. The flow is increased from 16 l min⁻¹ to 23 l min⁻¹ using the CRN pump.

It is not feasible to completely avoid that the coils heat up during

³H.I.B RFCS 9HE 2 kW

operation, but the peak-to-peak variations are kept at 2 °C with a 0.1 °C variation of the peak level just before trap turn off, where it is most critical to keep a stable trap bottom.

3.2 Laser system

The heart of any quantum gas experiment is the laser system, which is used at all stages of the experiment for cooling, trapping, state preparation and detection of atoms. A large part of the laser system has been rebuilt. The original set-up was based on three 780 nm lasers named *Master*, *Cooler* and *Repumper* lasers. The Master laser was used for optical pumping and absorption imaging, as well as serving as a reference for the offset lock for the Cooling laser. The Cooling laser was amplified with a tapered amplifier (TA) for the MOT cooling light. The repump laser is the only remaining laser, and is used during the MOT stage to pump atoms lost from the cooling cycle by off-resonant excitation to the $|F' = 2\rangle$ state, from which they can decay to the $|F = 1\rangle$ state. The repump laser pumps atoms from $|F = 1\rangle$ to $|F' = 2\rangle$, where they predominantly decay to $|F = 2\rangle$ and are again back on the cooling transition. In combination, the cooling and the repumping light creates a closed cooling cycle.

In addition, the set-up consists of two additional 914 nm lasers for the optical lattice set-up [81]. Later, an extra 780 nm laser was added for off-resonant Faraday imaging [84]. All lasers were homebuilt Littrow configuration external cavity diode lasers.

In the fall of 2016 we installed a new 780 nm Toptica DL Pro laser. By shifting the frequency with acousto optic modulators (AOMs) this has replaced both the Master, Cooler and Faraday laser, reducing the number of operated lasers to two when the lattice setup is not used. This greatly increased the stability of the operation of the experiment, which in particular was crucial during the acquisition of the large datasets required for the investigation of fluctuations of a BEC presented in Chapter 6.

3.2. Laser system

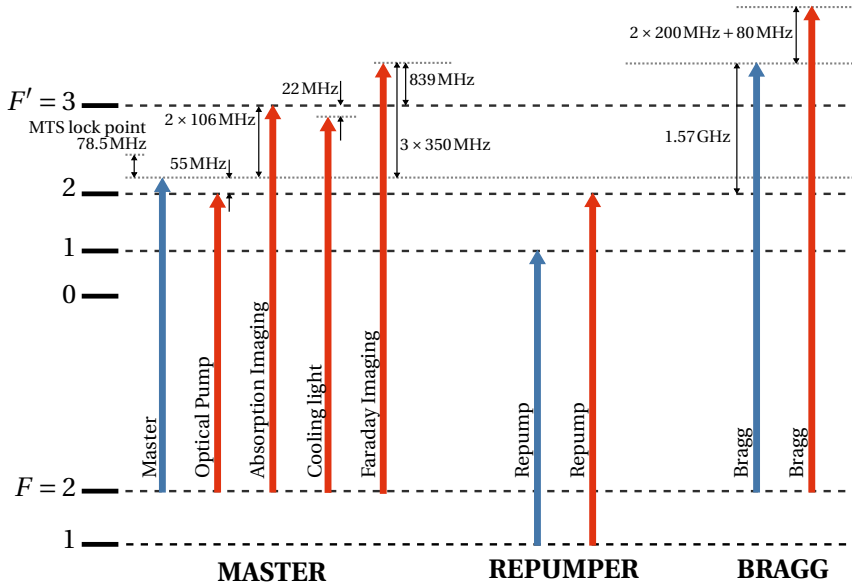


Figure 3.5: Schematic illustration of the laser frequencies of the three lasers used in the experiments in this thesis and the level structure of ^{87}Rb . Blue arrows indicate lock points of the lasers, and the red arrows show the frequencies shifted by AOMs.

Using the Master laser to generate light for Faraday imaging freed up the old Faraday laser set-up. Recently, we have reused this to implement a Bragg diffraction set-up, which is treated in Section 3.4.

In total, three lasers are currently in use for the experiments presented in this thesis. An overview of all the required frequencies are shown in Fig. 3.5 for the three lasers.

3. PRODUCTION AND DETECTION OF ULTRACOLD GASES

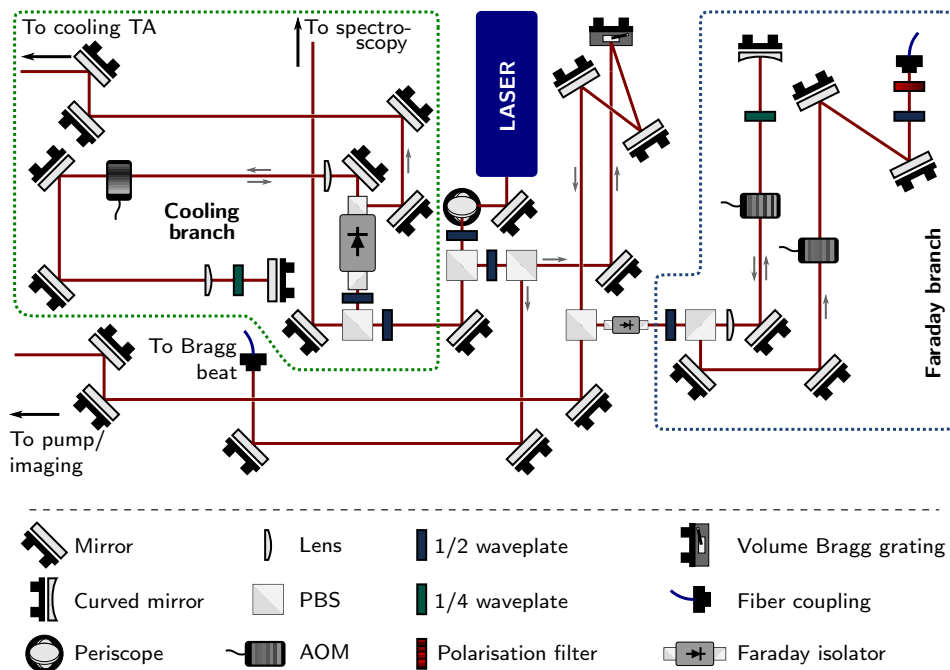


Figure 3.6: Schematic illustration of the new optical layout around the master laser. The Faraday and Cooling branches are highlighted with dashed borders.

Master laser

The new Master laser now delivers both optical pumping, imaging and Faraday-light, as well as seeds the cooling TA. Fig. 3.6 shows the current Master laser optical layout. The laser is locked using a Toptica Digilock i combination with a Frequency Modulation Transfer Spectroscopy set-up [88, 89]. The modulation is achieved with an AOM in double pass configuration, which is modulated at 111.61 kHz around a centre fre-

quency of 78.5 MHz. Since only the pump is shifted by 2×78.5 MHz, the laser is locked 78.5 MHz below the chosen lock point. By locking to the $|F = 2\rangle$ to $|F' = 2/3\rangle$ crossover resonance, the laser frequency is identical to the old Master laser, which was locked directly to the $|F = 2\rangle$ to $|F' = 1/3\rangle$ crossover resonance. This meant that the AOM set-up for optical pumping and imaging could be preserved without alterations.

The light is separated into two main branches, one for seeding the cooling TA, and one for imaging and optical pumping. The seed light is shifted up by 190 MHz with a double pass AOM. After amplification in the TA, the cooling light is combined with repump light, before being separated into three 50/50 fiber splitters, that corresponds to the three pairs of beams in the MOT.

The other branch is first cleaned by a volume Bragg grating (VBG). The grating has full width at half max (FWHM) bandwidth of 0.12 nm and removes the broad background of spontaneous emission from the diode laser. This is particular important for absorption imaging, as discussed in Section 3.3. The light is split into the Faraday imaging branch and the pump/imaging branch. The latter has not undergone significant changes from the original set-up. The optical pump is used after the MOT stage of an experimental sequence to prepare atoms in the $|F = 2, m_f = 2\rangle$ state that is magnetically trappable.

Repump laser

The repump laser is the only original laser still in use during the MOT stage. It is locked with frequency modulated saturated absorption spectroscopy by modulating the laser current. It is locked to the $|F = 1\rangle$ to $|F' = 1\rangle$ transition, and shifted into resonance with the $|F = 1\rangle$ to $|F' = 2\rangle$ transition. The repump light is mixed with the cooling light for the MOT and the optical pump. If we wish to image atoms in $|F = 1\rangle$ a small amount of repump light can be added to the imaging light.

Faraday laser setup

Since the new Master laser deliver much more power, we now derive the Faraday light from the master laser. Faraday imaging is treated in detail in Chapter 4, but the laser set-up is described here.

The light for Faraday imaging is extracted after being filtered by the VBG. To achieve the required detuning, two AOMs are used, both with a center frequency of 350 MHz. The first AOM has a wider bandwidth of 150 MHz and is arranged in a double pass configuration. The second has a bandwidth of 50 MHz and is in a single-pass configuration. This gives us a total detuning of 839 MHz blue-detuned with a tuning range of more than 200 MHz. Since there is sufficient light, the second AOM configuration can be changed to double pass if we require an additional 350 MHz shift.

3.3 Imaging systems

The experiment currently has two primary imaging systems, the absorption imaging system on the x -axis, and the Faraday imaging system on the z -axis⁴. If required, the cameras can be moved to the y -axis or one of the off-axis auxiliary axes for absorption imaging.

3.3.1 Absorption imaging

Absorption imaging is an ubiquitous method in experiments with ultracold gasses, and is our primary detection tool. The absorption imaging is used on the x -axis of the experiment, where both the radial and axial extent of the cloud can be observed. The cloud is imaged at an intermediate imaging plane by a pair of achromatic lenses. The intermediate imaging plane is then imaged onto a charge coupled device (CCD) by a second

⁴The coordinate-system is illustrated in Fig. 3.1

pair of achromatic doublet lenses. The camera is an Andor iXon Ultra 897, which is cooled to -40°C , at which point we observe no thermally induced counts. The imaging light is circular polarised, as this ideally creates a closed imaging transition from $|F = 2, m_f = 2\rangle$ to $|F' = 3, m_f = 3\rangle$, where the only dipole allowed transition is back to $|F = 2, m_f = 2\rangle$. To use circular polarisation for imaging, it is necessary to apply a bias magnetic field in the x -direction, which is achieved with the shim coils during TOF.

Previously, we observed stray light on the images, which was traced to reflections of the imaging beam on the camera, back to the imaging optics and on to the CCD. The CCD has a bright appearance around the active area, and the imaging beam is slightly larger than the chip size. Therefore, we installed an adjustable mask in the intermediate imaging plane, which consists of two pairs of adjustable razorblades. The mask blocks all light not falling onto the chip. With this in place, the problematic stray light is gone. The formed pinhole is much larger than the image of the cloud, which is important in order to avoid distortion of the formed image.

Extracting column density data from absorption images

Absorption imaging measures the cloud density profile by determining the number of photons scattered by the atoms from the shadow cast by the cloud. The scattering rate of a two-level atom can be derived from the optical Bloch equations [85]. Assuming that the atom has undergone many scattering events and all coherences has decayed, the steady state scattering rate of an atom illuminated by light of intensity I is

$$R_{\text{sc}} = \frac{\Gamma}{2} \frac{I/I_{\text{sat}}}{1 + (2\Delta/\Gamma)^2 + I/I_{\text{sat}}}, \quad (3.2)$$

where Γ is the natural line-width of the atom and I_{sat} is the saturation intensity. This lead to a reduction of the light intensity as the imaging beam propagates through the sample. The attenuation of the intensity of

light with angular frequency ω depends on the atomic density through

$$\frac{dI}{dz} = -\hbar\omega R_{\text{sc}} n(z) = -\frac{n(z)\sigma_0}{1 + (2\Delta/\Gamma)^2 + I/I_{\text{sat}}} I, \quad (3.3)$$

where the resonant scattering cross section $\sigma_0 = \hbar\omega\Gamma/2I_{\text{sat}}$ has been introduced.

Due to the Lorentzian line shape of the laser, any frequency noise affects the precision of the imaging more when $\Delta \neq 0$. Additionally, the dispersion is non-zero for $\Delta \neq 0$, which causes the atoms to refract the imaging light. We therefore always image on resonance where $\Delta = 0$.

The two-level model is inadequate for real atoms. To take into account effects such as the multi-level atomic structure, polarisation imperfections and possibility of multiple scattering events, the saturation intensity is replaced with an effective saturation intensity $I_{\text{sat}}^{\text{eff}} = \alpha I_{\text{sat}}$ [90]. With this, Eq. (3.3) becomes

$$\frac{dI}{dz} = -\hbar\omega R_{\text{sc}} n(z) = -n(z) \frac{\sigma_0}{\alpha} \frac{1}{1 + I/I_{\text{sat}}^{\text{eff}}} I. \quad (3.4)$$

To determine the atomic density, Eq. (3.4) is integrated along z to yield the optical depth

$$\text{OD} = \alpha \ln\left(\frac{I_0}{I}\right) + \frac{I_0 - I}{I_{\text{sat}}} = \sigma_0 \int dz n(z) = \sigma_0 \tilde{n}, \quad (3.5)$$

where I_0 and I are the incident and final intensities and \tilde{n} is the column density. The α -coefficient thus corresponds to a scaling between the logarithmic and linear part of the optical density. Since it must be independent of the light intensity, we can calibrate α by imaging clouds of constant density at different light intensities [90]. The feedback-stabilised preparation covered in Chapter 5 greatly improves our ability to perform such calibrations, as we can insure constant atom number between experimental runs [31].

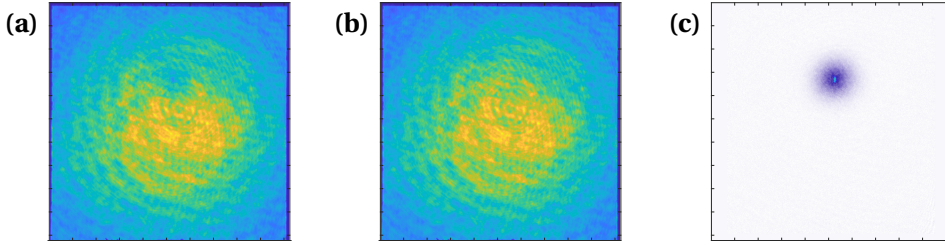


Figure 3.7: Two raw images are obtained to calculate the optical depth. **(a)** A raw shadow image with the cloud barely visible. **(b)** To correct for the spatial structure of the imaging beam, a second image without atoms is acquired. Both images are corrected for the bias level. **(c)** The cloud is clearly visible in the evaluated optical depth image.

To extract the optical depth from a shadow image, we need to know both the incident and final intensities of the imaging beam. Figure 3.7(a) shows an example of a shadow image, where the cloud profile is hidden by the structure of the imaging beam. A beam image shown in Fig. 3.7(b) without atoms is obtained to determine the spatially varying intensity, and Eq. (3.5) is used to evaluate the optical density shown in Fig. 3.7(c). Both the shadow and the beam images are corrected for the bias level of the camera and potential stray light not originating from the imaging beam. This is achieved by subtracting two images recorded without the imaging pulses shortly after the atom and beam images.

Saturation of the optical depth

The largest observable optical depth in absorption imaging will be limited by any off-resonant light in the imaging beam, that is not absorbable by the cloud. To model this, one can assume that a small amount of off-resonant light $I_{\text{off}} = \gamma I_0$ is added to I and I_0 . If the cloud is very dense, all light will be absorbed, and $I = 0$. The maximally observable optical depth

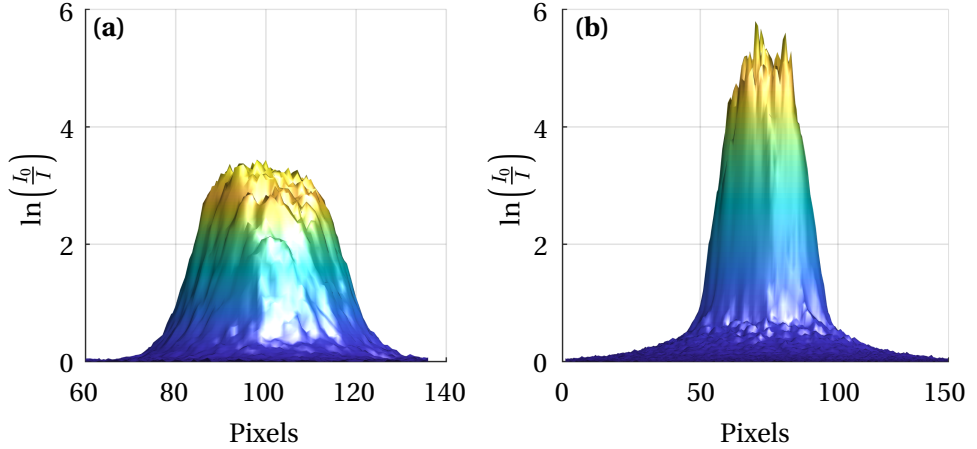


Figure 3.8: Illustration of the effect of the VBG showing the logarithm term of Eq. (3.4) (without the α prefactor) of saturated images. **(a)** A thermal cloud at short TOF imaged before the installation of the new laser and the VBG. **(b)** A BEC imaged with the new laser and the VBG.

is then

$$OD_{\max} = \alpha \ln \left(\frac{I_0 + I_{\text{off}}}{I + I_{\text{off}}} \right) + \frac{(I_0 + I_{\text{off}}) - (I + I_{\text{off}})}{I_{\text{sat}}} = \alpha \ln \left(\frac{1 + \gamma}{\gamma} \right) + \frac{I_0}{I_{\text{sat}}}. \quad (3.6)$$

There are now two options for reducing the saturation effects. Either the light intensity I_0 is increased, or γ is minimised. To obtain the best precision, a reasonable fraction of the intensity should be absorbed by the cloud, which effectively limits I_0 to $\sim 1 I_{\text{sat}}$ to $3 I_{\text{sat}}$.

To reduce γ we have installed the VBG seen in the diagram in Fig. 3.6. As previously mentioned, it acts as a narrow band filter with a FWHM bandwidth of 0.12 nm. The effect of the VBG is seen in Fig. 3.8, where the logarithm term of Eq. (3.4) is shown for two clouds imaged with and without the VBG installed, respectively. The flat tops of the distributions is caused by saturation of the optical depth, but the saturation level

increases from 3.07(14) without the VBG to 5.0(3) with the VBG installed. Using Eq. (3.6) this corresponds to a reduction of $\gamma = 4.9 \times 10^{-2}$ to $\gamma = 6.8 \times 10^{-3}$.

Saturation of the optical depth will not only limit the maximal observable densities, but will also lead to a systematic underestimation of the densities as the saturation level is approached. We therefore always strive to limit the optical depth to $1/2 \times OD_{\text{max}}$. The optical depth can be reduced by increasing the expansion time before imaging the clouds.

Fringe suppression through fast imaging

Vibration of optical components along the beam path leads to variation of the imaging beam between the shadow and the background image. This will be visible in the evaluated optical depth images as fringes, which severely limits our ability to accurately extract cloud properties. Apart from mechanically reducing the vibrations of the experimental set-up, we can reduce the influence of vibrations by acquiring the images much faster than any significant vibrations frequencies.

The frame rate will be limited by the time it takes the cloud to leave the signal area. Even for cold thermal clouds at 25 ms TOF, the cloud will still linger in the frame for several milliseconds, which corresponds to the time scale of acoustic frequencies.

To speed up the frame rate we need to remove the atoms faster after the shadow image has been acquired. We have previously used resonant light to blow the atoms out of the frame, but due to the saturation of the optical transition which caps the acceleration due to a push beam, this method was limited to an image separation of $800 \mu\text{s}$ [91].

Instead we now pulse on the pump-light after acquiring the first image. The pump excites the atoms to the $|F' = 2\rangle$ state, from which they with reasonable probability decays to $|F = 1\rangle$, where the imaging light is detuned by 6.8 GHz from the atomic transition. We denote it the *depump* pulse. To make sure that it is sufficient to remove the atoms, we measured

3. PRODUCTION AND DETECTION OF ULTRACOLD GASES

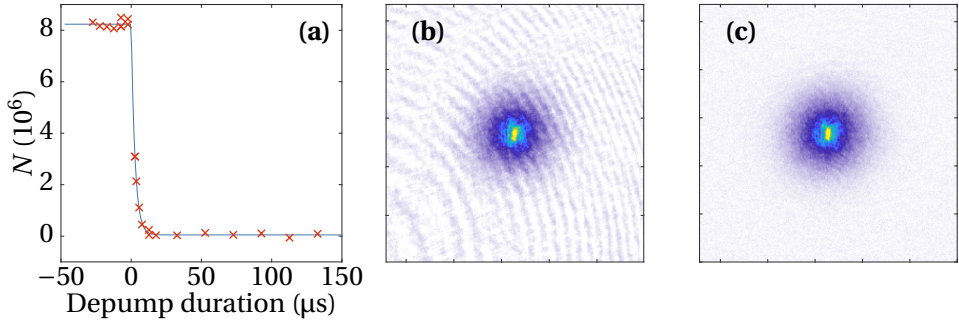


Figure 3.9: Illustration of the efficiency of the depump pulse. **(a)** The number of atoms in $|F = 2\rangle$ as a function of the illumination time of the depump pulse. The measured decay time is $2.7 \mu\text{s}$. **(b)** We record beam images with 6 s of separation from the shadow image. Evaluation of the cloud density using this image shows clear fringes. **(c)** The fringes are suppressed by keeping the delay between the shadow and beam image as short as possible. Here the separation is $340 \mu\text{s}$.

the destructivity of the pulse. Figure 3.9(a) shows the atom number as a function of the depump pulse duration. The total pulse power is $97 \mu\text{W}$, and the decay time of the atoms once illuminated is $2.7 \mu\text{s}$. Using the depump, the frame separation is reduced to $340 \mu\text{s}$, limited by the time required by the camera to shift a frame into the storage area of the chip when operated in frame transfer mode.

Figure 3.9(b - c) illustrates the benefit of the fast imaging. The first image shows the cloud density evaluated with a beam image delayed by several seconds, whereas the second is evaluated using the beam image obtained by the use of a depump pulse.

Fringing of the images due to vibration can also be tackled in the post-processing of the images. As an alternative to using a single beam image, a large number of beam images is then recorded to construct a

basis set. From the basis set an artificial beam image is created as the linear combination, that minimises the difference between the shadow image and the artificial beam image in a region that excludes the atomic signal [92]. In addition to reducing fringing of the images, since the beam image now is an average over many images, the total number of photons collected is much larger. This leads to a reduction of the photon shot noise in the beam image. We have tested this method on images without atoms where the method works very well. However, when analysing the atom number fluctuations presented in Chapter 6, we found no improvements from this method after the fast imaging was implemented. This indicates, that the fringing is already sufficiently reduced and that our detection is not limited by the photon shot noise in the beam image.

3.3.2 Faraday imaging

Faraday imaging is a non-destructive dispersive imaging method, that enables non-destructive probing of ultracold gases. It is treated in greater detail in Chapter 4, and is a prerequisite for the feedback stabilised preparation of ultracold atom clouds presented in Chapter 5.

3.4 Bragg diffraction of ultracold clouds

The newest addition to the experimental apparatus is a small Bragg diffraction set-up. The set-up has been designed and assembled on a bread board by Søren Sørensen Snefrup as a part of his masters degree.

The set-up is used to scatter atoms using two counter-propagating off-resonant laser beams. The scattering can be seen as a N -photon process, where an atom absorbs N photons from the first laser beam and re-emits them into the second through stimulated emission. If the two laser beams have a frequency difference $\nu = \nu_2 - \nu_1$, the atoms will gain kinetic energy. This corresponds to a transition between two momentum

states within the same internal ground state. The transition must fulfil energy and momentum conservation, giving rise to the Bragg scattering condition

$$Nh\nu = \frac{(p_0 + 2N\hbar k)^2}{2m} - \frac{p_0^2}{2m} = \frac{2N\hbar k p_0}{m} + \frac{2N^2\hbar^2 k^2}{m}, \quad (3.7)$$

where k is wave number of the light m and p_0 is the mass and initial momentum of the atom. By tuning the frequency difference ν we can address a certain velocity class.

However, for a Bragg pulse of finite duration τ , the spectral width of the pulse will be Fourier limited by $\Delta\nu \approx 1/\tau$. This gives rise to two distinct ways to use the set-up. For long pulses, the spectral width of the diffraction pulse becomes narrower than the momentum distribution of the ultracold sample. This has been used to make direct spectroscopic measurements of the momentum distribution of ultracold gases and BECs [93]. For short pulses, the spectral width can be significantly broader than the momentum distribution of the samples. In this case the entire sample will be diffracted, which has been used in atom interferometers for creating the beam splitters and mirrors, transferring a large number of momentum quanta $\hbar k$ to the atoms [94, 95].

Due to the large difference in the widths of the momentum distribution of a thermal cloud and a BEC, Bragg diffraction has also been used to spatially filter the condensate from the thermal background. This is achieved by using a pulse duration τ such that the entire BEC is diffracted, but the spectral width of the Bragg pulse is still narrow relative to the thermal momentum distribution. This has been used to investigate the thermodynamics of BECs at finite temperature [21], as well as separate the condensate and the quantum depletion for BECs at zero temperature [96]. This application is the main motivation for us, as it complements direct measurements of the TOF density distributions when investigating the BEC statistics, which is the topic of Chapter 6.

3.4. Bragg diffraction of ultracold clouds

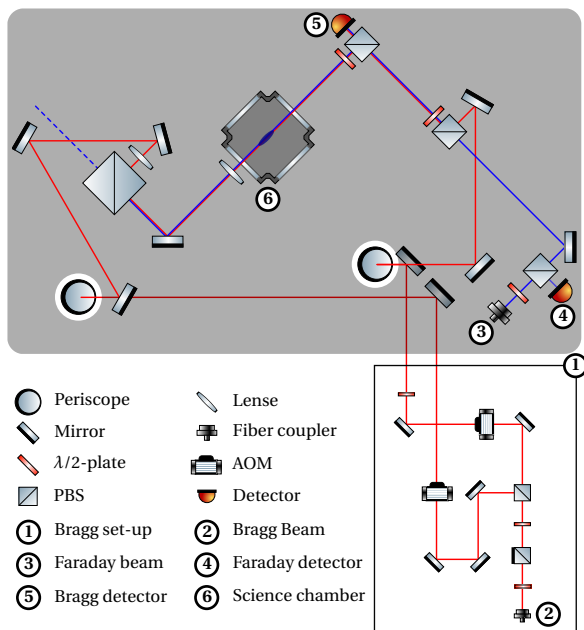


Figure 3.10: Schematic illustration of the implementation of the Bragg set-up on the laser table. The red line illustrates the beam path of the Bragg light and the blue line illustrates the Faraday imaging light. Reproduced from [87].

Our implementation of the Bragg diffraction set-up is sketched in Fig. 3.10. The old Faraday laser that was freed up by the new master laser is reused as the Bragg diffraction laser. It is offset locked to the Master laser with a detuning of 1.57 GHz and shifted by a further 400 MHz by an AOM in double pass configuration. The AOM doubles as the optical switch to generate the pulses. The light is transferred to the vacuum table via a single optical fiber to avoid a differential phase shift of the two Bragg beams.

Once at the vacuum table the light is split 50/50 and shifted by an

additional 80 MHz with two independent AOMs, achieving a total detuning of 1.84 GHz blue detuned from the $|F = 2\rangle$ to $|F' = 3\rangle$ transition. The relative detuning between the two beams are obtained by setting the desired frequency difference of the two phase-locked RF sources for the AOMs. The Bragg beams are overlapped with the cloud by overlapping one beam with the Faraday imaging beam and using the now spare port on the polarising beamsplitter (PBS) cube after the chamber.

The formalism developed for two-level atoms in an electromagnetic field can be applied to the Bragg scattering process by realising, that the system is analogous to a two-level system. The two-level system is realised by the two distinct momentum states that fulfil the Bragg condition Eq. (3.7). In this case, the ground state has momentum p_0 and the excited state has momentum $p_0 + N\hbar k$. This means that concepts such as Rabi oscillations, π -pulses etc. applies here as well. For a two level system starting out in ground state, the probability for finding the atom in the excited state is given by [97]

$$|c_2(t)|^2 = \frac{\Omega^2}{\Omega^2 + \Delta^2} \sin^2\left(\frac{\sqrt{\Omega^2 + \Delta^2} t}{2}\right). \quad (3.8)$$

Here Ω is the Rabi frequency and $\Delta = 2\pi \times (\nu - \nu_0)$ is the detuning from the resonance frequency ν_0 fulfilling the condition given by Eq. (3.7) for $p_0 = 0$.

Since the set-up is a very recent addition to the experimental apparatus, we have only made a few first experiments to characterise and test the capabilities. Figure 3.11(a) shows a measurement of the resonance frequency. The data is obtained by applying a short Bragg pulse of duration $\tau = 132\mu\text{s}$ to a BEC after 2 ms TOF, after which the two momentum states separate in time of flight. The cloud is imaged after 27.5 ms, where we count the atom numbers N_0 and N_1 of the two momentum states. By scanning the frequency difference ν the transferred fraction changes. In Fig. 3.11(a) the relative fraction of atoms in the excited momentum state is

3.4. Bragg diffraction of ultracold clouds

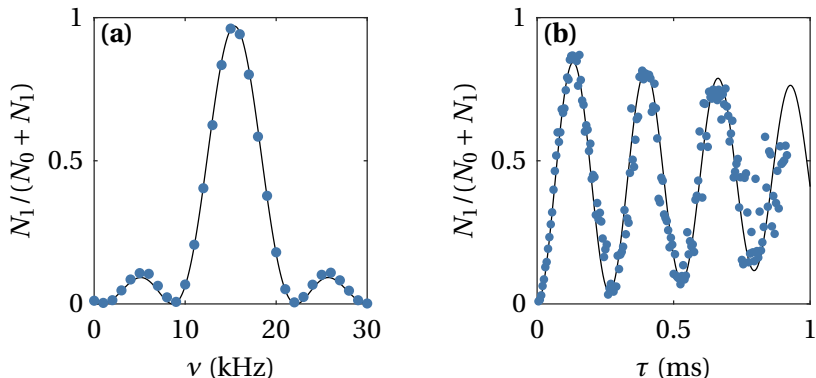


Figure 3.11: **(a)** Scan of the resonance frequency for Bragg scattering. Errorbars are smaller than the markers. **(b)** Rabi oscillations as the Bragg pulse duration is increased.

fitted with Eq. (3.8) with Ω and ν_0 as free parameters. $|c_2(t)|^2$ corresponds to N_1 . From the fit, we determine $\nu_0 = 15.42(2)$ kHz, which corresponds well to the prediction of Eq. (3.7) $\nu_0 = 15.09$ kHz. The discrepancy may be due to a small misalignment of the Bragg beams, or that the trap turn off induces a small lateral motion of the cloud. The Rabi frequency is found to be $\Omega = 2\pi \times 3.37(4)$ kHz.

Figure 3.11(b) shows Rabi oscillations when the Bragg pulse duration is varied at a constant frequency $\nu = 16.2$ kHz. The data is fitted with Eq. (3.8) modified to include a decay of the coherence with decay time τ_0 towards the steady state value $\Omega^2/2/(\Omega^2 + \Delta^2)$

$$N_1 = \left(|c_2(t)|^2 - \frac{\Omega^2/2}{\Omega^2 + \Delta^2} \right) e^{-\tau/\tau_0} + \frac{\Omega^2/2}{\Omega^2 + \Delta^2}. \quad (3.9)$$

The fit yields $\Omega = 2\pi \times 3.50(2)$ kHz, $\Delta = 2\pi \times 0.224(7)$ kHz and $\tau_0 = 3.0(2)$ ms. Curiously, this indicates a shift of the resonance frequency by ≈ 0.6 kHz, which we also observe in the Bragg spectroscopy measurements to be

discussed next, but as of yet we are not aware of the origin. The decay of the oscillations is partially explained by the fact, that for longer pulse durations, the spectral width of the Bragg pulse becomes comparable to the width of the momentum distribution. This will prevent full transfer, but does not explain why we do not return to no transfer for a full 2π -pulse. This can only be understood as decay of coherence. The beam path is quite long, and for a pulse duration of up to 1 ms the time scale is comparable to acoustic vibrations of optical components along the different beam paths. This can lead to different phase noise on the two counter-propagating beams, which will lead to the observed loss of coherence.

Bragg spectroscopy

By using long Bragg-pulses, we have measured the spectral distributions of a thermal clouds at a temperature $T = 80$ nK and a pure BEC. Since the spectral width of the BEC is significantly narrower, the pulse duration was $\tau = 5$ ms, while the pulse duration was $\tau = 250$ μ s. Both spectra are seen in Fig. 3.12. By scanning the detuning and determining the fraction of scattered atoms, the momentum distributions are mapped out. To make a qualitative comparison, the atom number of the thermal cloud were reduced below the critical number for condensations, and the temperature thus corresponds to a typical partially condensed cloud. Still, the thermal momentum distribution is much wider than that of the BEC.

The thermal data has been fitted with a Gaussian distribution, yielding a width of $\sigma_v = 8.4(4)$ kHz. The momentum spread of the Maxwell-Boltzman distribution is $\sigma_p = \sqrt{mk_B T}$, which by the use of Eq. (3.7) yields a width of $\sigma_v = 7.1$ kHz. Taking the Fourier width of the Bragg pulse $\sim 1/\tau = 4$ kHz into account, the expected width is $\sqrt{(7.1 \text{ kHz})^2 + (4 \text{ kHz})^2} = 8.1$ kHz, showing that the agreement is excellent.

As seen in Section 2.4, the TOF-expansion of a weakly interacting BEC retains the parabolic shape. Hence, the momentum distribution of

3.4. Bragg diffraction of ultracold clouds

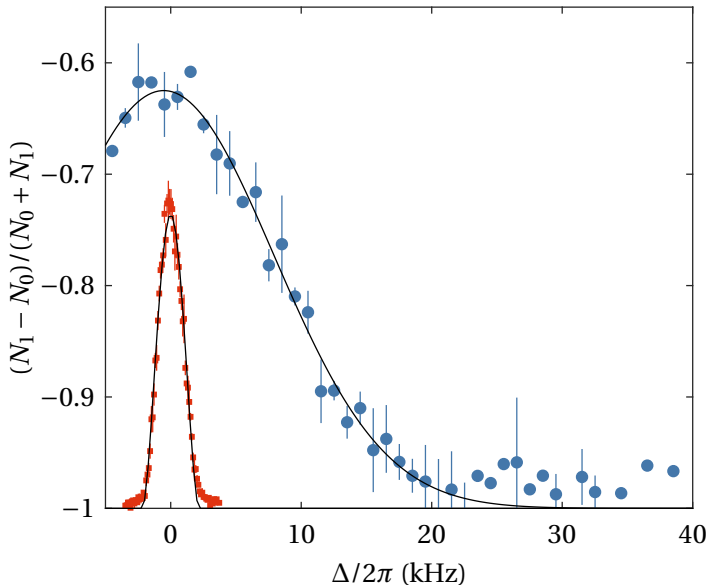


Figure 3.12: Bragg spectroscopy measurements of the momentum distribution of an almost pure BEC (■) and a thermal cloud (●). The data is fitted with a squared inverted parabola and a Gaussian distribution respectively.

BEC is also parabolic [93], and the BEC data is fitted with an inverted parabola integrated along the x - and y -directions similar to Eq. (A.2). The fit function is thus

$$f(\Delta/2\pi) = a \max\left(0, 1 - \frac{(\Delta/2\pi)^2}{\nu_{\text{HW}}}\right)^2 - 1. \quad (3.10)$$

The fit yields a half-width of the zero-crossing $\nu_{\text{HW}} = 2.19(2)$ kHz. The data shows small wings that cannot be fitted. These are most likely residual thermal atoms that are not visible in the TOF images, but revealed by the Bragg diffraction spectroscopy.

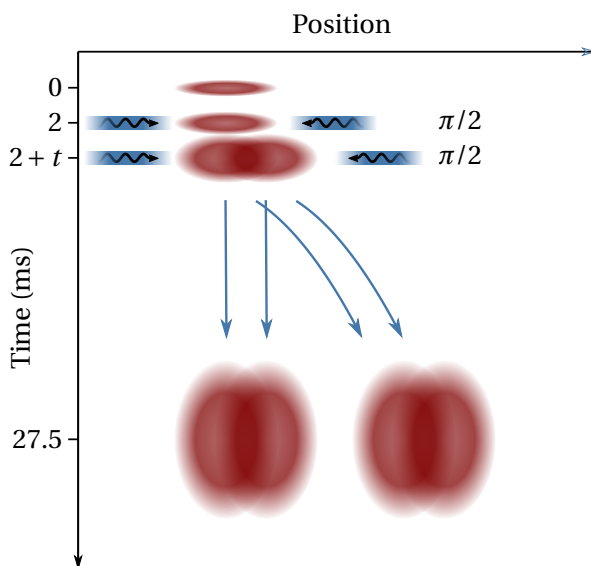


Figure 3.13: Schematic illustration of the open interferometer. Two pairs of BEC are made to overlap by splitting the BEC twice with two $\pi/2$ -pulses separated by a time delay t

Open interferometer

As a last example of the capabilities of the Bragg set-up, we have created a simple open interferometer. The interferometer sequence is illustrated in Fig. 3.13. A $\pi/2$ pulse is applied after 2 ms TOF, separating the cloud in two. After a variable delay t a second $\pi/2$ splits both clouds again, creating two pairs of clouds following parallel trajectories. The overlap can be adjusted by changing the time delay. Such an interferometer has been used to study the coherence of BECs [98].

Figure 3.14 shows a series of absorption images after the interferometer sequence, showing clear vertical equidistant interference stripes. The pattern can be intuitively understood by realising, that the parabolic

3.4. Bragg diffraction of ultracold clouds

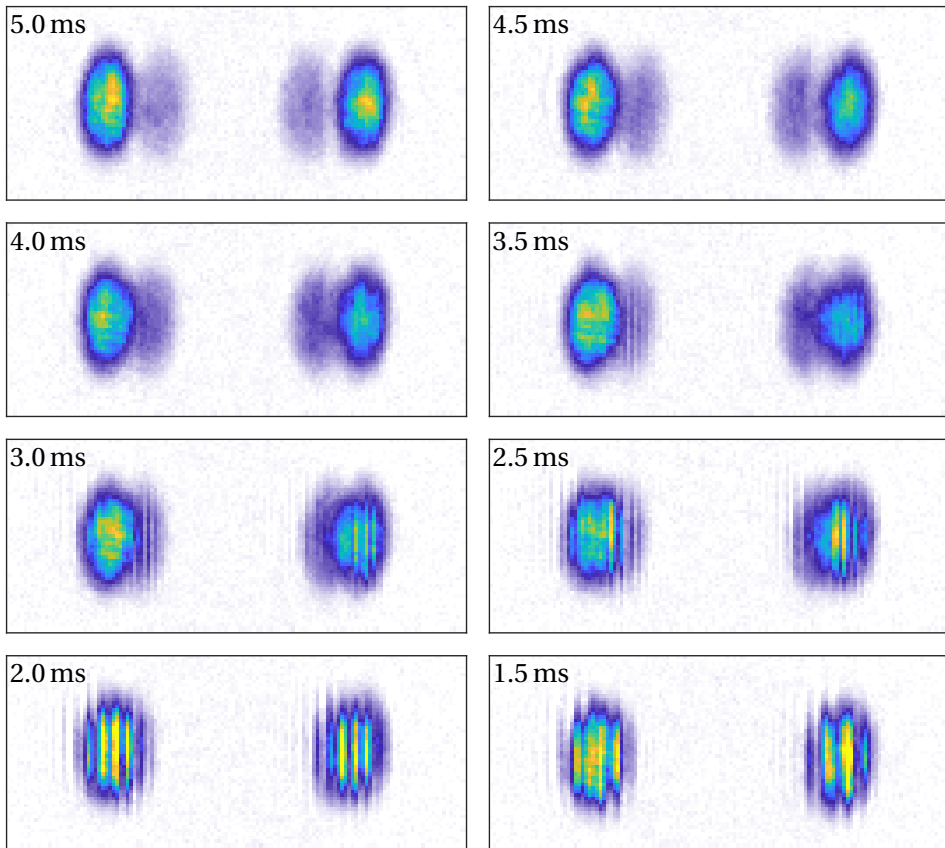


Figure 3.14: Experimental images of the open interferometer, showing interference fringes when the condensates overlap. The time delay t is indicated in each image.

3. PRODUCTION AND DETECTION OF ULTRACOLD GASES

density profile implies that the velocity field being the gradient of the density is linear. Therefore, the velocity difference is constant across the overlapping condensates and depends only on the spatial overlap given by the separation time delay t . Thus for larger t the the velocity difference is larger and the stripes change more rapidly across the BEC.

NON-DESTRUCTIVE FARADAY PROBING OF ULTRACOLD CLOUDS

In this chapter I present an overview of our implementation of Faraday imaging followed by a detailed characterisation and analysis of the obtainable precision in our Faraday measurements. The Faraday imaging has become an invaluable tool in our experiments, enabling non-destructive probing of ultracold clouds, which besides providing very precise measurements of relative atom numbers also greatly improves calibrations and diagnostics of the experiment. Most importantly this has enabled our actively stabilised preparation of ultracold clouds presented in Chapter 5.

The initial experimental implementation of Faraday imaging was done before I arrived in the group. The Ph.D. thesis of Miroslaw Gajdacz [84] contains details on the initial implementation and experiments with Faraday detection, as well as comparisons of the signal-to-noise

ratio (SNR) of different dispersive imaging techniques. During my studies the method has been used for the stabilisation experiments, which warranted a detailed experimental investigation of the performance of the imaging method.

Our implementation of Faraday imaging and the performance is presented in this chapter. It is adapted in mostly original form from Chapter 2 of my progress report [99], which has also formed the basis of our paper published in Journal of Physics B [32]. The body text and figures Section 4.3 has been restructured to incorporate material from [32], and Section 4.4 has been adapted to adopt notation from [32].

4.1 Faraday rotation

Non-destructive imaging of ultracold gases with spatial resolution has been demonstrated using various different techniques based on diffraction [27], partial transfer absorption imaging [28] and dispersive methods [23, 100]. The dispersive methods all rely on detecting the phase shift an imaging beam experiences after off-resonant interaction with an atomic sample. The interaction can be through the scalar part of the atomic polarisability, as in dark field scalar imaging and phase contrast imaging, or through the vector part as in dark field Faraday imaging [25, 31] and dual port Faraday imaging [29]. Provided that the shot noise of the detected light is the dominant source of noise, all four dispersive imaging methods yield a comparable SNR [31]. In our experiments we employ dark field Faraday imaging, which I will subsequently refer to simply as Faraday imaging.

Faraday imaging exploits circular birefringence in spin-polarised atomic samples. The light-matter interaction leads to a differential phase shift of the two circular components of the light leading to an overall rotation of the initial linear polarisation plane. The rotation angle is given

4.2. Experimental implementation of Faraday imaging

by

$$\theta(x, y) = c_F(\Delta_{\text{eff}}) \tilde{n}(x, y), \quad (4.1)$$

where $\tilde{n}(x, y)$ is the column density of the atomic cloud and the Faraday coefficient of ^{87}Rb is given as $c_F(\Delta_{\text{eff}}) = \frac{\hbar m_F \Gamma \lambda^2}{16\pi \Delta_{\text{eff}}}$ [31]. For ^{87}Rb atoms in the $|F = 2, m_F = 2\rangle$ state that are probed on the D2 line, the natural linewidth is $\Gamma = 2\pi \cdot 6.067$ MHz, and the wavelength of the imaging transition is $\lambda = 780.241$ nm. The effective detuning Δ_{eff} describes the detuning of the imaging beam weighted by the transition strength for the three possible optical transitions $F = 2 \rightarrow F' = 1, 2, 3$

$$\frac{1}{\Delta_{\text{eff}}} = \frac{1}{20} \left(\frac{28}{\Delta_{2,3}} - \frac{5}{\Delta_{2,2}} - \frac{3}{\Delta_{2,1}} \right). \quad (4.2)$$

4.2 Experimental implementation of Faraday imaging

Figure 4.1 shows the key elements of the Faraday imaging set-up. An off-resonant imaging beam initially linearly polarised along y propagates along the quantization axis defined by the bias magnetic field along the z -axis of the magnetic trap. The spatial distribution of the atomic cloud is mapped onto the polarisation of the imaging beam through the Faraday effect. A PBS cube reflects the non-rotated light, and the rotated light is imaged onto an Andor iXon DU-888 Electron Multiplying Charge Coupled Device (EMCCD) camera. The magnification of the imaging system is 4.85. The intensity of the imaging light can be monitored on a photodiode (PD) on the reflected port, and can be used to stabilise the imaging light intensity.

A typical absorption imaging set-up is easily adapted for Faraday imaging. The sole extra component required is the polariser.

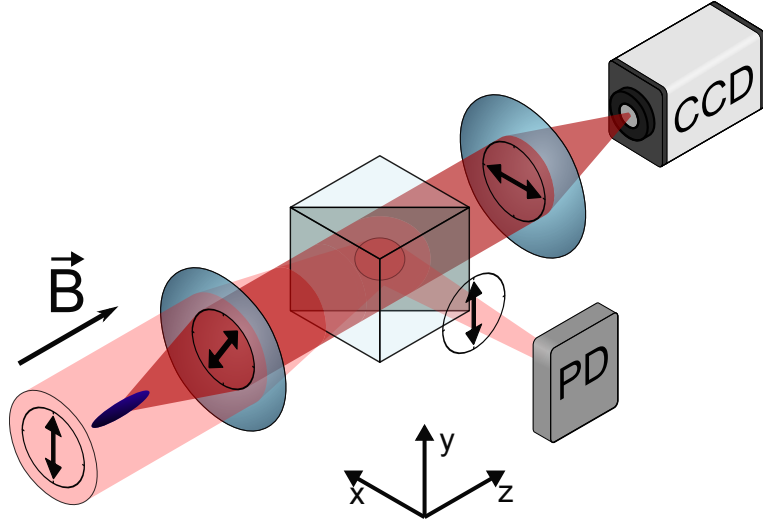


Figure 4.1: Sketch of the experimental setup. The polarisation state of the light is indicated by the double-headed arrows. The interaction with the atoms (blue, cigarshaped) causes the polarisation to change. Adapted from [99]

4.3 Characterisation of Faraday imaging

To characterise the imaging method, clouds containing on average 5×10^6 atoms at a temperature of $18 \mu\text{K}$ were prepared in the QUIC trap with axial and radial trapping frequencies $\omega_z = 2\pi \times 17.1 \text{ Hz}$ and $\omega_\rho = 2\pi \times 296 \text{ Hz}$, respectively. The axial bias was 330 mG. The general steps for preparation of ultracold clouds is outlined in Chapter 3. The results presented in this chapter were acquired before the replacement of the original Faraday laser setup. Details on the old laser setup can be found in [84]. The imaging light was detuned by 1200(1) MHz from the $|F = 2 \rightarrow |F' = 3\rangle$ transition. The intensity distribution of the imaging beam was Gaussian with a waist of 1.4 mm. The intensity of 0.5 mW cm^{-2} across the cloud

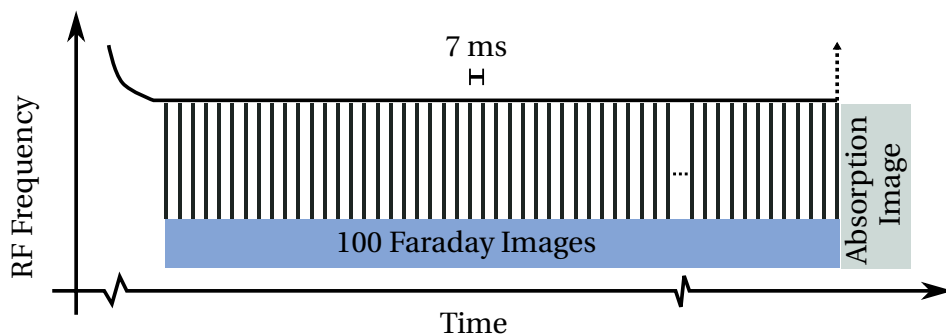


Figure 4.2: Outline of the experimental sequence after evaporative the evaporative cooling. Adapted from [99].

was approximately uniform.

The last part of the experimental sequence is depicted in Fig. 4.2. After initial evaporative cooling, the RF frequency is held constant. A series of 100 Faraday images is taken with 7 ms between the beginning of each imaging pulse. The pulse duration can be varied to investigate the precision as a function of the probe duration. After the 100 images are recorded, the magnetic trap is extinguished, and an absorption image in TOF is obtained. This allows us to calibrate the Faraday images to obtain accurate atom numbers. The data was acquired over several days.

4.3.1 Evaluation of Faraday images

A great advantage of Faraday imaging is the relative simplicity of evaluating the Faraday signal, as all required information is contained in the image, and the acquisition of reference images is not required as in the case of e.g. absorption images. Figure 4.3(a) shows an example of a raw Faraday image, with relevant regions of interest (ROIs) marked. The

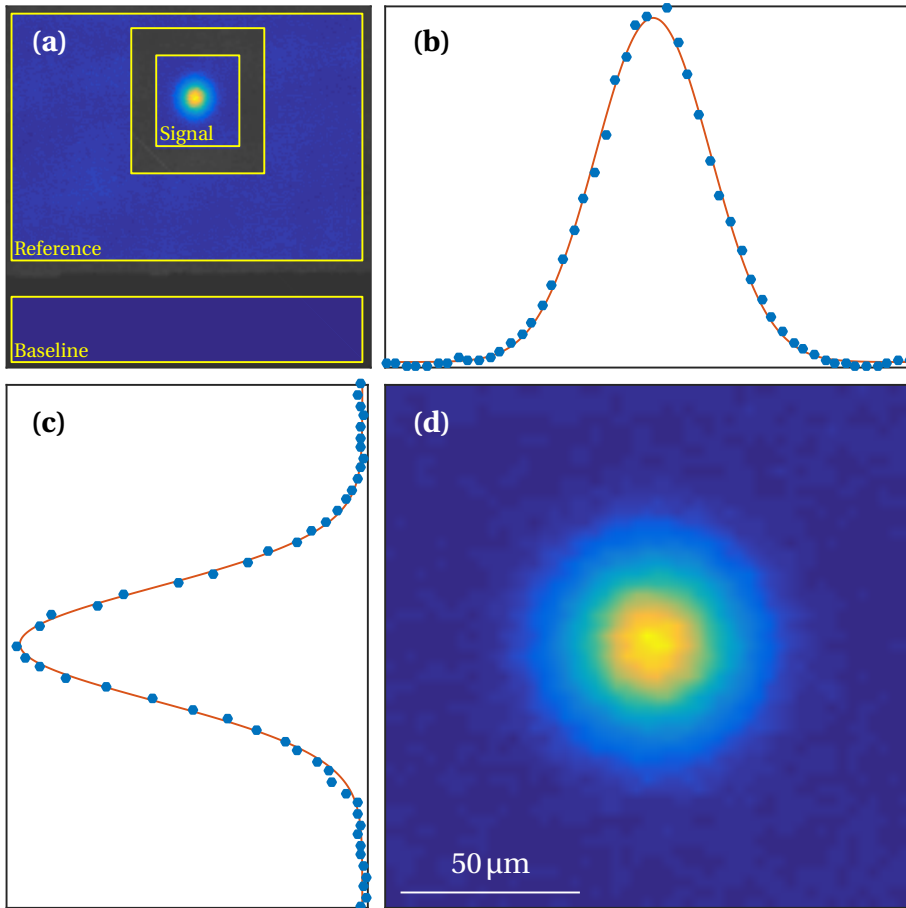


Figure 4.3: **(a)** Full frame of raw Faraday Image. The ROIs for signal (innermost square), reference (outermost square, excluding a safety margin) and baseline (bottom square) are indicated. The greyed areas are discarded safety margins. **(b,c)** Cross sections of evaluated signal (blue points ●) with corresponding cross sections of the fits of Eq. (4.6) (red line —). **(d)** Evaluated Faraday signal S . Adapted from [99]

quantity of interest is the Faraday ‘signal’ S defined as

$$S \equiv \sin^2(\theta). \quad (4.3)$$

The evaluation of the signal requires knowledge of the ‘rotated’ light and the intensity incident on the atoms. Due to the finite extinction ratio of the PBS, a small amount of light leaks through polariser also in the absence of an atomic density. The incident intensity can thus be estimated from the area surrounding the cloud. The detected light intensity is

$$I(\theta) = \sin^2(\theta)I(\frac{\pi}{2}) + \cos^2(\theta)I(0), \quad (4.4)$$

where $I(0)$ is the detected light in the absence of any rotation, and $I(\frac{\pi}{2})$ is the detected light for maximal rotation of $\theta = \frac{\pi}{2}$. The cube extinction ratio is characterised by the ‘cube suppression’ $CS = I(0)/I(\frac{\pi}{2})$, which is measured to $CS = 1.5 \times 10^{-3}$. By isolating $\sin^2(\theta)$, we obtain a simple expression for the Faraday signal

$$S = \left(\frac{I(\theta)}{I(0)} - 1 \right) \left(\frac{CS}{1 - CS} \right). \quad (4.5)$$

The signal is evaluated in the central signal ROI marked in Fig. 4.3(a). The leakage light $I(0)$ is taken as an average intensity in a reference region around the atoms. Both $I(\theta)$ and $I(0)$ are corrected for the baseline level of the camera, which is analysed in an area masked by a knife blade. The evaluated signal is shown in Fig. 4.3(d).

This simple evaluation of the Faraday signal is suitable for implementation on a FPGA, which has allowed us to obtain real-time information on the cloud properties during individual experimental runs [35]. Note also that an absolute intensity-calibration is not required. If structure in the profile of the imaging beam are important, reference images can be used for the evaluation in post-processing.

4.3.2 Absolute atom number and temperature

To extract atom numbers and temperatures from the Faraday images, we can work directly with the signal S or reconstruct the rotation angles from the evaluated signal.

Equation (4.1) links the atomic density to the Faraday rotation angles. Evaluating the angles allows us to determine the total atom number given by the area integral of the angle distribution scaled by the Faraday coefficient $\Sigma_\theta / c_F(\Delta_{\text{eff}})$. The angle sum Σ_θ can be obtained either by summation of the angles in all pixels, or by fitting the angle distribution. The in-trap distribution of a thermal cloud in a harmonic trap sufficiently above T_c is Gaussian. The distribution θ_G of the angles is thus a 2D Gaussian distribution given by Eq. (2.34) scaled by the Faraday coefficient $c_F(\Delta_{\text{eff}})$. The fit yields a measure of both the atom number N and the temperature T . The Faraday rotation angles can be reconstructed from the evaluated signal through $\theta = \arcsin(\sqrt{S})$, but this approach has two important drawbacks. First, since the baseline is subtracted, the pixel counts for pixels with low signal can become negative, which is problematic when evaluating the square root. Secondly, the steep derivative of the square root for small arguments amplifies the noise in pixels with low rotation angles. The areas at the edge of the cloud will thus contribute a larger proportion of the noise to the integrated signal.

To avoid these complications we obtain better results by working directly with the signal S . Atom number and temperature are obtained by fitting the evaluated signal directly with

$$S_G(x, y) = S_G^{\text{max}} \sin^2(\theta_G). \quad (4.6)$$

Figure 4.3(b-c) shows cross sections of a 2-dimensional fit of Eq. (4.6) to the signal S . From the fit we obtain a more reliable value of Σ_θ .

Faraday imaging underestimates both the total atom number and temperature. As established in [31] the atom number is underestimated by a factor of 0.65(3) and the temperature by a factor of 0.82(9). This is at-

4.3. Characterisation of Faraday imaging

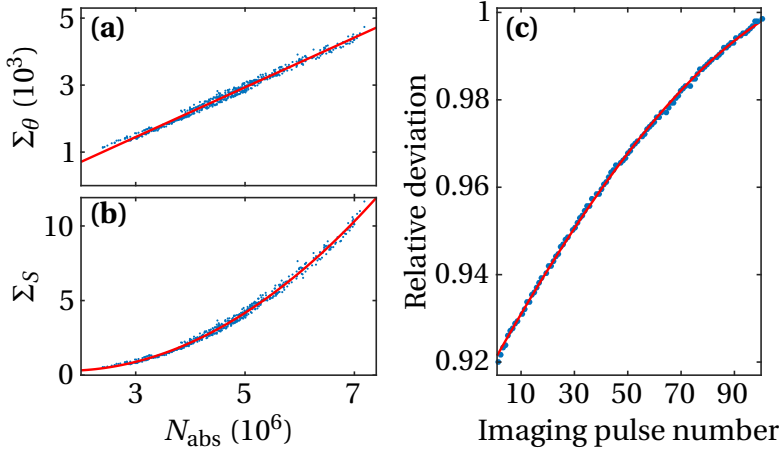


Figure 4.4: **(a)** Angle sum obtained from a fit of Eq. (4.6) as a function of the atom number determined by absorption imaging (blue points ●) and a fitted linear calibration curve (red line —). **(b)** Signal sum as a function of the atom number determined by absorption imaging (blue points ●) and a fitted quadratic calibration curve (red line —). **(c)** Ratio of atom numbers obtained from the use of calibrations in (a) and (b) as a function of image number in the imaging series (blue points ●). For the 100'th image the ratio is 1, as both the signal sum and angle sum are directly calibrated against absorption imaging. The data is fitted with a quadratic polynomial (red line —). Reproduced from [32].

tributed to density dependant collective scattering effects, which are not included in the light-scattering model [29]. However, with appropriate scaling, the method provides precise measurements with good accuracy.

Figure 4.4(a) shows a direct cross calibration of Σ_θ in the last image of each experimental realisation with the atom number extracted from absorption imaging. The loss of atoms due to the imaging samples a large range of atom numbers when the imaging pulse duration is varied.

Additionally, the initial atom number varies with a standard deviation of 12.5 % across all data sets. Σ_θ is linear in atom number. The data is fitted with $\Sigma_\theta = a_1(N - a_2)$, where a_2 models the lower bound for detection of small angles due to the finite extinction ratio of the PBS. The calibration allows us to convert the angle sum obtained for each image into an atom number.

4.3.3 Atom number from the Faraday signal sum

An alternative approach is to work only with the total signal sum

$$\Sigma_S = \sum S_{ij}, \quad (4.7)$$

where the sum runs over all pixels in the signal ROI. Σ_S is a scalar function of the atom number and temperature does not allow us to directly determine N and T . However, in our experiment, the evaporative cooling leads to a high degree of correlation between N and T since it relies on elastic collisions between atoms [101]. This makes the cloud properties a function of a single parameter, and the signal sum $\Sigma_S(N, T) = \Sigma_S(N)$ fully determines the cloud properties.

Typically the rotation angles are small ($< 15^\circ$), and the dependence of the signal sum Σ_S on atom number and temperature can be determined from the small angle approximation of Eq. (4.3)

$$S \approx \theta^2 = (c_F(\Delta_{\text{eff}})\tilde{n}_{\text{th}}(x, y))^2. \quad (4.8)$$

Inserting a 2D Gaussian distribution given by Eq. (A.5) for the column density, we see that the small angle dependence of the signal sum on number of atoms and temperature is

$$\Sigma_S \propto \frac{N^2}{T}. \quad (4.9)$$

The atom number can be extracted from the signal sum Σ_S by calibrating it versus the atom number extracted from absorption images. Figure 4.4(b) shows Σ_S as a function of the atom number from absorption imaging. Inspired by Eq. (4.9) the data is fitted with a quadratic function $\Sigma_S = b_1(N - b_2)^2 + b_3$. As for the case of the angle sum, b_2 models a lower bound on the atom number detection. b_3 models beam inhomogeneity that gives rise to an offset in the signal sum.

The calibration of the signal sum is only accurate for constant temperature. From absorption imaging the variation in temperature is observed to be less than 1.5%. The heating of the cloud is also negligible relative to the cloud temperature, and losses due to imaging occur mainly due to spontaneous decay into un-trapped states [32, 84]. However, over the course of the 100 images, there is a significant cooling due to free evaporation. The atom number is thus underestimated in the initial images due to the clouds being warmer (see e.g. Eq. (4.9)).

This issue can be solved by an extra calibration step. Figure 4.4(c) shows the ratio of the average atom number estimated from Σ_θ and Σ_S as a function of the image number. The signal sum underestimates the atom number in the first image by 8%. At the final image, both methods yield the same atom number, as both methods are calibrated directly against absorption imaging. The data is fitted with a quadratic function, which allows us to correct the atom number estimated from the signal sum. Despite the extra calibration step required to extract accurate numbers from the signal sum, the next section shows that it yields superior precision.

4.4 Precision of Faraday imaging

To obtain the best possible precision in any detection scheme, care has to be taken to minimise any sources of technical noise, such that we approach the limits set by the inherent fundamental noise sources. In our

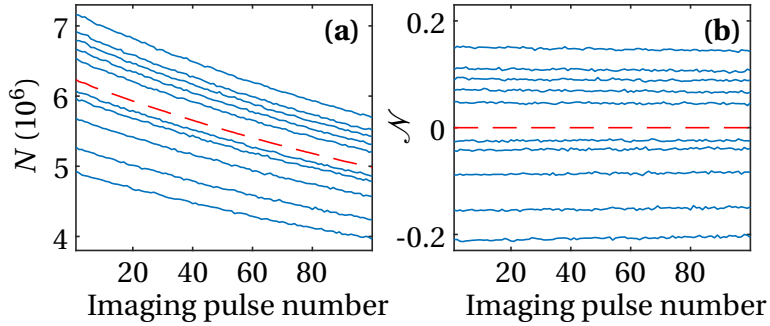


Figure 4.5: **(a)** Representative traces showing the decay of atoms during imaging with a pulse duration of $660 \mu\text{s}$. Red dashed line indicates mean atom number over entire dataset. **(b)** Traces showing relative deviation \mathcal{N} from mean atom number. Reproduced from [32].

scheme, the fundamental noise sources are photon shot noise and the stochastic uncertainty of the number of lost atoms due to the imaging. In addition the images suffer from other technical noise such as camera noise, which consists of readout noise, clock induced charges, thermal dark counts and spurious charges, but it also includes laser frequency instability, imaging light intensity instability and mechanical vibrations of the optical components along the imaging beam path. In particular, the readout noise can be detrimental due to the low number of photons per pixel in the reference area. To overcome the readout noise, we take advantage of the cameras electron multiplying (EM) feature to amplify the detected signal above the readout noise. The EM amplifier consists of a multi-stage avalanche-type amplification, and leads to a multiplicative noise term increasing the photon shot noise by a factor approaching $\sqrt{2}$ [102, 103]. The application of EM-gain and the large reference and baseline ROIs ensure that our imaging is limited by the noise in the signal ROI. In the following I show that the quantity that we determine with the best precision is the integrated signal Σ_S .

Figure 4.5(a) shows the evolution of the atom number during imaging with a pulse duration of 660 μs . The atom number is obtained from Σ_S using the calibration curves in Fig. 4.4(b,c). In Fig. 4.5(b) the same data is shown as normalised atom number

$$\mathcal{N}_{i,j} = \frac{N_{i,j}}{\langle N_{i,j} \rangle_{\text{runs}}} - 1, \quad (4.10)$$

where i denotes run number in a given dataset and j denotes image number in a given run. $\langle N_{i,j} \rangle_{\text{runs}}$ is the mean atom number in the j 'th image, averaged over all runs in the given dataset.

To characterise the measurement noise we evaluate a two-sample variance for all pairs of images along the individual traces

$$\sigma_N^2 = \frac{1}{2} \langle (N_{j+1} - N_j)^2 \rangle. \quad (4.11)$$

The two-sample variance can be evaluated for both the atom number traces and the normalised errors. It is two-sample variance is insensitive to sufficiently slow trends or drifts in the measurements, but captures the relevant noise contribution. Figure 4.6 shows the relative two-sample deviation, defined as the square root of the two-sample variance, for both the atom number and the normalised error.

To gain insight into the contributions of the different noise sources, expected photon shot noise and the noise due to loss of atoms is evaluated in the following. Both the detection of individual photons and the loss of atoms are examples of single particle events that leads to Poissonian statistics.

The photon shot noise can be evaluated directly from the Faraday image using the fact, that the detected number of photo-electrons N_{el} , generated when an incident photon hits the CCD, is distributed according to a Poissonian distribution with variance equal to the number of detected electrons. The uncertainty in the number of photo electrons

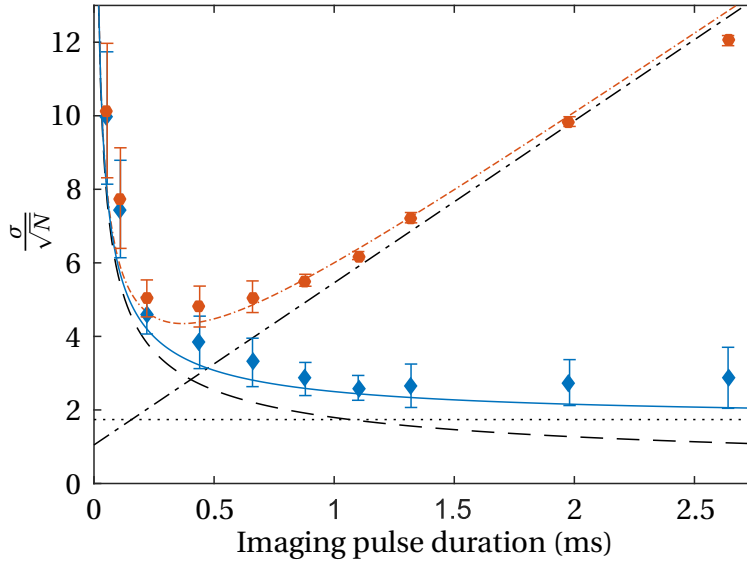


Figure 4.6: Relative two-sample deviation of the atom number (red points \bullet) and normalised deviation (blue points \blacklozenge) as a function of the pulse duration. The photon shot noise (dashed line ---) is dominant for short pulse durations. As the pulse duration is increased, the mean decay dominates the atom number deviation (dash-dot line -.-.-). By evaluating the normalised error the mean decay can be eliminated, and the noise continues to decrease, approaching a constant offset (dotted line). The solid lines are the relevant contributions added in quadrature for both cases. The total decay per image is so small that the stochastic noise is negligible. Error bars represent $1\text{-}\sigma$ statistical uncertainties. Reproduced from [32].

leads to an uncertainty in the detected signal given by [31]

$$\sigma_{\Sigma_S} = \sqrt{\frac{\Sigma_S}{N_{\text{el},0}}}, \quad (4.12)$$

where $N_{\text{el},0}$ is the number of electrons per pixel we would detect if the cloud and PBS were absent. We can evaluate this from the number of counts in the reference area by taking the camera gain and the cube suppression into account. The corresponding uncertainty in atom number can be calculated as $\sigma_{\text{psn}}^2 = (\partial N / \partial \Sigma_S)^2 \sigma_{\Sigma_S}^2$, where the error propagation coefficient is determined from the calibrations in Fig. 4.5(b,c). The photon shot noise is dominant for short pulses, but decreases as $1/\sqrt{t}$ when the pulse duration t is increased.

Atom loss leads to an increase in the atom number variance both due to the stochastic nature of the discrete particle loss and through the decay of the mean atom number. Assuming that only single-particle loss occurs, the variance due to loss is given by [104]

$$\sigma_{\text{loss}}^2 = \frac{N_0}{2\tau} t + \frac{N_0^2}{2\tau^2} t^2, \quad (4.13)$$

where N_0 is the atom number at the start of the imaging and τ is the lifetime during imaging. The lifetime is determined by fitting an exponential decay $N(t) = N_0 \exp(-t/\tau)$ to the atom number traces. The first term describes the noise due to the stochastic loss of atoms. The second term can be eliminated by removing the mean decay from the traces, as seen for the normalised errors. For all the pulse durations considered here, the stochastic noise in a single image is negligible.

Figure 4.6 shows that the photon shot noise σ_{psn} and the atom loss noise σ_{loss} plus a small contribution from technical noise σ_{tech} account well for the observed noise in single images. A likely candidate for the offset is the frequency stability of the detection laser. The laser has a 1 MHz line width after 5 ms integration, corresponding to $\sim 1 \times 10^{-3}$ relative detuning noise. Through error propagation using Eq. (4.1) this corresponds to $\sim 5 \times 10^{-4}$ relative noise in the detected number of atoms. The time scale is similar to the time between consecutive images, and is therefore expected to be independent of the pulse duration.

4.4.1 Multi-image detection

In principle, the variance keeps decreasing as the pulse duration is increased when the data is corrected for the mean decay, as is the case for the normalised errors. In practice, however, the pulse duration is limited by the dynamical range of the camera, especially because sufficient EM-gain is necessary to render the readout noise negligible when imaging small rotation angles. To artificially increase the dynamical range of the camera, we can exploit the non-destructive nature of our detection by acquiring multiple images and average the result. For uncorrelated noise, the standard deviation of the mean decreases with the number of images n as $\frac{1}{\sqrt{n}}$. This is the case for the shot noise and a fair assumption for the technical noise offset. This is not the case for the stochastic atom loss noise, which is correlated, because the width of the atom number distribution reflects the random walk in atom number during all previous images.

To see how the stochastic noise grows as the number of images increases, assume for the moment that our images are only susceptible to the stochastic loss of atoms, and no other detection noise influences the precision. After every image, a certain mean fraction of atoms remain, characterised by a survival probability $p = e^{-t/\tau}$. The mean atom number $\langle N_k \rangle$ in the k 'th image is

$$\langle N_k \rangle = \langle N_{k-1} \rangle p = N_0 p^k. \quad (4.14)$$

N_0 here implies the initial 'true' atom number. The loss of atoms leads to a stochastic step ΔN_k during every image leading to a random walk away from the mean behaviour. The actual atom number detected in the k 'th image is therefore

$$N_k = N_{k-1} p + \Delta N_k = N_0 p^k + \sum_{j=1}^k \Delta N_j. \quad (4.15)$$

4.4. Precision of Faraday imaging

ΔN_j are independent random variables distributed according to a Poisson distribution with variance $\text{Var}(\Delta N_j) = N_j(1 - p)$ and $\langle \Delta N_j \rangle = 0$. If we wish to estimate the initial atom number $\tilde{N}_{0,k}$ from the k 'th image we get

$$\tilde{N}_{0,k} = N_k p^{-k} = N_0 - p^{-k} \sum_{j=1}^k \Delta N_j. \quad (4.16)$$

The average estimate over all n images is then

$$\tilde{N}_0 = \frac{1}{n} \sum_{k=1}^n \tilde{N}_{0,k} = N_0 - \frac{1}{n} \sum_{k=1}^n p^{-k} \sum_{j=1}^k \Delta N_j. \quad (4.17)$$

The order of summation can be swapped since $j \leq n$ and $k \geq j$. Defining $\Delta \tilde{N}_0 = \tilde{N}_0 - N_0$ we obtain

$$\Delta \tilde{N}_0 = \frac{1}{n} \sum_{j=1}^n \Delta N_j \sum_{k=j}^n p^{-k} = \sum_{j=1}^n w_{n,j} \Delta N_j, \quad (4.18)$$

where I have defined the 'weighting factor', $w_{n,j} = \sum_{k=j}^n p^{-k} / n$. The summation corresponds to a geometric series, and is thus given by

$$w_{n,j} = \sum_{k=j}^n \frac{p^{-k}}{n} = \frac{1}{n} \frac{p^{-j} - p^{-(n+1)}}{1 - p^{-1}}. \quad (4.19)$$

The variance of the mean due to the stochastic atom loss is then

$$\sigma_{\text{stoch}}^2 = \text{Var}(\Delta N_0) = \sum_{j=1}^n w_{n,j}^2 \text{Var}(\Delta N_j), \quad (4.20)$$

and using the fact that $\text{Var}(\Delta N_j) = N_j(1 - p)$

$$\sigma_{\text{stoch}}^2 = \sum_{j=1}^n w_{n,j}^2 N_j(1 - p) = N_0(1 - p) \sum_{j=1}^n w_{n,j}^2 p^j. \quad (4.21)$$

This shows that the stochastic atom loss noise of an average over n image is increased by the factor $\sum_{j=1}^n w_{n,j}^2 p^j$. For our typical imaging conditions with an average over 50 images and a total illumination time of 33 ms this corresponds to a factor of 108.

To obtain experimental measures of the detection precision data from the single image characterisation is reused. The data sets are first split in two, the first set containing images 1:50 and the second set containing 51:100. The number of images included in the average can now be varied for $1 \leq n \leq 50$. The normalised atom number averaged over n consecutive images is denoted \mathcal{N}_1^n and \mathcal{N}_2^n corresponding to the two sets of images. The two averages are ‘taken from the middle’ of the imaging series and always includes image number 50 and 51. Figure 4.7(a) shows the correlation of \mathcal{N}_1^{50} and \mathcal{N}_2^{50} for a pulse duration of 0.88 ms. The correlation is fitted with a quadratic polynomial. The deviation $\Delta\mathcal{N}^{50}$ from the polynomial is shown in Fig. 4.7(b).

A slow drift of $\Delta\mathcal{N}^{50}$ is seen in Fig. 4.7(b). The trend arises from drifts in the experimental apparatus, of which the main cause is small variations in the temperature of the cooling water for the magnetic trap. To evaluate the inherent noise of the detection, a two-sample deviation in time is used to reject the trend.

By varying the number of images included in the average, we determine the precision as number of images shown in Fig. 4.7(c). The blue line shows the measured imaging noise as function of the number of images included in the average. The shaded bound denotes the uncertainty on the measured detection noise, which is obtained by bootstrapping the dataset.

The total noise model consists of photon shot noise, stochastic noise and technical noise. For the photon shot noise and technical noise the result from the single image precision scaled with the number of images is used. The stochastic noise is given by Eq. (4.21). The noise model is

4.4. Precision of Faraday imaging

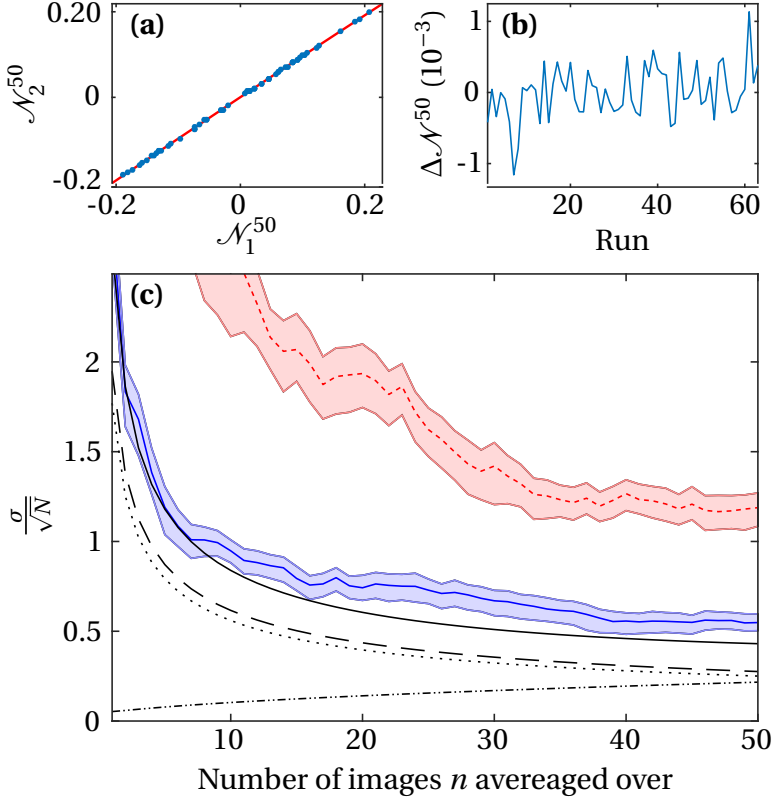


Figure 4.7: **(a)** Correlation of the normalised atom number \mathcal{N}_1^{50} and \mathcal{N}_2^{50} for an average over 50 images. A quadratic fit is applied to the data. **(b)** Deviation of \mathcal{N}_2^{50} from the fitted dependence. **(c)** Experimental imaging noise and noise model. The blue curve shows the measured noise and the red dashed line shows the imaging noise when fitting the Faraday images to extract Σ_θ . The shaded areas are 1- σ confidence bounds obtained by bootstrapping the data. The lines showing the imaging noise models correspond noise due to stochastic atom loss (dot-dot-dash), technical noise (dotted), photon shot noise (dashed) and full noise model (black solid). Reproduced from [32].

thus given by

$$\sigma_N = \sqrt{\frac{\sigma_{\text{psn}}^2}{n} + \frac{\sigma_{\text{tech}}^2}{n}} + \sigma_{\text{stoch}}. \quad (4.22)$$

The agreement between the model and the data is excellent considering the model contains no free parameters. The parameters are calculated from the statistics of the experimental data and the estimate of the laser frequency noise.

The data and model in Fig. 4.7(c) is scaled by \sqrt{N} determined as the average atom number in image 50 and 51. It is therefore readily seen that for $n > 10$ corresponding to a ~ 10 ms pulse duration we achieve sub-shot noise detection.

The same analysis can be performed with atom numbers extracted by directly fitting the signal distributions to obtain Σ_θ , which is also shown in Fig. 4.7(c). We obtain excellent precision with this method, but as the fitting routine introduces extra uncertainty which prevents sub-shot noise limited detection. Interestingly it is worthwhile to average over more images when using this approach. Still it is evident that the total atom number can be evaluated with high precision even in cases where the calibration with absorption images is not an option.

FEEDBACK-STABILISED PREPARATION OF ULTRACOLD CLOUDS

In the field of ultracold atoms, many experiments operate under fluctuating starting conditions for experiments. The general experimental procedure for preparation of ultracold atom clouds were outlined in Chapter 3. In our experiment, the biggest culprits are a fluctuating efficiency of the cooling and initial load of atoms in the MOT, the transfer from the MOT to a magnetic quadrupole trap and transport of the cloud through a differential pumping stage. This leads to fluctuating starting conditions for the subsequent evaporative cooling, and causes both atom number and temperature of the sample to vary, leading to shot-to-shot fluctuations of the initial conditions for an experiment. Since many ex-

periments are sensitive to the cloud density, precise preparation of the total atom number holds the potential to increase performance of atomic clocks through reduction of density-dependant collisional shifts [36] and a reduction of the linewidth of atom lasers [37].

In this chapter I present our work on using our implementation of fast and precise Faraday imaging to produce actively stabilised samples of ultracold clouds. Using the non-destructive Faraday imaging presented in the preceding chapter, we have implemented a feedback stabilised preparation scheme for ultracold atoms. By measuring the atom number during cooling sequence, we can discard excess atoms to reduce shot-to-shot number fluctuations. The feedback preparation has enabled us to study the atom number fluctuations of BECs, which is the subject of Chapter 6.

The work on feedback stabilised production of ultracold clouds were initiated by Miroslav Gajdacz during his Ph.D. studies. He wrote the bulk of the LabVIEW FPGA-code that interfaces a RF-synthesiser for the evaporative cooling and the camera for the Faraday imaging, which is described in his thesis. Additionally, his thesis includes strategies to evaluate temperature and atom number on the FPGA [84].

Together we acquired the data and performed the analysis for the experiments demonstrating preparation of ultracold atom clouds at the shot noise level based on the Faraday signal alone. This result was published in Physical Review Letters [35], and is covered in the first part of the chapter. Since Miroslav's departure, I have continued the development of the tool, and the chapter concludes with a current status of how we now apply and use the stabilisation technique.

The body text and figures from Chapter 3 of my progress report [99] is reused for this chapter. Many additional details are included throughout the following chapter, and the structure has been changed to improve the flow of the text.

The chapters opens with a description of implementation of FPGA analysis of the Faraday images, and the RF control using the FPGA. Then

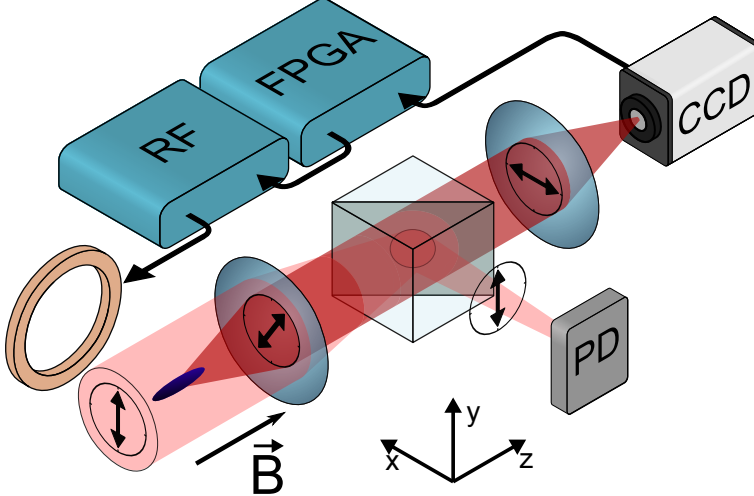


Figure 5.1: Set-up for feedback stabilisation. The Faraday images are read out from the camera to an FPGA. The FPGA controls an RF-synthesiser that generates the RF-radiation for evaporative cooling and loss pulses via an RF antenna. The rest of the figure is explained in the caption of Fig. 4.1. Adapted from [99].

follows a section on characterisation of the stochastic noise due to RF induced loss of atoms. This is important, as it will limit the precision of the stabilisation procedure. After that, the procedure to actively stabilise the preparation is presented, along with the performance of the stabilisation of the Faraday signal. Lastly, the final part is devoted to strategies to stabilise the absolute atom number rather than the Faraday signal.

5.1 Experimental implementation

To actively stabilise the production of ultracold clouds, two requirements must be met. Information about the relevant properties of the clouds,

such as atom number and temperature, must be obtained in a manner that does not destroy the system. Additionally, this information must be processed in real-time such that the preparation sequence can be adapted to yield clouds with the desired properties. Non-destructive Faraday imaging with a fast real-time analysis of the images on a FPGA meets these criteria.

Our experimental control system is a home-written program denoted ECS and written in Delphi 7, which has been in use for more than 12 years. It controls most hardware and timing of an experimental sequence through two DIO64 64-channel digital input/output cards. Once the sequence is buffered to the cards there is no possibility for changing the sequence during runtime.

The FPGA extends the capabilities of the experimental control system. The model we use is an NI PCIe-7852R operating on a 40 MHz clock. It runs in parallel with the main experimental control system synchronised through a digital channel. It has taken over the control of frequency of the RF for evaporative cooling and timing of the Faraday imaging. The reconfigurable logic of the FPGA allows us to implement data analysis algorithms that can adapt the experimental sequence during runtime.

5.1.1 Analysis of Faraday images on the FPGA

Faraday imaging was treated in Chapter 4. To use the images for stabilisation, the imaging set-up is expanded as illustrated in Fig. 5.1. The Faraday images are read out from the camera and streamed in parallel to the computer and the FPGA. This enables real-time analysis of the images on the FPGA while the images still get stored for later post-processing.

Figure 5.2 shows a typical raw Faraday image, in which the three ROIs are indicated. The calculation of the Faraday signal is given by Eq. (4.5) on page 73. The simple relation is attractive for implementation on the FPGA. By treating the incident intensity and baseline counts as constant across all pixels we only need to store the average values. The incident

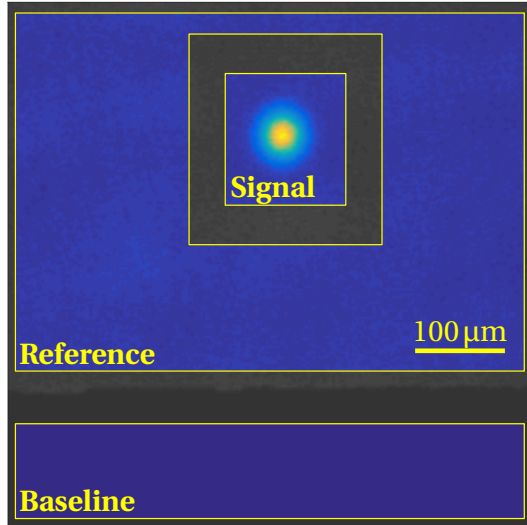


Figure 5.2: Example of a raw Faraday image of a thermal cloud with $\sim 6.7 \times 10^6$ atoms at a temperature of $18 \mu\text{K}$. The Signal, Reference, and Baseline ROIs are indicated. The image size is 220×200 pixels. The grey shaded areas are disregarded during the evaluation of the images. Adapted from [99].

intensity and baseline counts can thus be evaluated already during image readout by accumulating the sum of the pixel counts in the reference and baseline regions, respectively.

The same procedure can be used to obtain the signal sum Σ_S . In practice the entire signal region is stored to the memory of the FPGA, since this allows us to obtain extra information such as the image centre of mass and peak signal in addition to the signal sum. Strategies to extract approximate temperature and atom numbers are given in the thesis of Miroslav Gajdacz [84]. These are not currently implemented, since the signal sum provides superior precision as shown in Chapter 4.

5.1.2 RF control

The FPGA directly controls the frequency output of the direct digital synthesis (DDS) synthesizer used as the source for the RF radiation for the evaporative cooling. While the DDS is capable of both static and swept output, the interfacing of the DDS with the FPGA is only capable of setting static outputs. However, the FPGA can update the frequency every $8.4\ \mu\text{s}$, which is sufficient to emulate a swept output for RF evaporative cooling.

In order to apply feedback to the evaporative sequence, a method to remove atoms from the trap is required. The direct control of the RF source makes a transient pulse of RF radiation the ideal candidate. The pulse transfers atoms to an untrapped state and expels them from the trap.

The FPGA only controls the frequency of the radiation, while the power is controlled by the main control program ECS. Therefore the amount of loss induced is determined by the duration of the RF pulse. Since the pulse duration is discretised in units of $8.4\ \mu\text{s}$, we refer to the duration as loss pulses, such that 10000 loss pulses corresponds to a total duration of 84 ms.

5.2 Characterisation of RF induced losses

The feedback scheme relies on correlation of the two measurements denoted F1 and F2. Using the measurement at F1 as a precursor for predicted atom number later in the sequence, the loss induced after F1 is adjusted to provide the desired target atom number at F2. It is thus important to carefully characterise the correlation between the two measurements in the presence of loss to determine the limitations of the feedback scheme.

The loss of atoms due to the loss pulses is a 1-body process, and

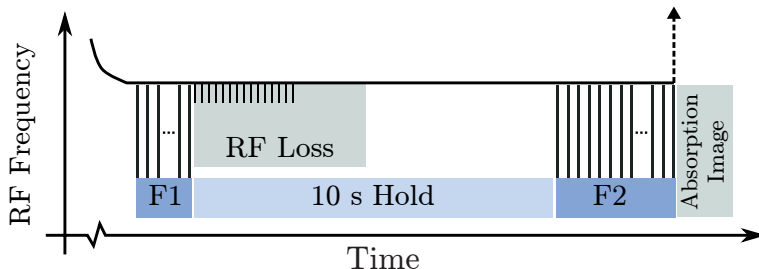


Figure 5.3: Schematics of the experimental sequence. F1 and F2 are two Faraday imaging series of 50 and 100 images, respectively. The total time for applying all loss pulses is less than 5 s. Adapted from [99]

the resulting loss is stochastic. Using Faraday imaging as a precise non-destructive detection technique, we have experimentally characterised the evolution of the atom number distribution under application of the loss.

The experimental sequence for non-destructive probing and feedback is illustrated in Fig. 5.3. Beforehand, the cloud is evaporatively cooled by sweeping the RF-frequency. At 1900 kHz the frequency is kept constant, until it is finally raised during TOF and absorption imaging. On average, we prepare clouds with 6.7×10^6 atoms at a temperature of $18 \mu\text{K}$ in the $|F = 2, m_F = 2\rangle$ state.

The initial sample is probed by a set of 50 Faraday images with a total illumination time of 33 ms, corresponding to the optimal probing time in Fig. 4.7. The imaging pulses are generated with an AOM, where the AOM driver is controlled by the FPGA. The pulse power is monitored on the photo detector on the reflected port on the cube after the chamber illustrated in Fig. 5.1. Since only a tiny fraction of the light is sent to the camera, we can use the photo detector signal to stabilise the light intensity with a feedback loop running on the FPGA. This is important to avoid that a fluctuating light intensity induces a varying loss of atoms.

Following the first imaging series a loss of atoms is induced. The discarded fraction is controlled by the number of pulses. The loss pulses consists of a sudden reduction of the RF frequency to 95 % of the trap depth. This cuts away the tail of the thermal energy distribution, leading to a tiny fractional loss of atoms of $\sim 10^{-5}$. This provides a fine digital control over the total induced loss. The pulses truncate the thermal distribution by removing predominantly the hottest atoms, which has two consequences. First, the loss pulses lead to unwanted cooling of the sample. Section 5.4 discusses ways to circumvent this. Secondly, the tail of the thermal distribution is depleted after a single loss pulses. To allow the tail to repopulate, the loss pulses are separated by $50.4 \mu\text{s}$, where the RF frequency is raised to the original values. In less than 4 s a loss of 45 % of the atoms can be achieved by applying 60 000 loss pulses.

To allow the cloud to rethermalise after the application of the loss pulses, the cloud is held in the trap for a total of 10 s including the time for the loss pulses. It is then probed by a final imaging series F2 consisting of 100 Faraday images with a total illumination time of 55 ms. Finally, the trap is turned off and an absorption image in time of flight is obtained, which provides an independent measure of atom number and temperature.

The limitation to the preparation scheme was characterised by determining the correlation between the measurements two Faraday measurements with a fixed loss applied in-between. The fixed loss was varied between 25 % to 85 % atoms discarded, and around 50 runs were collected per setting. The 25 % loss occurred naturally during the hold without any loss pulses. To reduce the lost fraction, the in-trap hold time between F1 and F2 were shortened for three datasets. The initial atom number fluctuates by $\sim 10 \%$.

To quantify the degree correlation, the mean signal error $E1$ and $E2$

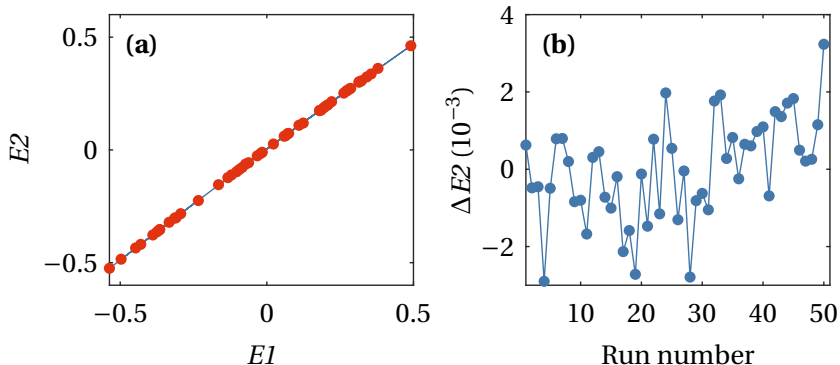


Figure 5.4: **(a)** The normalised errors for the first and second imaging series (\bullet) with a quadratic fit applied (—). **(b)** The error $E2$ with the quadratic fit subtracted as a function of run number (\bullet).

for the two imaging series is determined. It is defined as

$$E1 = \frac{\overline{\Sigma_{S,F1}}}{\langle \overline{\Sigma_{S,F1}} \rangle} - 1, \quad (5.1)$$

where $\overline{\Sigma_{S,F1}}$ is the mean signal sum over all images in corresponding imaging series for the given experimental realisation, and $\langle \overline{\Sigma_{S,F1}} \rangle$ is the average mean signal sum over all experimental realisations in the dataset. $E2$ is calculated in a similar fashion. The error $E2$ is plotted as a function $E1$ in Fig. 5.4(a) for 2000 loss pulses.

For each dataset, the degree of correlation is evaluated by first applying a quadratic fit to $E2$ as a function of $E1$, which is seen in Fig. 5.4(a). The fit is almost linear with a very weak quadratic dependence. Figure 5.4(b) shows the error residual $\Delta E2 = E2 - E2_{\text{fit}}$ obtained by subtracting the fit from $E2$.

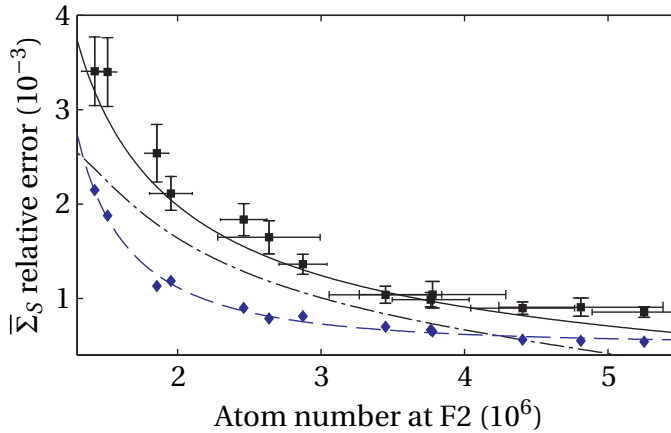


Figure 5.5: Faraday signal uncertainty as a function of number of atoms remaining in trap at F2. (■) Relative uncertainty in signal sum at F2. (♦) light shot noise contribution to atom number noise. (---) fit $\propto 1/N$ to light shot noise data. (-·-·-) stochastic atom loss noise contribution $\sqrt{(1-p)/\langle N \rangle}$. (—) Total noise model given by Eq. (5.9). Error bars are obtained by bootstrapping the data set. Adapted from [99].

A two-sample deviation is used as a measure of the degree of correlation, since this eliminates the influence of slow drifts in the experimental apparatus and environment, such as variations in the ambient magnetic field, on the observed correlations. It is shown in Fig. 5.5 as a function of the atom number at F2 determined by absorption imaging. Lower atom number corresponds to a larger induced loss. For larger loss the relative error grows due to the increasing stochastic loss of atoms. In the following, a model of the expected uncertainty will be developed.

5.2.1 Noise growth due to stochastic loss of atoms

The observed correlations are limited by the detection precision of the two Faraday measurements, and the growth of noise due to the stochastic nature of the atom loss. Here, the stochastic part is treated.

The loss is dominated by single particle loss, and we neglect two- and three-particle loss process. If N_0 is the initial atom number, we model the probability that exactly N atoms out of N_0 survive using a binomial distribution. If p is the survival probability of an atom, the mean and variance of the binomial distribution is

$$\langle N \rangle = N_0 p, \quad (5.2)$$

$$\text{Var}(N) = N_0 p(1 - p). \quad (5.3)$$

The relative uncertainty in the remaining number of atoms is therefore

$$\sigma_N = \frac{\sqrt{\text{Var}(N)}}{\langle N \rangle} = \sqrt{\frac{1 - p}{\langle N \rangle}} = \sqrt{\frac{d}{\langle N \rangle}}, \quad (5.4)$$

where the destructivity $d \equiv 1 - p$ has been introduced. When the destructivity approaches 1 the uncertainty approaches $1/\sqrt{N}$, which is often called the atom shot noise limit. We approximate the survival probability based on the mean atom number $\langle N_k \rangle$ ($k = 1, 2$) in the two imaging series as $p = \langle N_2 \rangle / \langle N_1 \rangle$, and the resulting relative uncertainty σ_N in atom number at F2 becomes

$$\sigma_N \approx \sqrt{\frac{1 - \langle N_2 \rangle / \langle N_1 \rangle}{\langle N_2 \rangle}}. \quad (5.5)$$

To compare this expression with the observed correlations, we need to determine how noise in atom number propagates into noise in the Faraday signal sum Σ_S . This is achieved by determining Σ_S as a function of the atom number N and temperature T extracted from absorption

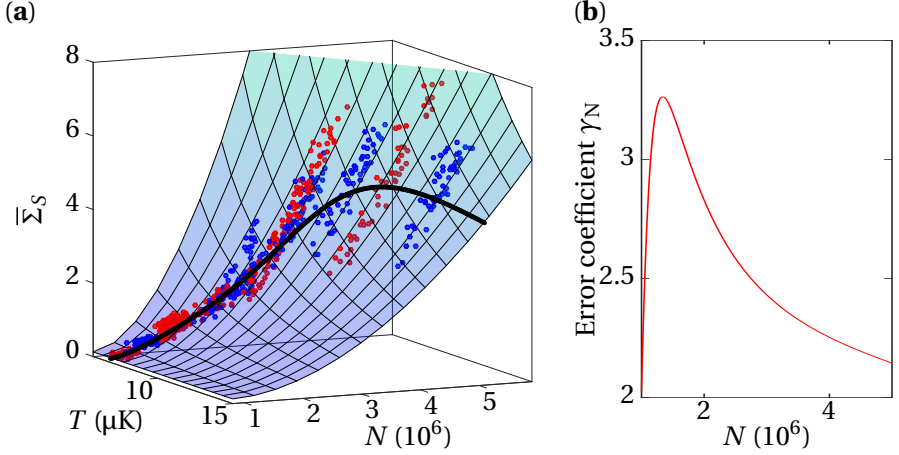


Figure 5.6: **(a)** Signal sum $\bar{\Sigma}_S$ as a function of atom number and temperature obtained from absorption images. Alternating red and blue points distinguish different datasets. The error propagation coefficient Eq. (5.8) is evaluated along the black line going through the mean values of each dataset. **(b)** Error propagation coefficient describing the propagation of uncertainty in atom number into uncertainty in signal sum. Adapted from [99].

imaging. The data is shown in Figure 5.6. The data is fitted with a surface inspired by the small angle dependence $S \approx \theta^2$. The in-trap density distribution is a Gaussian given by Eq. (2.34), and therefore $\theta \propto N/T$. When we integrate over the cloud area we obtain $\Sigma_S(N, t) \propto N^2/T$. Using this as inspiration, we allow the coefficients to vary to have a more general dependence that is not constrained to the small-angle limit. Hence, we use the fitting function

$$\bar{\Sigma}_S(N, T) = a_1 \frac{(N - a_5)^{a_2}}{\left(\frac{T}{1\mu\text{K}}\right)^{a_3}} + a_4. \quad (5.6)$$

Here T is in units of μK . The offset a_4 accounts for inhomogeneity in the beam leading to an offset in the signal sum. a_5 accounts for a lower limit for detection of small angles due to the finite extinction ratio of the PBS cube in the imaging set-up. The fitted parameters are $a_1 = 18.3(16) \times 10^{-18}$, $a_2 = 1.82(3)$, $a_3 = 1.51(3)$, $a_4 = 0.13(5)$ and $a_5 = 8.0(7) \times 10^5$.

The temperature varies in a correlated manner with the atom number for a fixed applied loss. The variation is though ~ 10 times smaller than the variation in atom number, and due to the signal sum dependence $\Sigma_S(N, t) \propto N^2/T$ this implies that the influence of temperature variation on the signal sum is ~ 20 times smaller than atom number variation. As such, we neglect temperature variations in our noise model, and only need the error propagation coefficient for atom number γ_N

$$\sigma_{\Sigma_S} = \frac{\partial \overline{\Sigma_S}}{\partial N} \frac{\langle N \rangle}{\langle \Sigma_S \rangle} \sigma_N = \gamma_N \sigma_N. \quad (5.7)$$

The resulting error propagation coefficient is

$$\gamma_N = a_2 \left(1 - \frac{a_4}{\Sigma_S(N, T)} \right) \left(1 - \frac{a_5}{N} \right)^{-1}. \quad (5.8)$$

The coefficient is evaluated along a trajectory following the mean values of every dataset in Fig. 5.6(a). The resulting coefficient is shown in Fig. 5.6(b). For large atom numbers, the coefficient approaches the value 2 as expected from the simple dependence $\Sigma_S(N, T) \propto N^2/T$. The coefficient goes to zero for low atom numbers since they are undetectable due to the finite cube suppression. The coefficient is used to generate the curves for the expected stochastic noise terms of signal $\gamma_N \sigma_N$, shown alongside the measured noise in Fig. 5.5.

The detection noise σ_{det} of Faraday imaging is the second contribution to the expected correlations. It is obtained for every dataset by evaluating the two-sample variance Eq. (4.11) for the normalised signal

traces. This includes light shot noise and a small contribution from technical noise (see Fig. 4.6 for corresponding precision in atom number), but neglects the accumulated stochastic loss detection noise due to averaging the signal in multiple images. For simplicity the loss due to imaging is instead included in the total loss between F1 and F2 and contributes to σ_N . The detection noise is shown in Fig. 5.5 along with a $1/N$ fit expected from the shot noise dependence Eq. (4.12).

Assuming the noise is uncorrelated, the expected noise is then

$$\sigma_{\text{tot}} = \sqrt{\sigma_{\text{det}}^2 + \gamma_N^2 \sigma_N^2} \quad (5.9)$$

As shown in Fig. 5.5, the observed correlations at F2 are well described by the this model. This shows that there are no unknown noise sources, which is a requirement for achieving atom number stabilisation below the shot noise limit.

5.3 Active stabilisation of Faraday Signal

The ability to perform on-line image evaluation and control the RF synthesiser enables us to actively stabilise the atom number. By varying the number of loss pulses N_{pulses} based on the mean signal sum at F1, we can correct for fluctuations of the initial atom number.

The amount of loss required is determined in real-time on the FPGA in two steps. First, the a dimensionless error is calculated. It corresponds to the ratio of the mean Faraday signal $\bar{\Sigma}_{S,F1}$ to a reference signal $\langle \bar{\Sigma}_{S,F1}^{\text{ref}} \rangle$. The reference signal is the average signal in F1 from at least 30 pre-recorded experimental realisations where no loss were applied. The dimensionless error with respect to the reference data is given by

$$EI^{\text{ref}} = \frac{\bar{\Sigma}_{S,F1}}{\langle \bar{\Sigma}_{S,F1}^{\text{ref}} \rangle} - 1, \quad (5.10)$$

The same quantity $E2^{\text{ref}}$ can be calculated for the second imaging series F2.

Next, the required number of loss pulses is determined. The loss pulses lead to an exponential loss of atoms, but since the feedback function must be implemented on the FPGA we approximate it by a cubic polynomial

$$N_{\text{pulses}} = gEI^{\text{ref}} \left(1 + qEI^{\text{ref}} + c(EI^{\text{ref}})^2 \right) + d_{\text{pulses}}, \quad (5.11)$$

where g , q , c are the linear, quadratic and cubic gains and d_{pulses} is the default number of loss pulses when $EI^{\text{ref}} = 0$. Hence, d_{pulses} corresponds to the fixed loss used in previous section.

5.3.1 Adjustment of feedback parameters

The feedback parameters are chosen through an iterative procedure. We first record the reference set, before enabling the loss. Then the loss is enabled with an initial set of feedback parameters. These are guessed based on experience, and may not yet yield a stable output. An example is shown in Fig. 5.7.

The natural fluctuations in starting atom number samples a range of EI^{ref} . Through the feedback function this causes the number of applied loss pulses N_{pulses} to vary accordingly. We can thus calibrate the loss pulses by determining the lost fraction $f_{\bar{\Sigma}_S}$ as a function of the number of loss pulses

$$f_{\bar{\Sigma}_S}(N_{\text{pulses}}) = \frac{\bar{\Sigma}_{S,F2}}{\bar{\Sigma}_{S,F1}}. \quad (5.12)$$

The ideal lost fraction would yield the stable signal $\bar{\Sigma}_{S,F2}^{\text{target}}$. It is thus given by

$$f_{\bar{\Sigma}_S}^{\text{ideal}} = \frac{\bar{\Sigma}_{S,F2}^{\text{target}}}{\bar{\Sigma}_{S,F1}}. \quad (5.13)$$

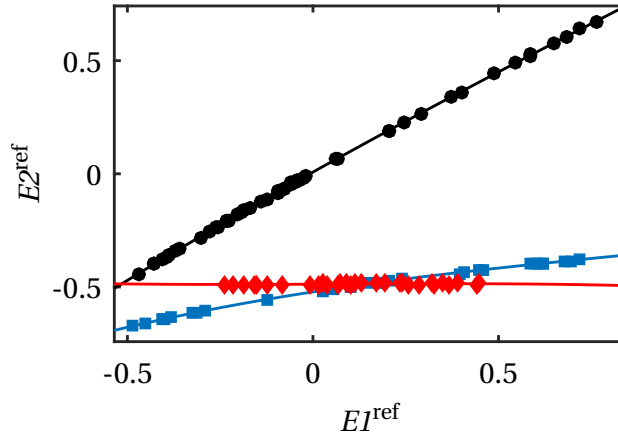


Figure 5.7: Correlation of the Faraday measurements at F1 and F2. (●) Correlation without feedback. (■) Correlation after feedback with trial feedback coefficients. (◆) Correlation with optimal feedback coefficients. The lines are quadratic fitted guides to the eye. Adapted from [99].

Equation (5.12) is inverted by fitting N_{pulses} as a function $f_{\Sigma_S}^-$ with a cubic polynomial. This allows us to determine the ideal number of loss pulses by

$$N_{\text{pulses}}^{\text{ideal}} = N_{\text{pulses}} \left(f_{\Sigma_S}^{\text{ideal}} \right). \quad (5.14)$$

Fitting $N_{\text{pulses}}^{\text{ideal}}$ as a function of EI^{ref} yields a set of improved feedback coefficients.

This procedure often needs to be iterated a few times. The stabilisation is done to the Faraday signal, which is non-linear in atom number. Additionally, the loss pulses induce an exponential rather than a linear loss, and both of these contribute to error on the outlined procedure. Hence, we typically iterate the parameters a few times. An example of

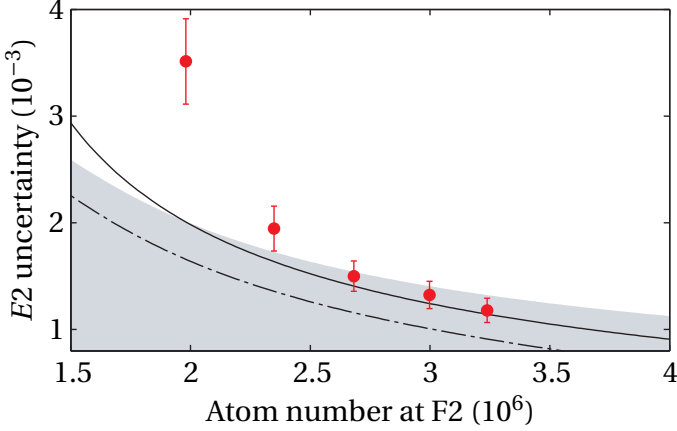


Figure 5.8: Result of stabilisation of Faraday signal. Red points represent two-sample deviation of feedback stabilized faraday signal, other lines same as Fig. 5.5. The shaded region indicates the interval where the relative uncertainty in the atom number lies below the level of Poissonian fluctuations, i.e., $1/\sqrt{N}$ expressed as signal sum. Adapted from [99].

optimal feedback parameters is shown in Fig. 5.7, where all variation in the relative signal sum $E2^{\text{ref}}$ is removed by the feedback.

5.3.2 Stabilisation at the shot noise limit

To evaluate the precision of our feedback stabilisation, we evaluate the two-sample deviation of the normalised error at F2

$$E2 = \frac{\overline{\Sigma_{S,F2}}}{\langle \overline{\Sigma_{S,F2}} \rangle} - 1. \quad (5.15)$$

$\overline{\Sigma_{S,F1}}$ is the average Faraday signal in F2 for a single experimental realisation, and $\langle \overline{\Sigma_{S,F2}} \rangle$ is the average over all experimental realisations. Note

that it is not with respect to the reference set in this case.

The two-sample deviation is evaluated without fitting the data in order that no residual variation is removed due to fitting. The result is shown in Fig. 5.8. For low levels of applied loss, we stabilise the signal at the level of the correlations with fixed loss, showing that our feedback does not induce any additional noise. For the smallest amounts of loss the stability is better than the Poissonian fluctuations $1/\sqrt{N}$. For the highest loss, the relative error is significantly larger than the corresponding correlations without loss. This is expected, since the approximation of the exponential loss by a cubic function becomes inaccurate. This highlights the importance of applying as weak a feedback as possible if the best precision possible is to be achieved. The fewer atoms we have to remove the closer we can approach the limit set by the detection, which as shown in the previous chapter is $0.5/\sqrt{N}$.

5.4 Atom number stabilisation

In the preceding experiments, we stabilised the Faraday signal, since it is the quantity we determine with the best precision. Unfortunately, a stable signal does not automatically imply stable atom number and temperature. The main reason is the nature of the loss pulses; the shallow RF cuts remove hot atoms as in evaporative cooling with RF. As seen in Fig. 5.6 the loss pulses lead to a cooling of the cloud, and in the preceding experiments a stable signal is achieved despite the variation in N and T .

To stabilise the atom number we have several options. First, we do not have to stabilise the signal to a constant value, but can instead let the target signal be a function of El . This requires detecting the absolute atom number with either absorption imaging or by fitting the Faraday images. Both these approaches exclude detecting sub-Poissonian correlations, as shown in Section 4.4.1 for the Faraday imaging. The performance of absorption imaging is worse than Faraday imaging, and is thus not a

viable option for atom number stabilisation below the shot noise level. Furthermore, the temperature will still be a function of El .

A second approach is to have evaporation between the applied loss and the detection at F2. The strong correlation of atom number and temperature during evaporation [101] will then lead to a situation, where temperature is a function of the atom number. The value of the signal sum $\Sigma_S(N, T) = \Sigma_S(N)$ thus unambiguously determines the properties of the cloud. Consequently, a stabilised signal at F2 implies simultaneous stable atom number and temperature. We did not adopt this approach here, however, because of the difficulties with stabilising the temperature of the cooling water for the magnetic coils in the trap. This causes the trap bottom to drift, an effect that is more severe for a shallower trap. Therefore we kept the RF-frequency constant to avoid trap bottom drifts during evaporation to become the dominant source of noise.

5.4.1 Loss induced at mean energy

The change in temperature is an undesirable side effect of the loss mechanism using the shallow cuts. A further option to obtain stable atom numbers is changing the way we induce the losses to avoid the cooling effect.

By adjusting the RF frequency of the loss pulses, we change the amount of energy removed by the lost atoms. Adjusted appropriately, we cut into the distribution at the mean energy. This leaves the temperature of the cloud unaffected by the losses. For deeper cuts, the temperature will increase, while shallower cuts leads to cooling.

The appropriate cut depth was determined experimentally. The number of loss pulses was varied for different cut depths, as seen in Fig. 5.9(a). Depending of the cut depth, the temperature increases or decreases. The traces were fit with a linear polynomial. Figure 5.9(b) shows the linear coefficient of the fit as a function of the cut depth. The zero-crossing

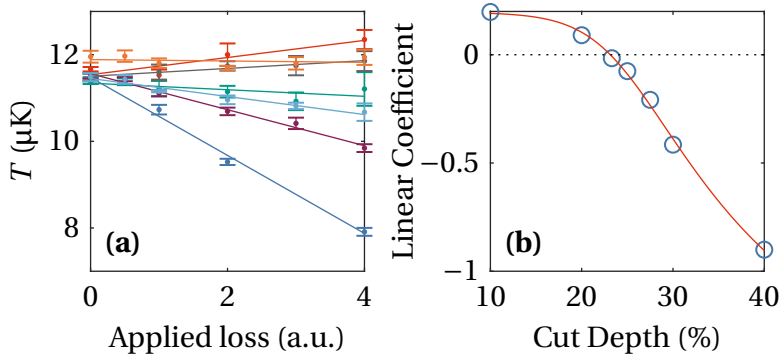


Figure 5.9: Experimental calibration of the cut depth. **(a)** The temperature variation as the loss is increased varies for different cut depths. The data is fitted with linear polynomials. **(b)** The linear coefficients of the fitted curves in (a) has a zero-crossing when the loss pulses do not change the temperature of the sample..

corresponds to the appropriate cut depth, which was found to be 23 % of the trap depth.

Since the density of atoms resonant at this lower frequency is much larger than for the shallow cuts, the RF power of the loss pulses has to be attenuated in order to retain the fine digital resolution of the loss induced by the pulses. Therefore we attenuate the RF power used for evaporation during the application of the loss pulses.

As an added benefit, the feedback can be applied faster with these deeper cuts. The RF pulses were previously applied with a delay between each pulse in order to repopulate the tail of the energy distribution. Since we only remove a tiny fraction of the resonant atoms, this hold time is no longer necessary. This allows us to apply the loss pulses continuously, effectively speeding up the application of the feedback by a factor of six. Furthermore the residual thermalisation, which was the reason for the

10 s hold in Fig. 5.3, is no longer required.

5.5 Summary

In summary, we have developed a tool to actively stabilise the preparation of ultracold atoms. A thermal cloud is probed by non-destructive Faraday imaging, during the evaporative cooling. Based on the measurement, a controlled fraction of the atoms is discarded to yield stable clouds from shot-to-shot.

The degree of correlation was measured between two Faraday measurements with loss applied in-between. It was demonstrated that the detection noise and the stochastic noise due to atom loss fully accounts for the observed variance. Additionally, we successfully stabilised the Faraday signal by actively controlling the amount of loss to the same level as the correlation measurements. This shows that the feedback scheme does not add additional noise.

Since these results were obtained the cooling water system for the magnetic trap was upgraded as described in Section 3.1.4. This mitigates some of the trap drifts observed. Once obtained, feedback parameters and reference runs now last weeks. This has matured the feedback scheme into a very usable tool for initial preparation of ultracold clouds for further experiments. As a very concrete example, the investigations of fluctuations covered in Chapter 6 relies on the correlation of N and T induced by the evaporative cooling. These correlations are only revealed due the the stabilised preparation.

OBSERVATION OF FLUCTUATIONS IN BOSE-EINSTEIN CONDENSATES

The condensate fraction of a BEC corresponds to the first moment of the distribution function for the ground-state occupation and was one of the first properties of Bose-Einstein condensation to be studied [20]. The atom number fluctuations of a BEC correspond to the second moment of the distribution, and this chapter is dedicated to the first ever experimental investigation of these fluctuations. The chapter opens with a discussion of the challenges related to performing such experiments, followed by a detailed account of the experimental methods and the analysis used to observe the fluctuations of a BEC.

6.1 Background

In Section 2.3 an overview of the long list of theoretical work on the fluctuations of the BEC was given. With the large interest from a theoretical point of view, the unusual statistical properties of degenerate Bose-gases and the unanswered questions related to the fluctuations of the interacting BEC, it may appear surprising that there has never been experimental studies of the fluctuations in atomic BECs. To date, the studies are limited to measurement of the statistics of the total atom number in degenerate Bose gases, where sub-Poissonian fluctuations were observed [105]. In photon-BECs the fluctuations were investigated under grand-canonical conditions [54].

The basic experiment for measuring fluctuations is simple; A series of clouds with constant atom number N and temperature T is prepared, which determines the average condensate atom number $\langle N_0 \rangle$. The sample variance ΔN_0^2 of N_0 is then the estimate of the fluctuations. However, under typical experimental conditions, N and T varies between experimental realisations, which leads to variation in $\langle N_0 \rangle$ that will shroud the fluctuations.

To estimate the stability requirement of the experiment, we can make a simple argument based on Eq. (2.25) (see also Fig. 2.3). Close to $T/T_c \sim 1$, the fluctuations are expected to be on the order of $\Delta N_0 \sim \sqrt{N}$. For a total atom number of $N = 1 \times 10^5$, this suggests that the standard deviation of N_0 must be measured at the level of $\Delta N_0 \sim 316$. This imposes a limitation on the acceptable variation in N and T , which can be estimated using the simple expression for the condensate fraction Eq. (2.7) and T_c Eq. (2.6). Combining these expressions, N_0 is given by

$$N_0 = N - KT^3, \tag{6.1}$$

with $K = (k_B/\hbar\bar{\omega})^3\zeta(3)$. To first order, the change in N_0 when N and T

vary is

$$\Delta N_0 = \frac{\partial N_0}{\partial N} \Delta N + \frac{\partial N_0}{\partial T} \Delta T = \Delta N - 3KT^2 \Delta T. \quad (6.2)$$

Using that $3KT^2 = 3(N - N_0)/T \approx 3N/T$ for $N \gg N_0$, which is valid close to $T = T_c$, the change in N_0 becomes

$$\Delta N_0 \sim N \left(\frac{\Delta N}{N} - 3 \frac{\Delta T}{T} \right). \quad (6.3)$$

Thus, for $N = 1 \times 10^5$, the relative variation in N must be below $\Delta N/N < 0.3\%$ and $\Delta T/T < 0.1\%$.

Typical ultracold quantum gas experiments are not able to meet these requirements, as the sequential preparation steps are all prone to technical fluctuations, and the final stability of N_0 can easily be on the order of 10%. One option would be to post select data with similar N and T , but this places strict requirements on the precision of both atom number and temperature determination, as well as vastly increases the required amount of data. Instead of post selection, our stabilisation technique presented in Chapter 5 puts us in a unique position to investigate the fluctuations of pre-stabilised ultracold clouds.

The most direct way of measuring the fluctuations is using a non-destructive technique to probe the same cloud in-trap, and determine the condensate atom number. However, our imaging resolution of the Faraday system does not allow for this approach. The experiment presented in the following sections is therefore based on repeated preparation of ultracold atom clouds and probing using destructive resonance absorption imaging after expansion during TOF.

6.2 Experimental procedure

The experimental procedure is illustrated in Fig. 6.1. We prepare thermal clouds as outlined in Chapter 3. When the clouds contain $\sim 4 \times 10^6$ atoms

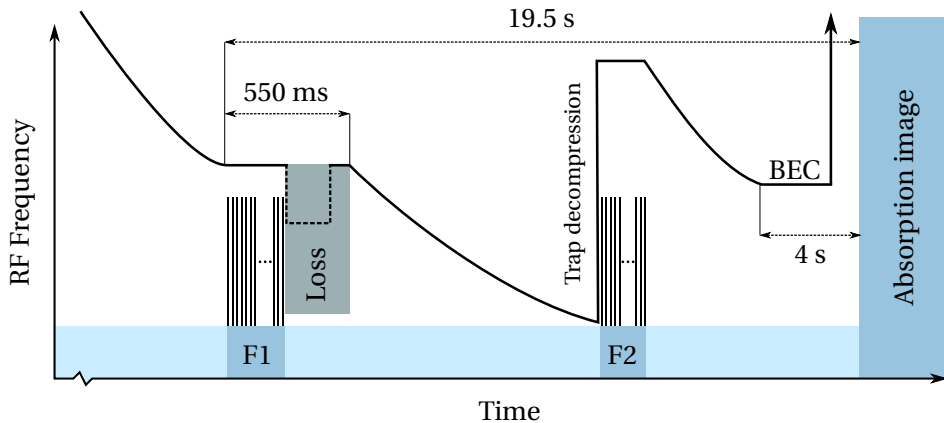


Figure 6.1: Schematic illustration of the final part of an experimental procedure for observing the atom number fluctuations of a BEC. F1 and F2 indicate the periods where Faraday imaging is employed. During the application on RF loss for the stabilisation, the RF frequency and power is transiently lowered to spill atoms. Adapted from [106].

at a temperature of $\sim 14\mu\text{K}$, the RF evaporation is interrupted to stabilise the preparation using the Faraday feedback method presented in Chapter 5. 50 Faraday images blue detuned from the $|F = 2\rangle$ to $|F' = 3\rangle$ transition by 799 MHz with a total pulse duration of 17.75 ms are acquired at the first imaging series F1, and subsequently a variable loss is induced. The amount of loss is determined by the Faraday measurement. The evaporation then proceeds until a temperature just above condensation is achieved.

Just before the second imaging series, the trap is decompressed. This is achieved by increasing the bias magnetic field by 6.9 G in the axial direction using a set of shim-coils in Helmholtz configuration. The axial trapping frequency is almost unchanged and is $\omega_z = 2\pi \times 17.7\text{ Hz}$, but the

radial frequency decreases from $\omega_\rho \sim 2\pi \times 300 \text{ Hz}$ to $\omega_\rho = 2\pi \times 96.4 \text{ Hz}$. This reduces the occurrence of phase fluctuations of the condensate that leads to density modulations of the condensate visible as stripes in the column density images [107]. The striping makes the fitting of condensate profiles less reliable, but as described later in Section 6.3, we analyse the images without relying on fits to the condensate profile. Any striping will therefore have a minimal influence on the analysis.

The decompression raises the trap bottom, and the RF knife is raised correspondingly. The bias field is ramped slowly in 2 s to avoid inducing oscillations of the cloud. After decompression a second set of 20 Faraday images with a total pulse duration of 10 ms is acquired at F2. These images are used to adjust the feedback coefficients and verify that the stabilisation was successful.

After F2 the cloud is cooled by the last evaporation ramp. By adjusting the final frequency of the RF knife we can select the temperature and condensate fraction of the cloud. The clouds are held in the trap for 4 seconds with the RF knife in place for the first 3 seconds to ensure that the clouds are in thermal equilibrium. The trap is turned off and the cloud is allowed to expand in time-of-flight for 27.5 ms before being probed with resonant absorption imaging. To avoid smearing of the cloud, a short imaging pulse of 25 μs is used. The imaging intensity is fairly high $I = 2.3 I_{\text{sat}}$ to accurately measure optically dense BECs.

For each value of the final RF frequency we repeat the sequence 60 times. Occasionally, the initial load of atoms is either too high or low for the feedback stabilisation to be effective. This can occur if the initial atom number is outside the range of the stabilisation reference (see Chapter 5). These runs are removed from the datasets, which therefore contains 45 - 60 experimental realisations each. In total, we have collected more than 3000 experimental realisations for the fluctuations investigations presented in this chapter.

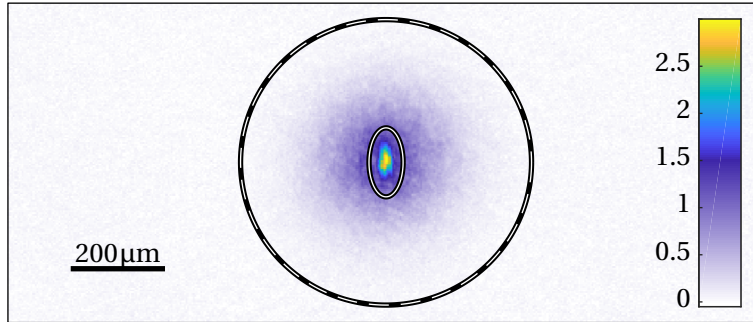


Figure 6.2: A sample image of a partly condensed BEC shown in optical density. Two ROIs are indicated, the outer (dashed) containing the entire cloud, and the inner (solid) enclosing the BEC. Adapted from [106].

6.3 Image analysis

The absorption images are the primary raw data and the column densities are evaluated as described in Section 3.3. To extract the relevant parameters, the images are evaluated in a two-step procedure. First, the optical density is fitted with a thermal distribution (Eq. (A.3)) in a ring-shaped ROI that excludes the BEC as shown in Fig. 6.2. The fit yields the thermal atom number and the temperature of the sample. The fitted density is subtracted from the total optical density, and the BEC atom number N_0 is determined by a simple summation of the density in each pixel in the inner ROI containing the BEC. The total atom number N is obtained by summation of the density in the region containing the entire cloud.

The determination of the ROIs deserves special attention. The images are first fitted individually, by creating ROIs based on a fit of a bimodal model to slices through the centre of the clouds. These are used to make initial guesses for 2D fit to the entire image as outlined above. From these we obtain the widths of the thermal profiles and the condensates. We then choose a final BEC ROI that encompass the largest BECs with a

margin of 20 % of the Thomas-Fermi radius. This ensures that potential edge effects at the boundary between the condensate and the thermal cloud does not influence the thermal density profile fit [80], and that small changes of the cloud position do not make the BEC extend outside the ROI. The thermal ROI is adjusted to encompass the entire cloud by correlating the total atom number and the cloud widths. In total, each image is fitted once with a bimodal model to slices of the images, and twice with 2D fits.

The advantage of this procedure is twofold. First, we can evaluate the fluctuations in exactly the same manner for partially condensed and thermal clouds, since the BEC ROI is fixed. Secondly, each pixel included in the summation when integrating the measured densities adds noise to the measurement. To minimize this, and to avoid that it varies due to variations in the ROI sizes, it is important to keep the ROI size constant.

6.4 Correlations revealed by feedback stabilisation

The feedback stabilisation provides reproducible starting conditions for the experiments. In the experiment we measure and stabilise to the Faraday signal, which depends on both N and T through $\Sigma_S \propto N^2/T$ (see Chapter 4), and a stable signal is thus not equivalent to simultaneously stable N and T . This was the case for the previous work on feedback stabilisation, see e.g. Fig. 5.6. In the previous work, application of loss pulses led to significant cooling of the sample. To remedy this, the frequency of the loss pulses is now adjusted to remove atoms at the mean energy of the sample as outlined in Section 5.4.1. This mitigates the influence of the loss pulses on the sample temperature. Additionally, the evaporation between the two imaging series at F1 and F2 ensures, that a stable Faraday signal implies stable atom number and temperature.

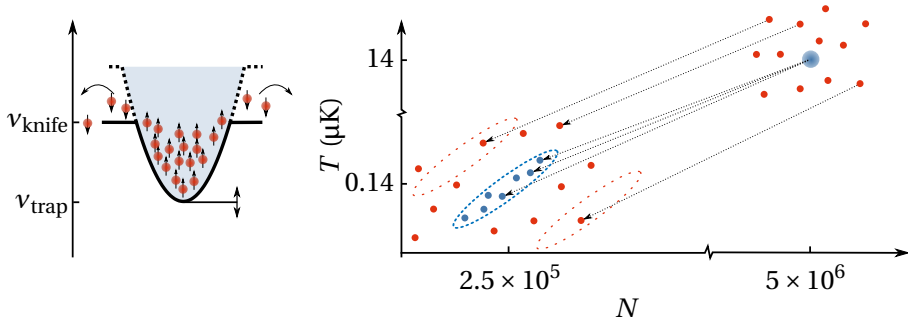


Figure 6.3: Right: An illustration of evaporative cooling, where the trap depth is set by the RF knife and the trap bottom. Left: Evaporative cooling reveals the correlated variation of the atom number and temperature when the final trap depth varies (\bullet). However, if there is an initial spread in atom number and temperature, the correlations get buried (\bullet).

Despite the stabilisation we still observe variation of the final atom number and temperature of the final clouds, which originates from variations in the depth of trap at low temperatures. The trap depth is determined by the frequency of the RF knife ν_{knife} and the trap bottom ν_{trap} , which corresponds to the frequency resonant with the trap center. The RF knife frequency is generated by a DDS function generator and is very well defined, but the trap bottom is prone to drifts. Possible sources are changes of the cooling water temperature for the magnetic trap, or small variations of the external background magnetic field. This induces correlated variations in N and T ; if the trap is shallower, we effectively evaporate further, reducing the atom number and temperature, and vice versa, when the trap is deeper, in contains more atoms at a higher temperature.

The situation is illustrated in Fig. 6.3. Starting with a well-defined initial atom number and temperature, the evaporative cooling process leads to samples with varying but highly correlated atom numbers and temper-

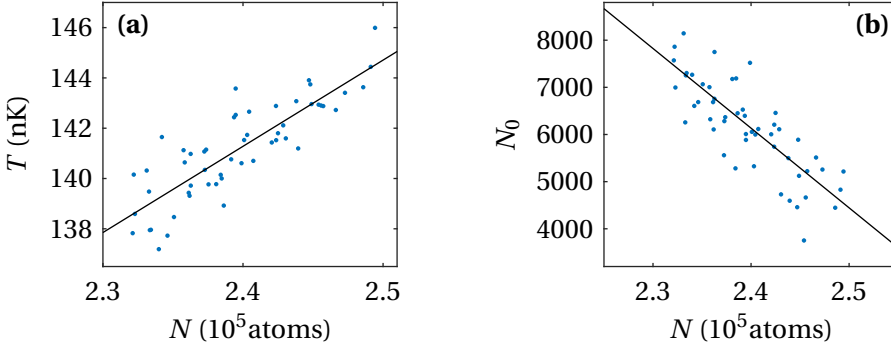


Figure 6.4: Observed correlations between **(a)** N and T and **(b)** N and N_0 for a single value of the final RF knife frequency. A linear fit is applied to the data.

atures. However, if the initial atom number and temperature fluctuate, the correlation gets shrouded in the scatter. The stabilisation provides the required conditions for the correlations to be observable. Figure 6.4(a) shows the observed correlation between the N and T and Fig. 6.4(b) the corresponding correlation between N and N_0 . The correlations reduce the dimensionality of the problem, since both T and N_0 are essentially determined by the total atom number. By utilising the correlations, we can overcome the problem of precisely determining both N , N_0 and T , which is required to measure the condensate fraction.

6.5 Condensate fraction

The condensed fraction of a partially condensed cloud is determined by the total atom number N and the temperature T . To compare our data to theory we must determine both N , N_0 and T with great precision. Figure 6.5(a) shows the condensate fraction for each individual experi-

6. OBSERVATION OF FLUCTUATIONS IN BOSE-EINSTEIN CONDENSATES

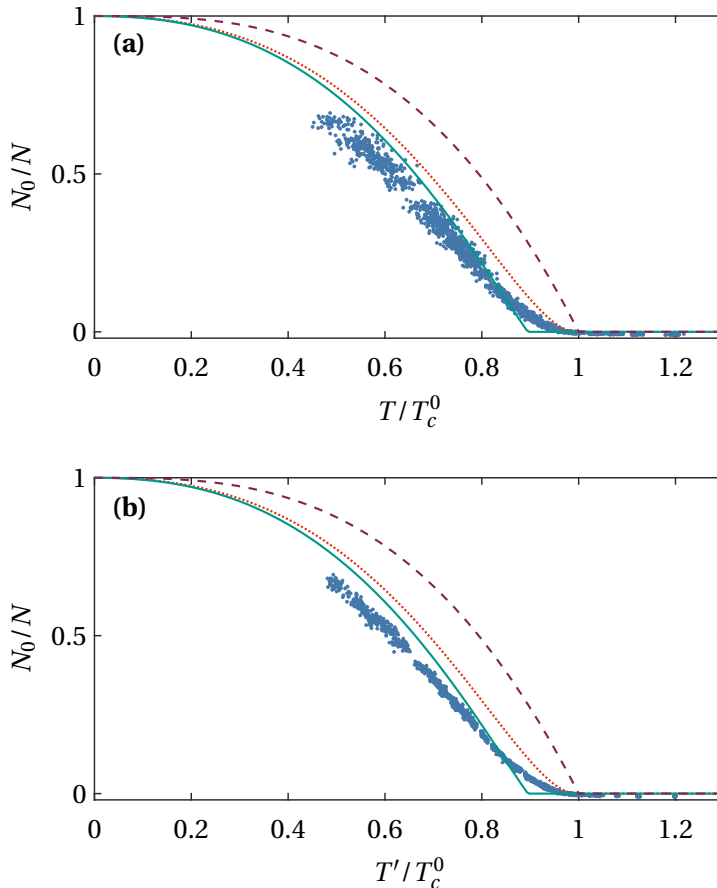


Figure 6.5: Comparison of measurements of the condensate fraction. In **(a)**, the temperature is inferred from the fit to the density profiles for each individual image. In **(b)**, the temperature is determined by the fitted correlation between atom number and temperature, as shown in Fig. 6.4. The resolution of the condensate fraction is increased by taking advantage of the correlation of N and T . The data (\bullet) is compared to the ideal prediction given by Eq. (2.7) (---), the condensate fraction including the finite size and interaction effects given by Eqs. (2.10) and (2.23) (—) and the semi-ideal model [78] (⋯).

mental realisation as a function of the reduced temperature T/T_c , where the parameters are determined as outlined in Section 6.3. T_c is calculated individually for every data point. The spread indicates the uncertainty of the measurement.

When the temperature is lowered, the extension of the thermal wings shrinks. As the size of the thermal component becomes comparable to the condensate size, the proper distinction between the thermal component and the condensate becomes difficult. This is particular problematic when determining the temperature, as the model fitting of the recorded density profiles is uncertain when the size of the condensate is similar to the size the of thermal component. The measurements cover the range $0.5T_c < T < 1.2T_c$. Below $T/T_c = 0.5$ we are no longer able to properly distinguish the two components and are therefore unable to determine the temperature.

The correlation between N and T allows for a more precise determination of the temperature. By fitting the correlation in Fig. 6.4(a) with a linear fit, we can obtain an adjusted temperature T' from the fit. A linear fit is chosen as a conservative choice that avoids overfitting the data. Note that the data range corresponds to a very small interval in N and T of the entire data . This method reduces the uncertainty from the individual temperature fits, since all temperature data in each narrow interval is taken into account, and T' can take advantage of the high precision of atom number determination. Figure 6.5(b) shows N_0/N vs T'/T_c . The spread is clearly reduced at all temperatures $T' < T_c$, highlighting the high precision of the method, which is a prerequisite for the study of fluctuations.

The data is compared to three theoretical predictions, namely the ideal gas result of Eq. (2.7), the same expression including the corrections due to the finite size effects and interactions in Eqs. (2.10) and (2.23), and finally the semi-ideal model, that takes the repulsion of the thermal cloud by the BEC into account, but neglects the corresponding repulsion of the BEC by the thermal cloud in Eq. (2.18) [78, see also Section 2.4].

The experimental data shows a clear reduction of the critical temperature relative to the ideal gas prediction, and the correspondence with the two other models is much better. Only the semi-ideal model captures the observed smooth onset of the BEC fraction. At $T < 0.95 T_c$ there is a systematic difference between the data and the models, with the data showing a lower condensate fraction (or equivalently a lower temperature). This is expected due to the choice of fitting model. In Section 2.4 it was shown that fitting Eq. (A.3), where the chemical potential has been set to $\mu = 0$, to the more accurate semi-ideal model underestimates the temperature by 5% to 10%. This explains the observed discrepancy well.

Above $T/T_c > 1$, we systematically observe a ‘negative’ BEC fraction. This is an artefact of the two-step evaluation, where the fitted thermal density is subtracted from the observed density. Since we use a fitting model with $\mu = 0$, the profile overestimates the central density slightly when the fitted region excludes the centre of the cloud.

6.6 Observation of fluctuations

To determine the condensate atom number fluctuations we again use the correlations revealed by the stabilisation. A linear fit is applied to the N_0 vs. N correlation of each dataset of 45 to 60 points as shown in Fig. 6.4(b). The fluctuations are estimated from the sample variance with respect to the fit

$$\Delta N_0^2 = \frac{1}{n-1} \sum_{i=1}^n (N_{0,i} - N_{\text{fit},i})^2, \quad (6.4)$$

where $N_{\text{fit},i}$ is the condensate atom number determined by the fitted correlation at the total atom number corresponding to point i , and n is the number of runs in the dataset.

Figure 6.6 shows the variance of N_0 in each dataset as a function of the reduced temperature T/T_c . T and T_c are the average temperature and average critical temperature of an ideal gas across each dataset. Error

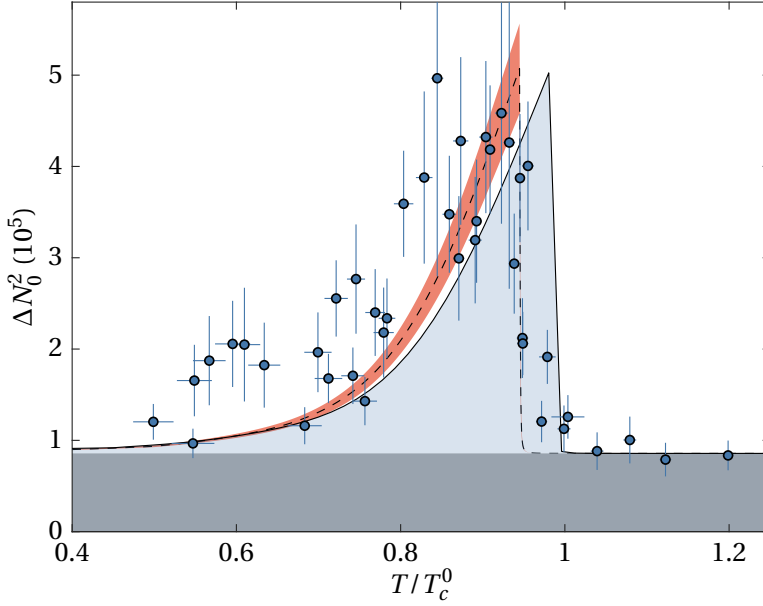


Figure 6.6: Comparison with the measured variance of N_0 with theory. ● Experimentally measured variance. The errorbars are 1σ statistical uncertainties. — Exact canonical calculations of the fluctuations of a non-interacting gas, offset by the variance estimated from the points at $T > T_c$. - - - Fitted model based on non-interacting approximations of the fluctuations, see Eq. (6.5). The shaded band is a 1σ confidence bound of the fit. ■ Offset determined by the average variance for points at $T > T_c$. The offset is assumed constant and added to the theory calculation and the model fit.

bars are 1σ statistical uncertainties on the variance without assumption of the underlying distribution [108, 109]. The rapid growth of the variance as the critical temperature is crossed from above is a clear signature of the fluctuations. The variance decreases below T_c due to the decreasing temperature and atom number.

Above T_c the variance does not completely vanish. Since the evaluation of the thermal clouds is identical to the condensates below T_c despite the absence of a BEC, we attribute this to an offset due to technical fluctuations (see Section 6.6.1 for a discussion of the origin of these). The offset is determined by averaging the datapoints at $T/T_c > 1$ to $\mathcal{O} = 0.85(9) \times 10^5$. We assume this can be regarded as a constant lower detection limit for our measurements.

As discussed in Section 2.3, the full theoretical description of the trapped weakly interacting Bose-gas is an outstanding challenge, and a complete comparison with theory is not possible. Therefore, the data is compared to theory in two ways. First, the fluctuations are calculated exactly within the canonical ensemble for a non-interacting gas in an anisotropic harmonic trap with our trapping frequencies, and with N and T adjusted to match our measurements [40]¹. To account for technical contributions, the constant offset \mathcal{O} is added to the calculations. This shows good agreement with the data. The sudden increase in variance at the critical temperature is consistent, and the magnitude of the observed fluctuations at the peak matches the peak value of theory. However, the observed peak is shifted with respect to the theory. This is expected due to the lowering of the critical temperature due to interactions in Eq. (2.22), which the exact calculation naturally does not take into account. A similar shift was observed in the recent theoretical work of [71]. The good agreement shows that we have observed the fluctuations in a BEC.

The data shows a small apparent peak at temperatures in the vicinity

¹The calculations was done by Krzysztof Pawłowski and Kazimierz Rzążewski at the Center for Theoretical Physics of the Polish Academy of Sciences.

of $T/T_c \sim 0.6$, where five points show systematically larger variance. The five points were acquired three weeks after the rest of the dataset. The most likely explanation of the apparent peak is that the stability of the experiment was worse, leading to a worse resolution of the correlations in Fig. 6.4. This will be seen as a systematically larger variance. Hence, we do not assign any physical significance to the feature.

To extract more quantitative results, the data is fitted with a model inspired by the limiting non-interacting theories in Fig. 2.3. Below T_c , the model corresponds to Eq. (2.25) with a free scaling α , while above T_c the GCE Eq. (2.24) result is used. Above T_c , N_0 is calculated analytically for the fit based on the analytical approximation given in [39]. In the fitting model we allow for a shift of the critical temperature δt . The lower value of these two expressions is used, and the fitted expression is thus

$$\Delta N_0^2 = \min \begin{cases} \alpha N \left(\frac{T}{T_c} + \delta t \right)^3 + \mathcal{O} \\ N_0(N_0 + 1) + \mathcal{O}. \end{cases} \quad (6.5)$$

The fitted curve is show in Fig. 6.6. The fitted parameters are $\alpha = 1.72(19)$ and $\delta t = -0.0429(3)$. The scaling α is larger than the asymptotic value $\zeta(2)/\zeta(3) \approx 1.36$, which is consistent with the enhancement of the fluctuations due to anisotropy of the trapping potential in Fig. 2.4. From the fit, the rise in fluctuations at the phase transition excluding the offset is determined to be $\Delta N_{0,\max}^2 = 4.2(8) \times 10^5$ at a total atom number of $N_{\max} = 2.5 \times 10^5$. This value is consistent with the exact non-interacting calculation, which yields a peak value of $\Delta N_{0,\max}^2 = 4.17 \times 10^5$. As discussed above, a negative temperature shift of the peak fluctuations is expected due to interactions. Using Eq. (2.22), the first order shift of the critical temperature is $T/T_c = -3.8\%$, which compares well with the measured shift $\delta t = -4.3\%$.

In Fig. 6.7 the fitted model is shown as a surface plot. This shows clearer that the decay of fluctuations is initially dominated by the decreasing atom number, in particular in the temperature range $0.8 < T/T_c < 1$.

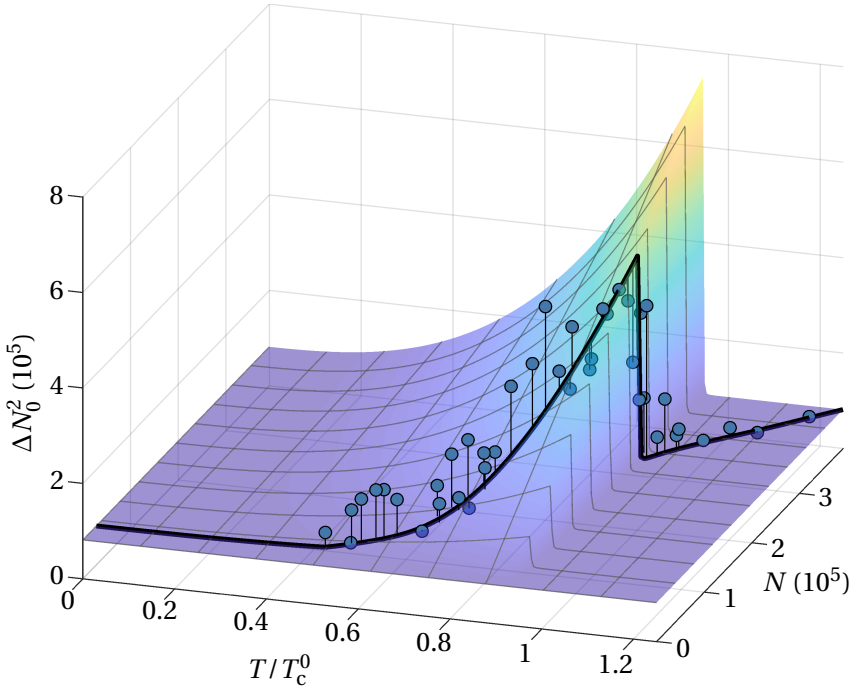


Figure 6.7: Surface plot of the fitted model Eq. (6.5). This illustrates that the decay of the fluctuations is both a consequence of the decreasing temperature and atom number, and that in particular the initial decay of the variance in the temperature range $T/T_c > 0.8$ is dominated by the decrease of N . (●) Experimentally measured variance. The stems connect the datapoints to the surface. (—) Evaluation of the fit Eq. (6.5) for atom number and temperature corresponding to the measurements.

At lower N and T the data quality is not sufficient to extract quantitative results. Consequently, the experimental approach presented does not currently allow us to investigate the low temperature scaling of the fluctuations with atom number discussed in Section 2.3.3.

6.6.1 Discussion of excess variance

The measurement of the variance of N_0 was presented with statistical errorbars in Fig. 6.6. The errorbars only concerns the statistical uncertainty of the variance estimate due to the finite sample sizes. Systematic uncertainties are not captured and further increase the variance. In this case, systematic uncertainties can be regarded as anything that contributes to the observed variance of the condensate atom number apart from the fundamental fluctuations, and here follows a brief discussion of the most important contributions.

Detection noise is an important contribution to the observed variance. Ideally, it is limited by the photon shot noise of the imaging, but technical camera noise such as read out noise contributes as well. A classical light noise contribution arise from fringing of the images if the imaging beam moves or changes between the shadow and reference images for absorption imaging, which we reduce by keeping the separation between the images as short as possible. A detailed description of the absorption imaging set-up was presented in Section 3.3.

Related to the detection noise is the fitting of the recorded density distributions. Though we do not directly use the fitted atom number and temperature for determining N_0 , we still subtract the fitted thermal density from the recorded density. Therefore, the fitting uncertainty will still have an influence on the determination of N_0 .

Both the detection noise and fitting noise are independent of whether we have a condensate present or not, and we assume that they are the origin of the bulk of the observed offset in the fluctuations. While there is likely a dependence on atom number, we do not have a method to determine this. Therefore, we choose to treat it as a constant offset across the entire range of data.

A separate effect that adds to the observed variance is drifts of the correlations in Fig. 6.4. If this is not constant in time, the distribution around the fitted lines will be broadened, increasing the observed variance. Drifts

of the correlations will arise if the external experimental conditions in the lab varies. This can be e.g. changes to the external background magnetic field or the cooling water of the magnetic trap. This effect is only relevant when the BEC is present, and is a contributing factor to the larger spread of the observed variance below T_c . Since the data is obtained sequentially for different evaporation levels, this can give a presumably false impression of features in the data, as is the case for the apparent peak at $T/T_c \sim 0.6$ in Fig. 6.6 previously discussed.

6.7 Supporting analysis

The previous sections presented the experiment and analysis leading to the main result presented in Fig. 6.6. This section presents investigations, that either support the findings in the previous sections or sheds light on the choices made during the experiments and analysis.

Model-free evaluation of fluctuations

The evaluation of the fluctuations includes the fitting of the idealized thermal distribution after time-of-flight given by Eq. (A.3). To estimate the effect of a different choice of fitting functions, the fluctuations can be estimated using the most naïve approach without assuming any fitting model. Instead, the total atom number in the inner ROI in Fig. 6.2 N_{center} is determined. This will overestimate N_0 , but the variance $\Delta N_{\text{center}}^2$ still corresponds to a measurement of condensate fluctuations. Figure 6.8 illustrates that this reproduces the same features. In particular, the growth of the variance at the transition is still clear.

Sample size considerations

The sample size of 60 runs per RF-setting was chosen to balance two requirements. On one hand we need a sufficiently large sample to es-

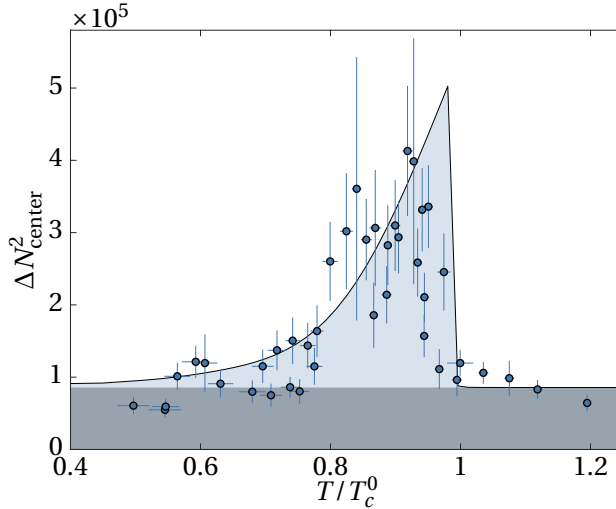


Figure 6.8: Estimate of the variance of N_{center} without any modelling of the density profile. The errorbars are 1σ statistical uncertainties. --- and --- are the exact canonical calculations of the fluctuations with the same offset as in Fig. 6.6.

estimate the variance and on the other hand it must be small enough, that changes of the external experimental conditions leading to drifts in the observed correlations discussed above are insignificant. By recording 610 consecutive runs at the same RF setting and varying the sample size when evaluating the fluctuations, 60 runs were found to be a good compromise. With a cycle time of 1 min 40 s, this corresponds to 100 min, similar to the observed time scales of the external cooling water temperature drifts.

6.8 Summary

In this chapter the measurement of the atom number fluctuations in a BEC was presented. The fluctuations reveal themselves as a sudden increase in the variance of the BEC atom number when a Bose-gas is cooled below the critical temperature for Bose-Einstein condensation. The experiment took advantage of the correlation N , N_0 and T , which were observable due to the feedback stabilised preparation scheme presented in Chapter 5. This allowed us to circumvent the problem that technical fluctuations typically dominate the fluctuations.

Since the theoretical description of the fluctuations at present is not able to fully account for interactions in trapped BEC, a full theoretical comparison was not possible. However, by comparing with non-interacting exact calculations, the measurements show that the interactions have a limited effect on the fluctuations.

CONCLUSION AND OUTLOOK

Within this thesis three main topics were covered, namely non-destructive detection of ultracold clouds based on the Faraday imaging, stabilised preparation of samples at the shot noise limit and the first experimental observation of the fluctuations of BECs.

In Chapter 4 the obtainable precision of Faraday imaging was experimentally characterised. It was demonstrated that a precision a factor of 2 below the standard shot noise level $1/\sqrt{N}$ is achievable. This precision is sufficient to use Faraday imaging in our feedback scheme, where the atom number is stabilised at or below the shot noise level.

Chapter 5 covered our implementation of feedback stabilised preparation of ultracold gases. The stabilisation scheme is based on detection of the initial atom number through Faraday imaging. The images are analysed in real-time on an FPGA, and excess atoms are discarded through RF cuts in the energy distribution. The obtainable performance of the

preparation scheme was characterised by measuring the degree of correlation between two Faraday measurements with a variable loss in-between. The observed fluctuations of the correlation can be accounted for by detection noise of the Faraday imaging and the stochastic nature of the loss. Through active control of the applied loss via a feedback algorithm implemented on the FPGA, stabilisation of the Faraday signal at the atom shot noise level was demonstrated.

Taking advantage of correlation between the atom number and the temperature revealed by the stabilised preparation, the first ever observation of the atom number fluctuations of BECs were made. The investigation of these fluctuations were presented in Chapter 6. There exist no theory that takes all aspects of the problem of calculating the fluctuations in interacting BECs into account. However, it was substantiated in Chapter 2 that the interactions only to a limited extent change the fluctuations in weakly interacting BECs. Therefore the observation was compared to an exact numerical calculation of the fluctuation in the non-interacting BEC. We found a good agreement between the maximal fluctuations of non-interacting theory and or measurements. The observed shift of the temperature at which the maximal fluctuations occur was attributed to the change of the critical temperature due to interactions.

The observation of the fluctuation of BECs is a concrete example of the value of precision preparation of ultracold gases. With a source of stable ultracold clouds, several interesting research questions presents themselves, of which a few examples are given below.

Precise measurements of temperature and condensate fraction

In Chapter 6 it was shown that the stabilised preparation led to increased precision of the condensate fraction. This was achieved by utilizing the correlation of N and T to reduce the uncertainty of the temperature fits. This holds the potential to make detailed test of models of the condensate

fraction. The new Bragg diffraction set-up can further complement this, as was the case in earlier studies [21].

This study will be augmented with the development of better models of the TOF expansion of partially condensed clouds. The numerical expansion of the semi-ideal model in Chapter 2 demonstrated a discrepancy between typically fitting models and the cloud profile in TOF. With a stabilised source of ultracold clouds we have the ideal setting for testing more accurate models, which will lead to better determination of temperature of ultracold clouds.

Anomalous fluctuations of BECs

The reported observation of the atom number fluctuations of BECs does not answer all the outstanding questions regarding the nature of these fluctuations. Perhaps the most straight forward extension of the reported experiments is a study of the scaling of the fluctuations with atom number. As discussed in Chapter 2, there has been a controversy concerning whether the fluctuations exhibit anomalous scaling $\Delta N_0^2 \propto N^\gamma$ with $\gamma > 1$. Figure 7.1 illustrates the expected difference in peak fluctuations between normal and anomalous scaling. While we could not determine whether $\gamma \neq 1$ from the data at hand, the experimental approach can be adapted to favour such a study. By measuring just the peak fluctuations as the atom number is varied, we can potentially rule out the anomalous fluctuations at higher atom numbers at finite temperatures.

The higher moments of the BEC distribution

The observed atom number fluctuations of BECs correspond to second moment or variance of the distribution function for the BEC. A further development of our methods may open up for investigations of the higher moments, which are expected to be non-gaussian [39]. Presently, we have

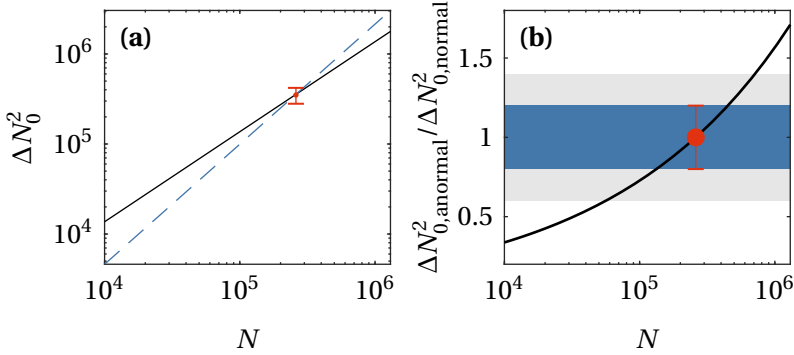


Figure 7.1: Comparison of the predicted fluctuations with normal and anomalous scaling. **(a)** The asymptotic fluctuations given by Eq. (2.25) at $T/T_c = 1$ with normal scaling $\Delta N_0^2 \propto N$ (—) and anomalous scaling $\Delta N_0^2 \propto N^{4/3}$ (- - -). The prefactor of the anomalous fluctuations are chosen to yield the value measured in the experiment (●). **(b)** Ratio of the anomalous to normally scaling predictions (—). The point again indicates our measurement (●). The bands ■ and ■ are 1σ and 95% confidence bounds on the peak fluctuation estimate.

so far not been able to reliably extract higher moments from the recorded data.

Feedback stabilisation version 2.0

The feedback stabilisation based on non-destructive Faraday detection is already an invaluable tool for our experiments, but exiting options for improving the method are available. Currently the limitation of the stabilisation is the stochastic nature of the induced loss. Consequently, a smaller loss will lead to better performance. This can be readily achieved by using a two-step or multi-step stabilisation scheme, where the final corrections are small.

One might also consider using the destructiveness of the Faraday imaging as the tool for the final corrections. This will make the stabilisation limited only by the precision of the detection, which were shown in Chapter 4 to be a factor of two below the standard shot noise level. In practice this can be achieved by implementing a Kalman filter on the FPGA, which will take our understanding of the the imaging, loss mechanisms and evaporative cooling into account, and stop the Final imaging sequence when the desired atom number is obtained.

A direction so far unexplored is using the FPGA to monitor in-trap motion. This information is however already available from the analysis of images on the FPGA. By reducing the frame size, the frame rate of the imaging can be significantly increased, which will make it possible to track fast motion. By controlling trap parameters through the external bias fields, the FPGA can be used to stabilise or drive oscillations or non-harmonic motion.

Appendix A

Integrated density profiles

When imaging ultracold atom clouds with optical methods, the resulting images probe the column densities of the density distributions. To fit the recorded images, we thus need to integrate the 3D density distributions given in Section 2.4 along the line of sight.

Thomas-Fermi density profile

The column density of a BEC described by the Thomas-Fermi profile is obtained by integration of Eq. (2.28) along z from $-z_0$ to z_0 , where $z_0^2 = R_z^2 \left(1 - \frac{x^2}{R_x^2} - \frac{y^2}{R_y^2}\right)$, the resulting column density being

$$\tilde{n}_c(x, y) \frac{5}{2\pi} \frac{N_0}{R_x R_y} \max\left(0, \left(1 - \frac{x^2}{R_x^2} - \frac{y^2}{R_y^2}\right)^{3/2}\right) \quad (\text{A.1})$$

Often it's convenient to integrate the recorded column densities along one direction, in which case we integrate Eq. (A.1) once more to obtain

$$n_c^{\text{1D}}(x) = \frac{15}{16} \frac{N_0}{R_x} \max\left(0, \left(1 - \frac{x^2}{R_x^2}\right)^2\right). \quad (\text{A.2})$$

Low temperature thermal density profiles

The column density of a cold thermal cloud is given by the integral of Eq. (2.37)

$$\tilde{n}_{\text{th}}(x, y) = \frac{N_{\text{th}}}{2\pi w_x w_y g_3(\tilde{z})} g_2\left(\tilde{z} e^{-x^2/2w_x - y^2/2w_y}\right). \quad (\text{A.3})$$

By integrating once more the resulting line density is

$$\tilde{n}_{\text{th}}^{1\text{D}}(x) = \frac{N_{\text{th}}}{\sqrt{2\pi} w_x g_3(\tilde{z})} g_{5/2}\left(\tilde{z} e^{-x^2/2w_x - y^2/2w_y}\right). \quad (\text{A.4})$$

At or below the critical temperature, the chemical potential will be limited to $\mu = 0 \implies \tilde{z} = \exp(\mu/k_B T) = 1$. Then $g_3(1) = \zeta(3) \approx 1.20$, where $\zeta(x)$ is the Riemann Zeta function.

High temperature thermal density profiles

At high temperatures the thermal density is given by Eq. (2.34). Integration along z yields the column density

$$\tilde{n}_{\text{th}}^{\text{MB}}(x, y) = \frac{N_{\text{th}}}{2\pi w_x w_y} e^{-x^2/2w_x^2 - y^2/2w_y^2}, \quad (\text{A.5})$$

and integrating once more along y yields the line density

$$\tilde{n}_{\text{th}}^{\text{MB}}(x, y) = \frac{N_{\text{th}}}{\sqrt{2\pi} w_x} e^{-x^2/2w_x^2}. \quad (\text{A.6})$$

BIBLIOGRAPHY

- [1] M. Planck, Zur Theori des Gesetzes der Energieverteilung im Normalspectrum, Verhandl. Dtsch. phys. Ges **2**, 237 (1900).
- [2] A. Einstein, Über einen die Erzeugung und Verwandlung des Lichtes betreffenden heuristischen Gesichtspunkt, Ann. Phys. **322**, 132–148 (1905).
- [3] N. Bohr, On the constitution of atoms and molecules, Philos. Mag. **26**, 476–502 (1913).
- [4] J. P. Dowling and G. J. Milburn, Quantum technology: the second quantum revolution, Philos. Trans. Roy. Soc. London **361**, 1655–1674 (2003).
- [5] A. de Touzalin, C. Marcus, F. Heijman, I. Cirac, R. Murray and T. Calarco, *Quantum manifesto*, (18th May 2016) <http://quope.eu/manifesto>.
- [6] R. Blatt and C. F. Roos, Quantum simulations with trapped ions, Nat. Phys. **8**, 277–284 (2012).
- [7] S. Schmidt and J. Koch, Circuit QED lattices: towards quantum simulation with superconducting circuits, Ann. Phys. **525**, 395–412 (2013).
- [8] A. Aspuru-Guzik and P. Walther, Photonic quantum simulators, Nat. Phys. **8**, 285–291 (2012).

- [9] M. Saffman, Quantum computing with atomic qubits and Rydberg interactions: progress and challenges, *J. Phys. B: At., Mol. Opt. Phys.* **49**, 202001 (2016).
- [10] Bose, Plancks Gesetz und Lichtquantenhypothese, *Zeitschrift für Physik* **26**, 178–181 ().
- [11] A. Einstein, Quantentheorie des einatomigen idealen Gases, in *Albert Einstein: Akademie-Vorträge*, Vol. 6 (Wiley-VCH Verlag GmbH & Co. KGaA, Weinheim, FRG, Sept. 1924), pp. 237–244.
- [12] M. H. Anderson, J. R. Ensher, M. R. Matthews, C. E. Wieman and E. A. Cornell, Observation of Bose-Einstein condensation in a dilute atomic vapor, *Science* **269**, 198–201 (1995).
- [13] K. B. Davis, M. -.-O. Mewes, M. R. Andrews, N. J. van Druten, D. S. Durfee, D. M. Kurn and W. Ketterle, Bose-Einstein condensation in a gas of sodium atoms, *Phys. Rev. Lett.* **75**, 3969–3973 (1995).
- [14] C. C. Bradley, C. A. Sackett, J. J. Tollett and R. G. Hulet, Evidence of Bose-Einstein condensation in an atomic gas with attractive interactions, *Phys. Rev. Lett.* **75**, 1687–1690 (1995).
- [15] B. DeMarco and D. S. Jin, Onset of Fermi degeneracy in a trapped atomic gas, *Science* **285**, 1703–1706 (1999).
- [16] C. Chin, R. Grimm, P. Julienne and E. Tiesinga, Feshbach resonances in ultracold gases, *Rev. Mod. Phys.* **82**, 1225–1286 (2010).
- [17] G. Modugno, M. Modugno, F. Riboli, G. Roati and M. Inguscio, Two atomic species superfluid, *Phys. Rev. Lett.* **89**, 190404 (2002).
- [18] L. Wacker, N. B. Jørgensen, D. Birkmose, R. Horchani, W. Ertmer, C. Klempt, N. Winter, J. Sherson and J. J. Arlt, Tunable dual-species Bose-Einstein condensates of ^{39}K and ^{87}Rb , *Phys. Rev. A* **92**, 053602 (2015).
- [19] I. Bloch, J. Dalibard and S. Nascimbène, Quantum simulations with ultracold quantum gases, *Nat. Phys.* **8**, 267–276 (2012).

- [20] J. R. Ensher, D. S. Jin, M. R. Matthews, C. E. Wieman and E. A. Cornell, Bose-Einstein condensation in a dilute gas: measurement of energy and ground-state occupation, *Phys. Rev. Lett.* **77**, 4984–4987 (1996).
- [21] F. Gerbier, J. H. Thywissen, S. Richard, M. Hugbart, P. Bouyer and A. Aspect, Experimental study of the thermodynamics of an interacting trapped Bose-Einstein condensed gas, *Phys. Rev. A* **70**, 013607 (2004).
- [22] R. Meppelink, R. A. Rozendaal, S. B. Koller, J. M. Vogels and P. van der Straten, Thermodynamics of Bose-Einstein-condensed clouds using phase-contrast imaging, *Phys. Rev. A* **81**, 053632 (2010).
- [23] M. R. Andrews, M.-O. Mewes, N. J. van Druten, D. S. Durfee, D. M. Kurn and W. Ketterle, Direct, nondestructive observation of a Bose condensate, *Science* **273**, 84–87 (1996).
- [24] M. R. Andrews, D. M. Kurn, H.-J. Miesner, D. S. Durfee, C. G. Townsend, S. Inouye and W. Ketterle, Propagation of sound in a Bose-Einstein condensate, *Phys. Rev. Lett.* **79**, 553–556 (1997).
- [25] C. C. Bradley, C. A. Sackett and R. G. Hulet, Bose-Einstein condensation of lithium: observation of limited condensate number, *Phys. Rev. Lett.* **78**, 985–989 (1997).
- [26] H.-J. Miesner, M. R. Stamper-Kurn Dan M. anMiesner, D. S. Durfee, S. Inouye and W. Ketterle, Bosonic stimulation in the formation of a Bose-Einstein condensate, *Science (New York, N.Y.)* **279**, 1005–7 (1998).
- [27] L. D. Turner, K. F. E. M. Domen and R. E. Scholten, Diffraction-contrast imaging of cold atoms, *Phys. Rev. A* **72**, 031403 (2005).

- [28] A. Ramanathan, S. R. Muniz, K. C. Wright, R. P. Anderson, W. D. Phillips, K. Helmerson and G. K. Campbell, Partial-transfer absorption imaging: a versatile technique for optimal imaging of ultracold gases, *Rev. Sci. Instrum.* **83**, 083119 (2012).
- [29] F. Kaminski, N. Kampel, M. Steenstrup, A. Griesmaier, E. Polzik and J. Müller, In-situ dual-port polarization contrast imaging of Faraday rotation in a high optical depth ultracold 87Rb atomic ensemble, *Eur. Phys. J. D* **66**, 1–8 (2012).
- [30] P. B. Wigley, P. J. Everitt, K. S. Hardman, M. R. Hush, C. H. Wei, M. A. Sooriyabandara, P. Manju, J. D. Close, N. P. Robins and C. C. N. Kuhn, Non-destructive shadowgraph imaging of ultra-cold atoms, *Opt. Lett.* **41**, 4795–4798 (2016).
- [31] M. Gajdacz, P. L. Pedersen, T. Mørch, A. J. Hilliard, J. Arlt and J. F. Sherson, Non-destructive Faraday imaging of dynamically controlled ultracold atoms, *Rev. Sci. Instrum.* **84**, 083105 (2013).
- [32] M. A. Kristensen, M. Gajdacz, P. L. Pedersen, C. Klempt, J. F. Sherson, J. J. Arlt and A. J. Hilliard, Sub-atom shot noise Faraday imaging of ultracold atom clouds, *J. Phys. B: At., Mol. Opt. Phys.* **50**, 034004 (2017).
- [33] B. J. Sawyer, A. B. Deb, T. McKellar and N. Kjærgaard, Reducing number fluctuations of ultracold atomic gases via dispersive interrogation, *Phys. Rev. A* **86**, 065401 (2012).
- [34] M. G. Bason, R. Heck, M. Napolitano, O. Eliasson, R. Müller, A. Thorsen, W.-Z. Zhang, J. Arlt and J. F. Sherson, Measurement-enhanced determination of BEC phase transitions, *J. Phys. B: At., Mol. Opt. Phys.* (2018).
- [35] M. Gajdacz, A. J. Hilliard, M. A. Kristensen, P. L. Pedersen, C. Klempt, J. J. Arlt and J. F. Sherson, Preparation of ultracold atom clouds at the shot noise level, *Phys. Rev. Lett.* **117**, 073604 (2016).

- [36] A. D. Ludlow, M. M. Boyd, J. Ye, E. Peik and P. O. Schmidt, Optical atomic clocks, *Rev. Mod. Phys.* **87**, 637–701 (2015).
- [37] S. S. Szigeti, M. R. Hush, A. R. R. Carvalho and J. J. Hope, Feedback control of an interacting Bose-Einstein condensate using phase-contrast imaging, *Phys. Rev. A* **82**, 043632 (2010).
- [38] R. M. Ziff, G. E. Uhlenbeck and M. Kac, The ideal Bose-Einstein gas, revisited, *Phys. Rep.* **32**, 169–248 (1977).
- [39] V. V. Kocharovskiy, V. V. Kocharovskiy, M. Holthaus, C. H. Raymond Ooi, A. Svidzinsky, W. Ketterle and M. O. Scully, Fluctuations in ideal and interacting Bose-Einstein condensates: from the laser phase transition analogy to squeezed states and Bogoliubov quasiparticles, *Adv. At. Mol. Opt. Phys.* **53**, 291–411 (2006).
- [40] C. Weiss and M. Wilkens, Particle number counting statistics in ideal Bose gases, *Opt. Express* **1**, 272–83 (1997).
- [41] C. J. Pethick and H. Smith, Bose-Einstein condensation in dilute gases, Second Edition (Cambridge, 2008).
- [42] W. Ketterle and N. J. Van Druten, Bose-Einstein condensation of a finite number of particles trapped in one or three dimensions, *Phys. Rev. A* **54**, 656 (1996).
- [43] F. Dalfovo, S. Giorgini, L. P. Pitaevskii and S. Stringari, Theory of Bose-Einstein condensation in trapped gases, *Rev. Mod. Phys.* **71**, 463–512 (1999).
- [44] N. N. Bogoliubov, On the theory of superfluidity, *J. Phys. (USSR)* **11**, 23–32 (1947).
- [45] A. Griffin, Conserving and gapless approximations for an inhomogeneous Bose gas at finite temperatures, *Phys. Rev. B* **53**, 9341–9347 (1996).

- [46] S. Giorgini, L. P. Pitaevskii and S. Stringari, Thermodynamics of a trapped Bose-condensed gas, *J. Low Temp. Phys.* **109**, 309–355 (1997).
- [47] S. Giorgini, L. P. Pitaevskii and S. Stringari, Condensate fraction and critical temperature of a trapped interacting Bose gas, *Phys. Rev. A* **54**, R4633–R4636 (1996).
- [48] M. J. Davis and P. B. Blakie, Critical temperature of a trapped Bose gas: comparison of theory and experiment, *Phys. Rev. Lett.* **96**, 060404 (2006).
- [49] R. P. Smith, N. Tammuz, R. L. D. Campbell, M. Holzmann and Z. Hadzibabic, Condensed fraction of an atomic Bose gas induced by critical correlations, *Phys. Rev. Lett.* **107**, 1–5 (2011).
- [50] R. P. Smith, R. L. D. Campbell, N. Tammuz and Z. Hadzibabic, Effects of interactions on the critical temperature of a trapped Bose gas, *Phys. Rev. Lett.* **106**, 1–4 (2011).
- [51] D. V. Schroeder, *An introduction to thermal physics* (Addison Wesley Longman, 2000).
- [52] M. Holthaus, E. Kalinowski and K. Kirsten, Condensate fluctuations in trapped Bose gases: canonical vs. microcanonical ensemble, *Ann. Phys.* **270**, 198–230 (1998).
- [53] J. Klaers, J. Schmitt, T. Damm, F. Vewinger and M. Weitz, Statistical physics of Bose-Einstein-condensed light in a dye microcavity, *Phys. Rev. Lett.* **108**, 160403 (2012).
- [54] J. Schmitt, T. Damm, D. Dung, F. Vewinger, J. Klaers and M. Weitz, Observation of grand-canonical number statistics in a photon Bose-Einstein condensate, *Phys. Rev. Lett.* **112**, 030401 (2014).
- [55] H. D. Politzer, Condensate fluctuations of a trapped, ideal Bose gas, *Phys. Rev. A* **54**, 5048–5054 (1996).

-
- [56] M. Gajda and K. Rzażewski, Fluctuations of Bose-Einstein condensate, *Phys. Rev. Lett.* **78**, 2686–2689 (1997).
- [57] P. Navez, D. Bitouk, M. Gajda, Z. Idziaszek and K. Rzażewski, Fourth statistical ensemble for the Bose-Einstein condensate, *Phys. Rev. Lett.* **79**, 1789–1792 (1997).
- [58] Z. Idziaszek, M. Gajda, P. Navez, M. Wilkens and K. Rzażewski, Fluctuations of the weakly interacting Bose-Einstein condensate, *Phys. Rev. Lett.* **82**, 4376–4379 (1999).
- [59] V. V. Kocharovskiy, V. V. Kocharovskiy and M. O. Scully, Condensate statistics in interacting and ideal dilute Bose gases, *Phys. Rev. Lett.* **84**, 2306–2309 (2000).
- [60] V. V. Kocharovskiy, V. V. Kocharovskiy and M. O. Scully, Condensation of n bosons. III. analytical results for all higher moments of condensate fluctuations in interacting and ideal dilute Bose gases via the canonical ensemble quasiparticle formulation, *Phys. Rev. A* **61**, 053606 (2000).
- [61] V. V. Kocharovskiy, M. O. Scully, S.-Y. Zhu and M. Suhail Zubairy, Condensation of n bosons. II. nonequilibrium analysis of an ideal Bose gas and the laser phase-transition analogy, *Phys. Rev. A* **61**, 023609 (2000).
- [62] A. A. Svidzinsky and M. O. Scully, Condensation of n interacting bosons: a hybrid approach to condensate fluctuations, *Phys. Rev. Lett.* **97**, 1–4 (2006).
- [63] A. A. Svidzinsky and M. O. Scully, Condensation of n bosons: microscopic approach to fluctuations in an interacting Bose gas, *Phys. Rev. A* **82**, 063630 (2010).
- [64] H. Xiong, S. Liu, G. Huang and Z. Xu, Canonical statistics of trapped ideal and interacting Bose gases, *Phys. Rev. A* **65**, 033609 (2002).

- [65] S. Liu, H. Xiong, G. Huang and Z. Xu, Anomalous particle-number fluctuations in a three-dimensional interacting Bose-Einstein condensate, *Phys. Rev. A* **68**, 065601 (2003).
- [66] F. Illuminati, P. Navez and M. Wilkens, Thermodynamic identities and particle number fluctuations in weakly interacting Bose-Einstein condensates, *J. Phys. B: At., Mol. Opt. Phys.* **32**, L461 (1999).
- [67] V. I. Yukalov, Principal problems in Bose-Einstein condensation of dilute gases, *Laser Phys. Lett.* **1**, 435–461 (2004).
- [68] V. I. Yukalov, No anomalous fluctuations exist in stable equilibrium systems, *Phys. Lett. A* **340**, 369–374 (2005).
- [69] A. Y. Cherny, Condensate fluctuations in the dilute Bose gas, *Phys. Rev. A* **71**, 043605 (2005).
- [70] Z. Idziaszek, Ł. Zawitkowski, M. Gajda and K. Rzażewski, Fluctuations of a weakly interacting Bose-Einstein condensate, *Europhys. Lett.* **86**, 10002 (2009).
- [71] S. Bhattacharyya and B. Chakrabarti, Condensate fluctuation and thermodynamics of mesoscopic Bose-Einstein condensates: a correlated many-body approach, *Phys. Rev. A* **93**, 023636 (2016).
- [72] M. Brewczyk, M. Gajda and K. Rzażewski, Classical fields approximation for bosons at nonzero temperatures, *J. Phys. B: At., Mol. Opt. Phys.* **40**, R1 (2007).
- [73] E. Witkowska, M. Gajda and K. Rzażewski, Bose statistics and classical fields, *Phys. Rev. A* **79**, 033631 (2009).
- [74] P. Bienias, K. Pawłowski, M. Gajda and K. Rzażewski, Statistical properties of one-dimensional Bose gas, *Phys. Rev. A* **83**, 033610 (2011).

- [75] M. A. Kristensen, M. B. Christensen, M. Iglicki, K. Pawłowski, C. Klempt, J. F. Sherson, K. Rzążewski, A. J. Hilliard and J. J. Arlt, Observation of fluctuations in a Bose-Einstein condensate, In preparation (2018).
- [76] Y. Castin and R. Dum, Bose-Einstein condensates in time dependent traps, *Phys. Rev. Lett.* **77**, 5315–5319 (1996).
- [77] A. Griffin, T. Nikuni and E. Zaremba, Bose-condensed gases at finite temperatures (Cambridge University Press, 2009).
- [78] M. Naraschewski and D. M. Stamper-Kurn, Analytical description of a trapped semi-ideal Bose gas at finite temperature, *Phys. Rev. A* **58**, 2423–2426 (1998).
- [79] W. Ketterle, D. S. Durfee and D. M. Stamper-Kurn, Making, probing and understanding Bose-Einstein condensates, in *Proceedings of the international school of physics of enrico fermi*, edited by M. Inguscio, S. Stringari and C. E. Wieman (Italian Physical Society, 1998), pp. 67–164.
- [80] J. Szczepkowski, R. Gartman, M. Witkowski, L. Tracewski, M. Zawada and W. Gawlik, Analysis and calibration of absorptive images of Bose-Einstein condensate at nonzero temperatures, *Rev. Sci. Instrum.* **80**, 053103 (2009).
- [81] H. K. Andersen, Bose-Einstein condensates in optical lattices, PhD thesis (Department of Physics and Astronomy, Aarhus University, 2008).
- [82] J. F. Bertelsen, Ultracold atomic gases, PhD thesis (Department of Physics and Astronomy, Aarhus University, 2007).
- [83] P. L. Pedersen, Mult-mode spin dynamics of a Bose-Einstein condensate in an optical lattice, PhD thesis (Department of Physics and Astronomy, Aarhus University, 2014).

- [84] M. Gajdacz, Non-destructive imaging and feedback with ultracold gases, PhD thesis (Department of Physics and Astronomy, Aarhus University, 2015).
- [85] H. J. Metcalf and P. van der Straaten, Laser cooling and trapping (Springer, 1999).
- [86] T. Esslinger, I. Bloch and T. W. Hänsch, Bose-Einstein condensation in a quadrupole-Ioffe-configuration trap, *Phys. Rev. A* **58**, R2664–R2667 (1998).
- [87] S. S. Snefturp, Bragg diffraction of Bose-Einstein condensates, MA thesis (Department of Physics and Astronomy, Aarhus University, 7th Sept. 2018).
- [88] G. Camy, C. J. Bordé and M. Ducloy, Heterodyne saturation spectroscopy through frequency modulation of the saturating beam, *Opt. Commun.* **41**, 325–330 (1982).
- [89] V. Negnevitsky and L. D. Turner, Wideband laser locking to an atomic reference with modulation transfer spectroscopy, *Opt. Express* **21**, 3103–3113 (2013).
- [90] G. Reinaudi, T. Lahaye, Z. Wang and D. Guery-Odelin, Strong saturation absorption imaging of dense clouds of ultracold atoms, *Opt. Lett.* **32**, 3143 (2007).
- [91] P. L. Pedersen, M. Gajdacz, F. Deuretzbacher, L. Santos, C. Klempt, J. F. Sherson, A. J. Hilliard and J. J. Arlt, Spin dynamics in a two-dimensional quantum gas, *Phys. Rev. A* **89**, 051603 (2014).
- [92] C. F. Ockeloen, A. F. Tauschinsky, R. J. C. Spreeuw and S. Whitlock, Detection of small atom numbers through image processing, *Phys. Rev. A* **82**, 061606 (2010).
- [93] J. Stenger, S. Inouye, A. P. Chikkatur, D. M. Stamper-Kurn, D. E. Pritchard and W. Ketterle, Bragg spectroscopy of a Bose-Einstein condensate, *Phys. Rev. Lett.* **82**, 4569–4573 (1999).

-
- [94] J. E. Simsarian, J. Denschlag, M. Edwards, C. W. Clark, L. Deng, E. W. Hagley, K. Helmerson, S. L. Rolston and W. D. Phillips, Imaging the phase of an evolving Bose-Einstein condensate wave function, *Phys. Rev. Lett.* **85**, 2040–2043 (2000).
- [95] S.-w. Chiow, T. Kovachy, H.-C. Chien and M. A. Kasevich, $102\hbar k$ large area atom interferometers, *Phys. Rev. Lett.* **107**, 130403 (2011).
- [96] R. Lopes, C. Eigen, N. Navon, D. Clément, R. P. Smith and Z. Hadzibabic, Quantum depletion of a homogeneous Bose-Einstein condensate, *Phys. Rev. Lett.* **119**, 190404 (2017).
- [97] C. J. Foot, *Atomic physics*, Oxford Master Series in Physics (Oxford University Press, 26th Aug. 2011).
- [98] K. Bongs, S. Burger, S. Dettmer, D. Hellweg, J. Arlt, W. Ertmer and K. Sengstock, Waveguide for Bose-Einstein condensates, *Phys. Rev. A* **63**, 031602 (2001).
- [99] M. A. Kristensen, High-precision non-destructive imaging and active stabilisation of ultracold clouds, Progress Report (Department of Physics and Astronomy, Aarhus University, 29th July 2016).
- [100] C. Menotti, M. Krämer, A. Smerzi, L. Pitaevskii and S. Stringari, Propagation of sound in a Bose-Einstein condensate in an optical lattice, *Phys. Rev. A - At. Mol. Opt. Phys.* **70**, 553–556 (2004).
- [101] W. Ketterle and N. J. Van Druten, Evaporative cooling of trapped atoms, in *Advances in atomic, molecular, and optical physics*, Vol. 37, edited by B. Bederson and H. Walther, *Advances In Atomic, Molecular, and Optical Physics* (Academic Press, 1996), pp. 181–236.
- [102] M. S. Robbins and B. J. Hadwen, The noise performance of electron multiplying charge-coupled devices, *IEEE Trans. Electron Devices* **50**, 1227–1232 (2003).

BIBLIOGRAPHY

- [103] J. Hyneczek, S. Member and T. Nishiwaki, Excess noise and other important characteristics of low light level imaging using charge multiplying ccids, *IEEE Trans. Electron Devices* **50**, 239–245 (2003).
- [104] D. B. Hume, I. Stroescu, M. Joos, W. Muessel, H. Strobel and M. K. Oberthaler, Accurate atom counting in mesoscopic ensembles, *Phys. Rev. Lett.* **111**, 253001 (2013).
- [105] C.-S. Chuu, F. Schreck, T. P. Meyrath, J. L. Hanssen, G. N. Price and M. G. Raizen, Direct observation of sub-Poissonian number statistics in a degenerate Bose gas, *Phys. Rev. Lett.* **95**, 260403 (2005).
- [106] M. B. Christensen, Precision investigation of Bose-Einstein condensates and the observation of ground state occupation fluctuations, Progress Report (Department of Physics and Astronomy, Aarhus University, 1st June 2018).
- [107] S. Dettmer, D. Hellweg, P. Ryytty, J. J. Arlt, W. Ertmer, K. Sengstock, D. S. Petrov, G. V. Shlyapnikov, H. Kreutzmann, L. Santos and M. Lewenstein, Observation of phase fluctuations in elongated Bose-Einstein condensates, *Phys. Rev. Lett.* **87**, 160406 (2001).
- [108] E. Cho, M. J. Cho and J. Eltinge, The variance of sample variance from a finite population, *IJPAM* **21**, 387–394 (2005).
- [109] E. Cho and M. J. Cho, Variance of sample variance with replacement, *IJPAM* **52**, 43–47 (2009).